SUPERSONIC FLUTTER OF CIRCULAR CYLINDRICAL SHELLS

Thesis by
Mervyn Daniel Olson

In Partial Fulfillment of the Requirements
For the Degree of
Doctor of Philosophy

California Institute of Technology
Pasadena, California
1966
(Submitted May 20, 1966)

ACKNOWLEDGMENT

The author is sincerely grateful to Prof. Y. C. Fung for the opportunity to undertake this research project and for the patient guidance and encouragement provided by him during the course of the investigation. The technical assistance provided by Drs. E. E. Sechler, T. Kubota, C. D. Babcock, Jr., L. V. Schmidt and Mr. M. E. Jessey is also gratefully acknowledged. Much of the success of the experimental investigations must be accredited to the tireless efforts of Messrs. R. D. Luntz, C. B. Hemphill, M. E. Jessey and Dr. L. V. Schmidt during the trying early morning hours of the wind tunnel testing. Thanks are also due Miss Martha Fossum and Mrs. Philip Cassady for their skilled typing of the manuscript.

This research was supported by the United States Air Force, through the Office of Scientific Research. The help provided by Dr. J. Pomerantz of OSR, C. W. Tusch of the USAF, and V. D. Reed, J. L. Jones, R. E. Fahey, S. Treon and J. Tietz of the NASA Ames Research Center is gratefully acknowledged.

Finally, the author is sincerely grateful for the financial support received from the California Institute of Technology, the Johnson's Wax Fund and the National Research Council of Canada.

ABSTRACT

Various experimental and theoretical studies on the supersonic flutter of circular cylindrical shells are discussed.

Results of experiments in the Mach number range 2.5 - 3.5 are presented. Three shells with radius-to-thickness ratios of 2,000 were subjected to radial external pressure loadings and to combinations of axial compressive loading and internal pressurization while in the presence of an external axially-directed supersonic flow.

Small amounts of internal pressurization were very stabilizing with respect to flutter, but moderate amounts reduced stability to the unpressurized level. However, high internal pressures completely stabilized the shells. The axial compressive loading was slightly destabilizing for moderate amounts of internal pressurization.

The flutter modes (which were standing waves in the axial direction with zero, one or two circumferential nodal lines) contained many waves around the circumference (of the order of 20) that travelled in the circumferential direction. This circumferentially travelling wave phenomenon possibly results from the nonlinear nature of cylindrical shells.

Model integrity was not threatened by even the most violent flutter which occurred just prior to buckling under radial external pressure loading and just after buckling under axial compressive loading. Buckled portions of a shell did not flutter. It appears that the large local curvatures encountered in the buckling of a cylindrical shell tend to stabilize the shell locally. However, it also appears that the localized buckling usually encountered in practice reduces the stability of any unbuckled regions of the shell.

The experimental flutter boundaries are compared with various theoretical predictions. Following Voss, a modal analysis which satisfies the so-called freely supported shell boundary conditions is used in conjunction with different aerodynamic approximations - namely piston theory and the potential theory of Leonard and Hedgepeth. It was found that the pressurized cylindrical shells fluttered at a lower level of free stream energy than predicted by the theory. Of the two results, that using piston theory appears to correspond closest to the experiment both in stability boundary and in critical values of circumferential wave number. Both predictions yield a larger stabilizing influence of the shell internal pressure than observed in the experiment.

An analysis is presented for calculating the final limiting amplitudes of flutter based on a two-mode, piston theory approximation. A Galerkin procedure is used to reduce the nonlinear shallow shell equations of Marguerre to two coupled nonlinear ordinary differential equations for the modal amplitudes. An approximate limit cycle solution to these equations is obtained by the method of Krylov and Bogoliubov. The results indicate that for practical purposes

cylindrical shell flutter does not occur below the stability boundary for infinitesimal disturbances. The limit cycle amplitudes predicted by this analysis seem to agree very well with the experimental ones. The results further indicate that the flutter amplitude, frequency and mode shape should change discontinuously (or jump) as the aerodynamic pressure is increased beyond the value for first flutter.

TABLE OF CONTENTS

LIST OF ILLUSTRATIONS

Figures in Appendices

LIST OF SYMBOLS *

a, b, c	shell parameters in nonlinear flutter solution; Eq. 3.24
a_1, a_2	modal amplitudes in nonlinear flutter solution; Eq. 3.23
a_∞	free stream speed of sound (ips)
A(t), B(t)	slowly varying amplitudes; Eq. 3.26
$\overline{A}$, $\overline{B}$	averages of A, B over one period
$A(\bar{x})$	Eq. 3.34
c_m	complex modal amplitudes in linear flutter solution
C_p	pressure coefficient = $(p_{wall} - p_\infty)/q_\infty$
D	shell bending rigidity = $Eh^3/(12(1 - \nu^2))$
E	Young's modulus (psi)
f	aerodynamic pressure parameter = $8\gamma M_\infty p_\infty / 3\rho_s L h$ (sec^{-2}) Eq. 3.24
f_o	value of f for flutter according to linearized two mode solution; Eq. 3.33
F	stress function; Eqs. 3.10 and 3.22

* Note that the symbols used in Appendices F, G and H are defined there.

G_j	(j = 1 to 3); Eq. 3.35
h	skin thickness of shell (inch)
i	$\sqrt{-1}$
j	number of circumferential nodal lines between the ends of the shell in flutter mode
k	nondimensional frequency = $\omega / \alpha_m U_\infty$
k_m	Eq. 3.7
K_j	(j = 1 to 4); Eq. 3.30
L	unsupported length of cylindrical shell (inches)
m	number of half waves between ends of shell in vibration mode
M, M_∞	Mach numbers locally and in free stream, respectively
M_1	$M_\infty(1 - k)$; Appendix F
M_2	$M_\infty(1 + k)$; Appendix F
n	number of circumferential waves in flutter or vibration mode
n_{min}	value of n corresponding to minimum flutter condition
N	number of modes in linear flutter solution; Eq. 3.12
$N_x, N_\theta, N_{x\theta}$	stress resultants in shell due to shell motion and to
$\overline{N}_x, \overline{N}_\theta, \overline{N}_{x\theta}$	applied loadings, respectively (lb/inch)

p	aerodynamic pressure term in Eqs. 3.10 and 3.11
p_∞	free stream static pressure (psf or psi)
$p_{\infty\ min}$	value of p_∞ corresponding to n_{min}
p_{cm}, p_{sm}	coefficients in aerodynamic pressure expression, Eq. 3.14
p_m	pressure differential across shell skin, positive for tensile hoop stress (psig)
$p_{m_{cr}}$	value of p_m which causes shell to buckle under radial external pressure loading
p_r	pressure in rubber tubes of axial loading mechanism (psig)
p_{t_∞}	free stream stagnation pressure (psfa)
p_{wall}	local static pressure on shell (psfa)
P_x	axial compressive load on cylindrical shell (lb)
q_∞	free stream dynamic pressure (psf)
R	radius of cylindrical shell (inches)
R_e	Reynolds number based on distance from leading edge of cylindrical flutter model
t	time (seconds)
T_{t_∞}	free stream stagnation temperature (degrees F)
u, v, w	shell displacements; Fig. 29
U_∞	free stream velocity (fps)

w_i	radial deflection shell skin as measured by i-th pickup (inches) i = 1, 2 or 3
$\overline{w^2}$	mean square value of shell skin deflection in oscillatory motion (inches^2)
w_{rms}	root mean square value of shell skin deflection in oscillatory motion (inches)
x, y, z	shell coordinates; Fig. 29
x_i	(i = 1 to 4); Eq. 3.31
x_{i_o}, x_{i_1}	(i = 1 to 4); Section 3.4.1
$\vec{x}$, $\vec{x}_o$	Eq. 3.34
α	π/L ; Eq. 3.23
α_m, α_ℓ	axial wave numbers = $m\pi/L$, $\ell\pi/L$, respectively; Eq. 3.12
β, β_m	imaginary part of frequency root; Section 3.3.1 b
γ	gas constant = 1.4
γ_1	structural damping coefficient (corresponds to γ in Ref. 22)
$\delta_{m\ell}$	Kronecker delta
δx_i	increment in x_i (i = 1 to 4); Section 3.4.1
Δ	aerodynamic damping parameter = $\gamma p_\infty / \rho_s h a_\infty (sec^{-1})$; Eq. 3.24

$\Delta_{m\ell}$ $= \begin{cases} 4\ell/\pi(\ell^2 - m^2) & \text{for } m + \ell \text{ odd; Eq. 3.15} \\ 0 & \text{otherwise} \end{cases}$

ε small nonlinearity parameter $= (n^2 h/R)^2$

θ angular position around model; looking upstream, positive θ is counter-clockwise and $\theta = 30^\circ$ corresponds to top of model. (Note, in Appendix E, $\theta = 0$ corresponds to right hand horizontal when looking upstream). Also see Fig. 29 for analytic work.

θ_1, θ_2 $\omega t + \varphi_1$, $\omega t + \varphi_2$, respectively; Eq. 3.27

κ $3L/8\, M_\infty a_\infty$

λ eigenvalue; Eq. 3.38

μ_m Eq. 3.6

ν Poisson's ratio

ξ, η normalized modal amplitudes a_1/h, a_2/h, respectively; Eq. 3.24

$\vec{\xi}$ limit cycle perturbation vector; Eq. 3.36

ρ_∞ free stream density (lb sec^2/ in^4)

ρ_s shell material density (lb sec^2/ in^4)

σ $\propto R/n$

ϕ phase angle of flutter mode; Figs. 31 and 34

ϕ_m argument of modal amplitudes c_m; Tables V, VI, VII

$\varphi_1(t)$, $\varphi_2(t)$	slowly varying phases; Eq. 3.26
$\bar{\varphi}_1$, $\bar{\varphi}_2$	averages of φ_1, φ_2 over one period
$\Psi_m(x)$	vibration mode for clamped-clamped beam; Eq. 3.5
ω	flutter or vibration frequency (rad/sec)
ω_o	flutter frequency according to linearized two mode solution; Eq. 3.33
ω_m	real part of frequency root; Section 3.3.1 b
ω_{mn}	linearized modal frequency; Eq. 3.16
Ω, Ω_m	complex frequency roots; Section 3.3.1 b

Miscellaneous Notation

$$\nabla^2 = \frac{\partial^2}{\partial x^2} + \frac{1}{R^2}\frac{\partial^2}{\partial \theta^2}$$

$$\nabla^4 = \nabla^2 \nabla^2 \quad , \quad \nabla^8 = \nabla^4 \nabla^4$$

$\left[\frac{q_\infty}{E(M_\infty - 1)^{\frac{1}{2}}}\right]^{\frac{1}{3}} \frac{R}{h}$ nondimensional parameter which defines approximate flutter boundary for cylindrical shells. See for example, Refs. 1 and 2 .

I. INTRODUCTION

The self-excited oscillation of thin plates or membranes exposed on one side to a parallel supersonic airstream is called panel flutter. The outer skin on almost all high speed flight vehicles is supported by variously spaced spars or ribs which divide it into individual panels forming an array, and these panels are susceptible to this flutter instability especially when subjected to in-plane compressive loads. In some cases, the prevention of this instability becomes the primary design criterion.

A thin-walled cylindrical shell of finite length may be considered as a degenerate panel which is closed on itself in the transverse direction. Such a panel or shell may also exhibit this flutter instability. In fact, the first reported occurrence of the phenomenon appears to have been on the V-2 rocket.

The first successful experimental observation of cylindrical shell flutter was obtained by the GALCIT* at the NASA Ames 8 x 7 foot supersonic tunnel in May 1962 (Refs. 1 and 2). Further experiments carried out by the writer in June and August 1964 were designed to clarify the interaction of flutter and buckling.

---

* Graduate Aeronautical Laboratories, California Institute of Technology.

The nonlinear interaction between buckling and flutter of flat panels or curved shell segments is a complex but important problem, mainly because the severest flutter seems to occur in the vicinity of buckling. In the case of flat panels, both theoretical and experimental results indicate that the flat panel is much more susceptible to large amplitude flutter in the buckled configuration. Theory for this interaction for the complete cylindrical shell is not yet available, but the limited results from the GALCIT - Ames experiments indicate that the maximum amplitude of flutter is obtained as buckling is approached, and that the flutter disappears when the shell is completely buckled. The shell with large buckles seems to act like a corrugated shell, whose critical flutter speed is much higher than that of the circular shell. These results were limited to buckling under radial external pressure loading only.

The buckling of a cylindrical shell under axial compression results in a buckling mode entirely different from that of radial external pressure loading. For low values of internal pressure, the well-known diamond pattern buckles are obtained, and at high values, the so-called bellows shaped ones are obtained. See for example, the excellent photographs in Ref. 3. Consequently, it was to be expected that the effect of axial compressive loading on the flutter would be entirely different from that of the radial external pressure loading. Hence, further experiments to investigate this interaction seemed desirable.

These experiments were carried out during the summer of 1964 at the NASA Ames 8 x 7 foot supersonic tunnel in two different phases. The first phase consisted of measuring the static pressure distribution over the thin shell section of the cylindrical

panel flutter model in the absence of flutter. The second phase consisted of the actual flutter tests. The first part of this thesis describes these experiments and the results obtained from them.

In the second part of this thesis, an attempt is made to provide some quantitative comparison between the experimental results and theory. Although by no means complete, this comparison goes far in straightening out some of the controversy over this problem already present in the literature.

Previously, it was thought that all published theories for cylindrical shell flutter yielded pessimistic results as to thicknesses required to prevent the instability. The influence of the viscous boundary layer, which was ignored in all these theories, was suggested as a possible explanation for the apparent discrepancy between theory and practice. Calculations based on a simple step boundary layer model (a thin region of uniform subsonic flow between the shell and the outer uniform supersonic flow) by Anderson and Fung (Ref. 4) revealed the possibility of significant changes in the stability boundaries for shell flutter with many circumferential waves.

This problem is re-examined herein by using a somewhat more realistic boundary layer model - that of a parallel shear flow with a velocity profile given by the mean velocity distribution in a classical turbulent boundary layer. The oscillating shell surface is approximated by an oscillating plane wall whose deflection is sinusoidal in both in-plane directions. Viscous effects are neglected with respect to flow perturbation quantities, and the resulting equations are linearized. The final equations admit solutions with exponential dependence on time and the in-plane coordinate directions but must be integrated

numerically in the direction normal to the plane. Several examples are worked out and are presented in Appendix G. The results from this study are the results of more recent work by Anderson (Ref. 5) indicate that the influence of the boundary layer may have been over predicted by an order of magnitude in the earlier work.

The experiments revealed that the shell internal pressure was an important parameter for the flutter phenomenon. Consequently, calculations including the effect of internal pressure were required for comparison purposes. Detailed calculations including this effect are presented using an analysis similar to that of Voss (Ref. 6), but using two main aerodynamic theories - piston theory and the potential theory of Leonard and Hedgepeth (Ref. 7). Although the use of the latter theory implies a neglect of the leading edge effect, it seems to be the easiest way to include three dimensional effects while retaining the simplicity of a sine wave modal analysis.

Finally, a nonlinear flutter analysis based on a two-mode, piston theory approximation is presented. A Galerkin procedure is used to reduce the nonlinear shallow shell equations of Marguerre to two coupled nonlinear ordinary differential equations for the modal amplitudes. An approximate limit cycle solution to these equations is obtained by the method of Krylov and Bogoliubov, and its stability is studied by the method of averaging.

II. EXPERIMENTS

2.1 Introduction

The same basic model used in the 1962 experiments (Ref. 1) was used in the new tests. The cylindrical shells, having a diameter of 16 inches and wall thicknesses of 0.0040 inches (hence a radius-to-thickness ratio of 2000), were again fabricated by electroplating. Over the years the electroplating technique has improved so that shells of smoother surface, more uniform thickness distribution, and higher yield point were obtained. A modification of the shell support and fabrication procedure was introduced so that the shells could be loaded in axial compression. With the new design, a test shell could be mounted on the model in the tunnel in about thirty minutes time.

The model consists of a nose, a center section which supports the thin shell flutter model and instrumentation, and a tail section which connects the center section to the wind tunnel sting. An ideal nose for this model would provide a rapid pressure recovery and uniform flow over the thin shell section. According to aerodynamic theory, this ideal nose would have a different shape for each Mach number to be tested. Since this was impractical, one shape was chosen for the middle Mach number with the hope that Mach number effects would be small. Cowl number six of Ref. 8 was chosen for this purpose, and the data given in this reference would seem to support this hope.

Previously, a check on the suitability of this cowl for the flutter model was made (in 1962) on a reduced scale model of 2.0 inches diameter in a 9 x 9 inch supersonic wind tunnel. It was ascertained (Ref. 1) that the variation of static pressure over the length of the model was less than 2 per cent of the dynamic pressure in the range of Mach numbers of interest, and this was regarded as satisfactory for the previous flutter tests whose purpose was mainly the determination of flutter characteristics of pressurized shells. It is well known that the exact variation of static pressure over a model depends to a large extent on the tunnel, and on the Reynolds number (model size). Hence, for more accurate information, the full scale model should be tested in the 8 x 7 foot tunnel. Now, for the thin shells of thickness 0.0040 inches to be used in the flutter tests, the radial external pressure loading which causes buckling is of the order of 0.05 psig. This pressure is so small that only very small variations in static pressure over the shell could be tolerated. These considerations resulted in the decision to investigate the static pressure distribution over the thin shell section of the model.

A description of this investigation and of the results obtained from it is given in Appendix E. It was found that the best testing conditions for the flutter experiments would be in the vicinity of $M_{\infty} = 3.0$.

2.2 Flutter Tests

2.2.1 Model and instrumentation

The cylindrical panel flutter model used in these experiments is the one described in Ref. 1 with some minor modifications. Its essential features are illustrated in Figs. 1 to 6.

The thin shells were constructed by electroplating copper onto a wax form. After being cut to length and removed from the form by melting the wax, each shell was soldered to two copper end rings as shown in Fig. 5. The mounting of a shell on the model for testing was accomplished by slipping the shell over the "0" ring seals from the upstream end of the model (left hand side of Fig. 4) after removing the thrust plate.

The pressure difference across the shell p_m (internal minus external pressure) was varied by varying the pressure in the sealed annular cavity under the shell. The shell was loaded axially in compression by pressurizing the rubber tubes adjacent to each of the copper end rings, as shown in Fig. 4.

Radial motion of the shell was measured by three inductance type pickups numbered 1 to 3 in Fig. 6. Pickups 1 and 2 are mounted on a drum which can be rotated 360 degrees, and pickup 1 can be moved longitudinally about two thirds the length of the shell. Pickup number 3 is fixed near the downstream end of the shell. A full 360 degree circumferential traverse and a full longitudinal traverse in one direction each takes about fifteen seconds. A potentiometer connected by gears to each traversing mechanism supplies D. C. voltage proportional to the distance or angle traversed. The signals

from the pickups and potentiometers were recorded on magnetic tape for later analysis.

A more complete description of the model and instrumentation is given in Appendix A.

2.2.2 Experimental procedure

The flow in the wind tunnel was started at a stagnation pressure p_{t_∞} of 2 psia and a shell internal pressure p_m of 4 psig. The low value of p_{t_∞} was chosen to ensure that the manometer fluid did not blow over when the flow became supersonic, and the high value of p_m was chosen to ensure that the shell did not buckle. After supersonic flow was established, p_m was held constant while p_{t_∞} was brought up to the value required for data.

Shell No. 1 (Table I) was tested at $M_\infty = 3.381$. The full range of available p_{t_∞} was covered with various values of positive p_m.

Shell No. 2 (Table II) was tested at $M_\infty = 2.993$. At first, p_m was held fixed while p_{t_∞} was varied over the available range. Then p_m was set at 3.93 psig, p_{t_∞} at 3170 psf and the axial compressive load P_x was increased until the shell buckled. The axial load was then removed and post-buckling flutter data was obtained for various combinations of p_{t_∞} and p_m.

Shell No. 3 (Table III) was also tested at $M_\infty = 2.993$. A determined effort to systematically cover the near-buckling region was made with this shell. Fig. 10 shows the estimated buckling boundaries which were used as a guide for this test. In order to avoid premature buckling of the shell, the test conditions were kept below and to the right of the dashed curve. Each of the test paths shown was followed for a particular setting of p_{t_∞}. As the last part of this test, the shell was buckled several times as indicated in Table III.

The actual recording of data on magnetic tape is described in Appendix B.

2.3 Results and Discussions

All the flutter data are tabulated in Tables I, II and III. Each table represents a different shell. The frequencies shown were obtained from power spectrum analyses of the shell motions and represent the predominant frequency present. The circumferential wave number n and the circumferential nodal line number j for each flutter mode were obtained from traverse plots like those of Figs. 20 to 25. The Correlation and Run numbers were used to correlate the data recorded by different methods.

2.3.1 Boundary layer

The boundary layer profiles near the downstream end of the shell are shown in Fig. 11 for $M_\infty = 2.993$. The data points near the shell surface (z = 0) should be viewed with some caution, since the finite size of the probes which has been ignored here would probably affect the profile shapes. However, the data does give an adequate indication of the overall boundary layer thickness. The figure indicates that the external flow was composed of a thin inner region (about 0.4 inches thick) which looks like a classical turbulent boundary layer and a rather extensive outer region containing a small Mach number gradient. This is typical of high Mach number flows over a test model. The "quasi-isentropic" nature of the outer region is a result of the so-called leading edge interaction.

No attempt was made to alter the boundary layer flow during these experiments, and hence its gross effect cannot be estimated. On the other hand, since most of the flutter data was

obtained at a constant Mach number and over a very limited range of dynamic pressures, the boundary layer flow was essentially constant. Hence, the effect of boundary layer changes during the experiments should be negligible.

2.3.2 Shell motion

Almost all the shell motion detected during the flutter test can be classified into four distinct types. A sample time trace of each of these types is exhibited in Fig. 12 and the power spectral density associated with each sample is shown in Fig. 13. Type (a) is random in frequency and of relatively low amplitude and represents the response of the shell to the turbulence in the airstream. Type (b) is a relatively clean sinusoidal oscillation with almost all of the shell motion concentrated at one frequency. This corresponds to the shell fluttering in one clean mode. Type (c) is a kind of beating between two or more sinusoidal oscillations of slightly different frequencies and corresponds to the shell fluttering in a combination of two or more distinct modes. Types (b) and (c) were obtained only when the shell internal pressure was positive and relatively large. Type (d) is a highly distorted sinusoidal oscillation of large amplitude with most of its power concentrated at one low frequency and was obtained when the internal pressure approached zero and went negative. Only the types (b) to (d) qualify for the term flutter.

The differences between the flutter phenomenon obtained in an experiment and the "instability" predicted by linear theory (that is, an exponential increase of amplitude with increasing time) are quite striking. These differences for the case of cylindrical

shell flutter are clearly explained in Section 6(a) of Ref. 1 and need only be summarized here. The main difference is that only the nonlinear limit cycle oscillations are seen in the experiment, and their association with the linear "instability" of the theory is merely intuitive.

2.3.3 General effects of the test parameters

Fig. 14 shows the variation of flutter amplitude with stagnation pressure p_{t_∞} as the internal pressure p_m was held fixed. Although the flutter amplitude increases with stagnation pressure, it does not increase monotonically.

According to Anderson and Fung (Ref. 4), small values of internal pressure are very stabilizing, but larger values tend to reduce stability to the unpressurized level. The results shown in Figs. 16 to 19 agree qualitatively with this prediction. For example, in Fig. 18, flutter was present when p_m was near zero but disappeared as p_m increased. It appeared again as p_m reached about 0.50 psig. Contrary to the theory however, large values of p_m completely stabilized the shell.

These figures also show that the axial load P_x was destabilizing when p_m was positive, in that it increased the range of p_m over which the shell fluttered. This agrees qualitatively with Kobayashi's theoretical prediction (Ref. 9). On the other hand, as can be seen from Figs. 17, 18 and 19, it had a slightly stabilizing effect on the flutter when p_m was near zero or negative.

The actual amplitude of flutter is a very complicated function of all the test parameters p_{t_∞}, p_m and P_x. The tabulated data indicates that the flutter mode (that is, the numbers j and n) is also a very complicated function of the test parameters. The non-linear character of the cylindrical shell, which to a large extent determines the final amplitude of the limit cycle oscillations, is a function of the numbers j and n and hence indirectly a function of the test parameters. Consequently, any attempt to explain the variations in flutter amplitude would have to include all these effects.

When Shell No. 1 (0.0040 inch thick) was tested at a free stream Mach number of 3.381 and maximum stagnation pressure of 3178 psf, no flutter was detected. For these conditions, the parameter $(q_\infty / E(M_\infty^2 - 1)^{1/2})^{1/3}$ R/h was 8.4 and was well above the value of 7.0 for which flutter was obtained when M_∞ was 2.993. The data from the pressure test (Appendix E) showed that the overall boundary layer * was very much thicker at the higher Mach number. This thicker boundary layer seems to have stabilized the shell.

2.3.4 Flutter modes

Typical examples of the measured mode shapes are shown in Figs. 20 to 25, and typical longitudinal distributions of the phase angle of the shell motions are shown in Fig. 26. The variations of the mean square amplitude of flutter in the axial direction showed that the flutter modes had zero, one, or two circumferential nodal lines between the ends of the shell; that is j = 0, 1 or 2 respectively. It is interesting to note that these nodal lines were not evenly spaced between the ends of the shell.

---

* I.e., classical boundary layer plus "quasi-isentropic" outer region. Cf. Section 2.3.1.

The j = 0 case occurred when the shell internal pressure p_m was near zero or negative for the unbuckled shell, but it also occurred when p_m was positive for the buckled shell (bellows shaped buckle). Figs. 22, 23 and 25 are typical examples. For this case, the motion of the shell at x/L = 0.15 led that at x/L = 0.72 by about 15 degrees, as shown in Fig. 26.

The j = 1 and 2 cases occurred for positive p_m and various axial loads P_x. Figs 21 and 24 are typical examples. For the j = 1 cases, the phase angle of the shell motion changed very little between the circumferential nodal line and the upstream end of the shell. The motion of the shell upstream of the nodal line led that of the downstream part by about 160 to 170 degrees, as shown in Fig. 26. The j = 2 modes were not clean enough to give a good measurement of the phase angle, and the example shown in Fig. 26 (Corr. No. 126) is not very accurate.

From these phase angle measurements and amplitude plots, it may be concluded that the flutter modes were approximately standing waves in the axial direction.

The example depicted in Fig. 20 shows that the flutter mode was a standing wave made up of many waves around the circumference (n = 20). This example of a standing wave around the circumference was the only one obtained. All the other traverse plots were of the circumferentially travelling wave type. For example, Fig. 24 shows that the mean square amplitude of motion was almost constant around the circumference, but the mean square of the difference of the signals from a circumferentially traversing pickup and the fixed pickup varied between approximately zero and a maximum many times around the circumference. In Appendix C, it is shown that a shell deflection of the form

$$w(x, \theta, t) = f(x) \left[A \sin n\theta \sin \omega t + B \cos n\theta \cos \omega t \right] \qquad (2.1)$$

where A is approximately equal to B will fit this plot, but one of the standing wave form

$$w(x, \theta, t) = f(x) \sin n\theta \sin \omega t \qquad (2.2)$$

will not. The former deflection shape may be put in the form (for A = B)

$$w(x, \theta, t) = A f(x) \cos (n\theta - \omega t) \qquad (2.3)$$

which is a "pseudo" travelling wave moving around the shell at an angular rate of $180\omega/n\pi$ degrees per second. This deflection is "pseudo" in the sense that there is nothing in the external flow to initiate such a circumferentially travelling wave.

One might suggest that the origin of this "pseudo" travelling wave lies in the nonlinear nature of the cylindrical shell. Evensen (Ref. 10) found this kind of phenomenon in his nonlinear forced vibrations of a thin ring and since the nonlinear character of cylindrical shell motions in mode shapes with large axial wave lengths (that is, for j small) is very much like that of a thin ring, it is not too surprising to find it here. See for example, Ref. 11.

When the cos $n\theta$ mode of a thin ring is driven into resonance and its amplitude of motion slowly increased by increasing the magnitude of the forcing function, at some critical amplitude the sin $n\theta$ mode will suddenly appear combining with the cos $n\theta$ mode in such a way as to form a "pseudo" travelling wave. This critical amplitude decreases with increasing wave number n and with decreasing damping in the ring. Qualitatively similar results would be expected to appear in cylindrical shell motions with large n and small j.

The physical explanation for the phenomenon is as follows. When the shell oscillates with a frequency ω in a cos $n\theta$ standing wave mode at large amplitude (for the shell this means motions of at least the order of the skin thickness), the mean position of the shell oscillates with a frequency 2ω at small amplitude. This means that the shell's mean position is oscillating at twice the natural frequency of the sin $n\theta$ mode (assuming the shell is perfect, the sin $n\theta$ and cos $n\theta$ modes have the same natural frequency since they represent the same deflection shape even though they are independent orthogonal modes) and hence parametrically excites the sin $n\theta$ mode. As in most parametrically excited vibrations in real systems, there is a minimum amplitude of the excitation required to produce the phenomenon.

If imperfections exist in the ring or the shell, the natural frequencies of the sin $n\theta$ and cos $n\theta$ modes will be separated. In this case, the second mode will only appear at small amplitude and consequently may not be observable, or if the separation is large enough, it may not occur at all. This possibly is the explanation for why this phenomenon was not detected in the tests of Ref. 1.

Most of the data from those tests were obtained from an especially thin shell (0.0032 inches as compared to 0.0040 inches for the tests described herein), and it is more difficult to minimize imperfections in the thinner shell. Many improvements in shell making were developed in the time between the two tests so that the shells tested most recently were undoubtedly of better quality.

2.3.5 Flutter in the vicinity of buckling

When Shell No. 2 (0.0039 inch thick) was taken towards axial buckling by increasing the axial compressive load P_x while maintaining a high internal pressure p_m and a high stagnation pressure p_{t_∞}, no flutter was detected. The shell buckled in a single bellows shaped mode at the downstream end as shown in Fig. 7. The buckle was about 1/16 inch high by 1/4 inch wide and was adjacent to the rear end ring, being almost perfectly symmetric about the shell. The rest of the shell remained unbuckled. After the axial load was removed, the buckle did not pop out indicating that the shell material had yielded. With $P_x = 0$ and $p_m = 3.93$ psig, the shell was still stable, but when p_m was lowered to around 1 psig, it fluttered with a much larger amplitude and in a different mode than it had before it was buckled. See for example, Fig. 23. Fig. 15 shows the variation in flutter amplitude with p_m and p_{t_∞} for this shell in the vicinity of $p_m = 0$, and Fig. 22 shows the flutter mode. The flutter amplitude was very much higher on one side of the shell than on the other, having a maximum rms amplitude of about four shell thicknesses near $x/L = 0.5$ and $\theta = -20^\circ$. Note that the data of Fig. 15 is only for a particular point on the shell and does not show the maximum flutter amplitude. This same type of response was obtained for the

unbuckled shell and will be elaborated on in the next paragraphs. As the last step, this shell was buckled at a p_m = -0.017 psig and P_x = 0. At this pressure setting, the buckling mode was of the form of four 5 inch waves around the top of the shell with no node between the ends. The buckled region was very stable, but the unbuckled region fluttered quite violently.

When Shell No. 3 (0.0040 inch thick) was taken toward buckling by decreasing p_m, different things happened for different settings of p_{t_∞} and P_x. See Figs. 16 to 19.

(i) At p_{t_∞} = 1768 psf, no flutter was detected.

(ii) At p_{t_∞} = 2120 psf, large amplitude flutter was obtained as p_m went to zero and the amplitude increased to a maximum near a p_m of one half the critical value for buckling under radial external pressure loading only. The flutter mode was of the localized type as shown in Fig. 25, with a maximum rms amplitude of about three shell thicknesses near the middle of one side of the shell. A small amount of axial load decreased the amplitude but did not change the trend.

(iii) At p_{t_∞} = 2475 psf, localized flutter was again detected near p_m = 0 for P_x = 0, but disappeared as p_m went negative. When a small amount of axial load was applied, the flutter near p_m = 0 did not occur.

(iv) At p_{t_∞} = 2827 psf, localized flutter was again detected near p_m = 0. As p_m went negative, the flutter amplitude first increased and then decreased as p_m went past half the critical value. A small amount of axial load effectively removed this flutter.

When p_{t_∞} was returned to 2475 psf, P_x set at 90 pounds and p_m decreased in steps until the shell buckled at $p_m = -0.037$ psig, no flutter was detected. Only very shallow longitudinal buckles occurred around the top of the shell and were quickly removed by immediately raising p_m. When the above process was repeated with $P_x = 200$ pounds, the shell buckled at $p_m = 0.010$ psig, but again no flutter was detected. Again only shallow buckles of the diamond pattern type occurred near the downstream end of the shell and did not pop out as p_m was increased to 0.015 psig. At this setting, violent flutter was observed on the forward portion of the shell which had not buckled, but the buckled region of the shell was very quiet. When p_m was then increased to 0.49 psig, the buckles popped out and the shell was quiet again. P_x was then set at 240 pounds and p_m lowered until severe buckling occurred at 0.098 psig. Figs. 8 and 9 show this buckled state. The buckled region was very stable, but the unbuckled forward portion of the shell fluttered violently and was clearly observable on the side shown in Fig. 9.

Although the foregoing results form a rather obscure picture, there are a few pertinent results of a general nature. For the unbuckled shell, the largest amplitude of flutter occurred for p_m near zero and slightly negative and was always much larger on one side of the shell than on the other. The example of flutter-buckling interaction obtained in the tests of Ref. 1 was also of localized nature. In fact, it was also localized in the axial direction in that the maximum amplitude occurred near the downstream end on one side of the shell.

The data from the pressure test (Appendix E) showed that the maximum change in static pressure around the circumference of the shell was about 0.3 per cent of the free stream dynamic pressure

when M_∞ was 3. (It is perhaps significant to note here that this change in static pressure could be accounted for by a change in free stream Mach number of only 0.4 per cent, which is of the order of the variations to be expected in a wind tunnel). The increase in static pressure along the length of the shell was about the same. At the highest dynamic pressure used in these flutter tests, this corresponds to 0.010 psi and at the lowest, to 0.006 psi. On the other hand, at $M_\infty = 2.5$ and $q_\infty = 274$ psf (the free stream Mach number and dynamic pressure of the flutter-buckling example of Ref. 1), the static pressure on the shell increased from the upstream to the downstream end by about 1 per cent of q_∞ or 0.020 psi. These pressure variations, although seemingly very small, can become important when the shell internal pressure is near zero. The localized nature of the flutter in this near-buckling region probably results from these non-uniformities in the static pressure distribution over the shell.

2.3.6 Experimental limitations

As mentioned above, the cylindrical shell flutter seems to be extremely sensitive to small non-uniformities in pressure distribution over the shell when the pressure differential p_m is near zero. These small non-uniformities in pressure distribution are caused by small deviations in model shape and non-uniformities in wind tunnel flow. Consequently, it must be realized that the flutter obtained near zero pressure differential may not represent the flutter of a shell in a uniform stress state.

These considerations also imply a limitation on the accuracy of measuring the pressure differential p_m in this region. The numbers quoted are the measured differences between the shell

internal pressure and the static pressure as obtained from a static pressure orifice just upstream of the shell, and this static pressure represents only some sort of average of the pressure distribution over the shell.

2.4 Conclusions

Again as in most panel flutter experiments, it was found that the instability predicted by linear theory (an exponential increase of amplitude with increasing time) was unobservable. Only the limit cycle oscillations were observed and were defined as flutter when the power spectral density of the shell motion became sharp at only a few frequencies and the amplitude of motion became large. This flutter was a relatively mild oscillation except in the vicinity of buckling where it was quite violent in some cases. However, even for the worst of these cases, the wind tunnel experiences showed no great danger of destruction of models.

Almost all the flutter modes observed in these experiments were of the circumferentially travelling wave type. That is, the modes contained many waves around the circumference (of the order of 20), but they were not fixed in space. It was found that these flutter modes could be described by approximately equal amounts of sin $n\theta$ and cos $n\theta$ modes oscillating 90 degrees out of phase in time. This phenomenon appears to be a result of the nonlinear character of cylindrical shells. These flutter modes were standing waves in the longitudinal direction with zero, one, or two circumferential nodal lines between the ends of the shell depending on the testing conditions.

It was found in qualitative agreement with available theory that small amounts of internal pressurization were very stabilizing, but moderate amounts reduced stability to the unpressurized level. On the other hand, contrary to the theory, large amounts of internal pressurization completely stabilized the shells independent of axial load or previous permanent buckling deformations.

It was also found in qualitative agreement with the theory that axial compressive loading was slightly destabilizing for moderate amounts of internal pressurization. On the other hand, this loading was slightly stabilizing when the internal pressure was near zero or negative.

The unbuckled shell exhibited large amplitude flutter when the internal pressure was near zero or slightly negative. The largest amplitude occurred for internal pressures from 1/3 to 1/2 of the critical value required for buckling under radial external pressure loading. This large amplitude flutter was of a localized nature in that the amplitude of shell motion was much larger on one side of the shell than on the other. The fact that this large amplitude, localized flutter occurred near zero internal pressure leads one to suspect that its localized nature was mainly a consequence of the small non-uniformity in static pressure distribution over the shell. The shell completely buckled under radial external pressure loading was essentially stable.

Loading conditions that led to the diamond pattern buckling (moderate axial loading and low internal pressure) had a completely different effect on the flutter. The shell did not flutter as buckling was approached. Only after the diamond pattern buckles appeared did the shell flutter and then only on the unbuckled portions of the shell. This flutter was very violent.

The shell did not flutter at all either during or after the buckling process that resulted in the bellows shaped buckle (high internal pressure and large axial loading). However, when the internal pressure was returned to a low level, this buckled shell then fluttered with a larger amplitude than it had before it was buckled.

Hence, it appears that the large local curvatures encountered in the buckling of a cylindrical shell have a marked stabilizing effect on the shell locally. However, it must be emphasized that it also appears that the localized buckling usually encountered in practice significantly reduces the stability of any unbuckled regions of the shell.

III. COMPARISON WITH THEORY

3.1 Cylindrical Shell Vibration Frequencies

The cylindrical shell vibration data obtained by the methods described in Appendix D are compared with theoretical predictions satisfying various boundary conditions. This provides some insight into the quality of the experimental models, and in particular indicates what effective boundary conditions the shells really have for different kinds of vibrations. Some of the theory is briefly developed in the following.

3.1.1 "Freely supported" ends

Following Arnold and Warburton (Ref. 12), the boundary conditions

$$v = w = \frac{\partial^2 w}{\partial x^2} = N_x = 0 \quad \text{at} \quad x = 0 \text{ and } L, \tag{3.1}$$

are called "freely supported" ends. The vibration modes

$$\left.\begin{aligned} u(x, \theta, t) &= \cos \frac{m\pi x}{L} \cos n\theta \cos \omega t \\ v(x, \theta, t) &= \sin \frac{m\pi x}{L} \sin n\theta \cos \omega t \\ w(x, \theta, t) &= \sin \frac{m\pi x}{L} \cos n\theta \cos \omega t \end{aligned}\right\} \tag{3.2}$$

satisfy the boundary conditions (3.1) and provide an exact solution to the complete linearized partial differential equations governing deflections of a cylindrical shell. See for example, Ref. 13. However, for present purposes, the simplified Donnell's equations seem to be sufficiently accurate. These equations are given in Section 3.3.

The frequency equation that results from substituting the modal solutions (3.2) into Eqs. (3.10) with p = 0 is Eq. (3.16) and is repeated below for convenience.

$$\omega_{mn}^2 = \frac{1}{\rho_s h}\left\{ D\left[\left(\frac{m\pi}{L}\right)^2 + \left(\frac{n}{R}\right)^2\right]^2 + \left(\frac{m\pi}{L}\right)^2 \bar{N}_x + \left(\frac{n}{R}\right)^2 \bar{N}_\theta + \frac{Eh}{R^2}\,\frac{\left(\frac{m\pi}{L}\right)^4}{\left[\left(\frac{m\pi}{L}\right)^2 + \left(\frac{n}{R}\right)^2\right]^2}\right\}, \qquad (3.16)$$

where m is the number of axial half waves and n is the number of circumferential waves in the vibration mode.

3.1.2 "Fixed" ends

Following Arnold and Warburton (Ref. 14), the boundary conditions

$$u = v = w = \frac{\partial w}{\partial x} = 0 \qquad \text{at} \qquad x = 0 \text{ and } L \qquad (3.3)$$

are called "fixed" ends. Arnold and Warburton have developed approximate expressions for the natural frequencies of a cylindrical shell having these end conditions based on an energy approach. Forsberg (Ref. 15) has shown that these approximations are within a few percent of his "exact" calculations. Consequently, the Arnold Warburton expressions should be quite adequate for the comparison needed herein.

3.1.3 Approximate "Fixed" ends

Even though the Arnold and Warburton expressions mentioned above are only approximate, they are still rather cumbersome. Hence, it would seem advantageous to have a simpler theory for the "fixed" ends case, especially for large n, since this is the important region for shell flutter. To achieve this purpose, the problem is approached in the following manner. The eighth order Donnell's Eq. (3.11) with p = 0 is used to represent the shell, and the axial dependence of the radial displacement is approximated by the expression for the vibration of a clamped-clamped beam. That is,

$$w(x, \theta, t) = \sin n\theta \ \psi_m(x) \ \sin \omega t \tag{3.4}$$

where from Ref. 16,

$$\psi_m(x) = \cosh \mu_m x - \cos \mu_m x - k_m(\sinh \mu_m x - \sin \mu_m x) \tag{3.5}$$

where μ_m satisfies the transcendental equation

$$\cosh \mu_m L \cos \mu_m L = 1 \tag{3.6}$$

and

$$k_m = \frac{\sin \mu_m L + \sinh \mu_m L}{\cosh \mu_m L - \cos \mu_m L} \quad . \tag{3.7}$$

This approximation for w (x, θ, t) satisfies the zero deflection and slope boundary conditions

$$w = \frac{\partial w}{\partial x} = 0 \qquad \text{at} \qquad x = 0 \text{ and } L \quad , \tag{3.8}$$

but does not seem to satisfy any other special end conditions. Hence it can be expected that the approximation will be very poor for low values of the wave numbers m and n. However, the approximation may be quite reasonable for high values of m and n for which boundary conditions on u and v become relatively unimportant compared to those on w.

The assumed solution (3.4) does not satisfy Donnell's equation identically, but may be forced to satisfy it approximately in the Galerkin sense. That is, the solution (3.4) is substituted into Eq. (3.11), and the result is multiplied by $\psi_m(x)$, integrated from

x = 0 to L and the integrated result set equal to zero. (The various integrals involved are given in Ref. 17). This procedure yields the following frequency equation.

$$\omega_{mn}^2 =$$

$$\frac{\frac{\mu_m^4 Eh}{R^2} + D\left\{\mu_m^8 + 6\mu_m^4\left(\frac{n}{R}\right)^4 + \left(\frac{n}{R}\right)^8 + 4\left(\frac{n}{R}\right)^2\left[\mu_m^4 + \left(\frac{n}{R}\right)^4\right] k_m\mu_m\left[k_m\mu_m - \frac{2}{L}\right]\right\}}{\rho_s h\left[\mu_m^4 + \left(\frac{n}{R}\right)^4 + 2k_m\mu_m\left(\frac{n}{R}\right)^2\left|k_m\mu_m - \frac{2}{L}\right|\right]}$$

(3.9)

The theoretical predictions for the three foregoing cases are shown in Fig. 27 along with the experimental data for a 0.0040 inch thick shell. The constants used in the calculations were

ν = 0.35

ρ_s = 0.000833 lb sec^2/in^4

E = 16 million psi

R = 8.0 inches

L = 15.4 inches

For low values of the circumferential wave number n, the experimental data lies between the predictions for "freely supported" and "fixed" ends. This indicates that in this region the effective end conditions lie somewhere between the two idealized ones as might well be expected. For high values of n, these two theories approach each other and the experimental points seem to lie above both predictions. Some of this descrepancy between theory and experiment may be due to error in measuring the shell thickness h. As explained in Appendix A, this thickness measurement was an average value based on independent measurements of total shell weight, size and density of the electroplated copper and could conceivably be in error by as much as ten per cent. In the region of positive slope on the frequency versus n plots, the frequency is essentially linear with thickness, so that any error in thickness is reflected directly into error in frequency. The experimental points for m = 3 and 4 and large n were very difficult to obtain and could easily be in error both in frequency and value of n.

The prediction given by the expression for approximate "fixed" ends seems to be remarkably close to the Arnold and Warburton result. In particular, the two results merge together for high values of n. This indicates that use of the clamped-clamped beam functions for a flutter calculation should lead to a good approximation to the "fixed" ends type of boundary condition especially for large n.

This is further verified by considerations of the two-mode flutter solution discussed in Section 3.3.1a. There it is shown that when aerodynamic damping is neglected, the level of static pressure required for flutter is proportional to $(\omega_{2n}^2 - \omega_{1n}^2)$.

This parameter is plotted versus n in Fig. 28 for the three cases discussed above. The approximate "fixed" ends result is seen to be remarkably close to the Arnold and Warburton one. The figure also indicates how the two different types of boundary conditions would affect the flutter condition. The minimum ($\omega_{2n}^2 - \omega_{1n}^2$) occurs at n = 29 for "freely supported" ends and at n = 32 for "fixed" ends. The actual level of this minimum is higher for the "fixed" ends case by about 40 per cent.

3.2 Aerodynamic Theory

One of the most serious limitations in the theoretical foundation for the flutter of a cylindrical shell is still the aerodynamic theory. Almost all available theoretical predictions of cylindrical shell flutter involve some highly questionable assumptions about the nature of the aerodynamic forces involved. In some cases, this has led to rather contradictory results. For the case of supersonic flow, most of the controversial approximations involved in current work are associated either directly or indirectly with three dimensional effects. These effects will be explained in some detail in the following.

3.2.1 Three dimensional effects in inviscid flow

The simplest and easiest aerodynamic theory to employ in supersonic flutter calculations is of course the linear piston theory (neglecting the aerodynamic damping leads to one form of the even simpler so-called Ackeret theory, but for the purposes of this discussion, no distinction need be made between the two). Even if the shell curvature is negligible, the use of piston theory is questionable, since it is only rigorously valid for two dimensional deflections. Hence, the question of how good the piston theory approximation is may be interpreted as a question of how important the three dimensional effects are.

One of the easiest ways to obtain a quantitative answer to this question is to consider axially-directed supersonic flow over an infinitely long cylinder whose surface is deformed sinusoidally in space and is oscillating normal to itself. The linear potential solution

for this problem may be easily obtained (see for example, Ref. 7) and the predicted surface pressure may be compared to that from piston theory. The resulting expressions from the potential solution are summarized in Appendix F for convenience. Some aspects of this comparison have already been given by Krumhaar (Ref. 18) and Anderson (Ref. 19). Both show rather vividly that the surface pressures predicted by the two theories are no longer even approximately the same when the ratio between the axial and circumferential wave lengths of the surface deflection becomes large. Anderson shows results for an example in which the wall is stationary that are typical even when the wall is moving. When the aforementioned wave length ratio is large, the potential theory pressure terms are strongly attenuated and have a large phase shift away from the corresponding piston theory terms.

However, even though the two theories are radically different in this case, it is unwise to immediately conclude that piston theory is of no use. Some physical interpretation of the theoretical predictions will serve to illustrate why. Consider the following sketch of a portion of the cross section of the cylinder where the air flow is normal to the paper.

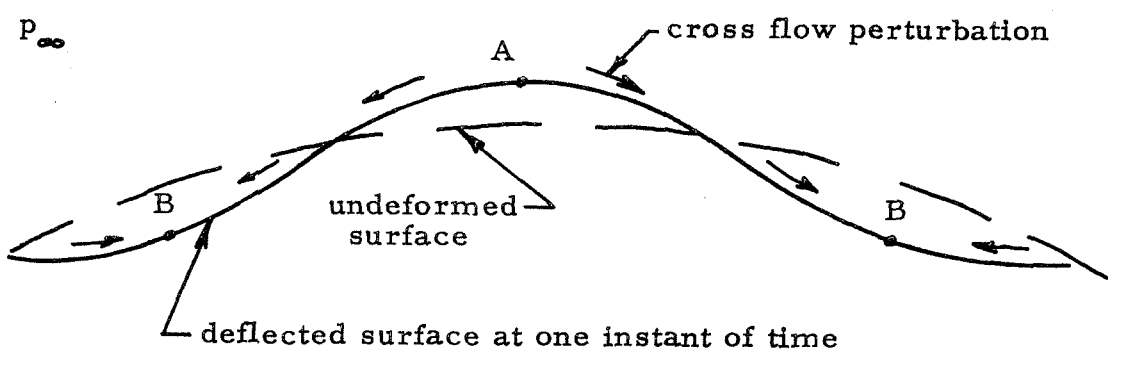

Sketch 1: Deflected surface of oscillating cylinder

According to the piston theory prediction, the wall pressure at point A will be larger than p_∞, the static pressure far from the cylinder, while at points B, it will be smaller than p_∞. Furthermore, since the theory is strictly two dimensional, it predicts no cross-flow between points A and B. On the other hand, it is apparent that the pressure difference between points A and B will produce some cross-flow and indeed the potential solution does yield this cross-flow. In effect, it is this cross-flow which relaxes the pressure difference between points A and B and hence results in a wall pressure far different from that given by piston theory. However, the potential theory probably predicts a larger cross-flow than that occurring in a real fluid because of viscous effects. This is a result of the fact that this cross-flow component must vanish on the surface of the cylinder. Furthermore, the relevant Reynolds number for these considerations may be proportional to the cross-flow component of velocity and to the circumferential wave length of the surface deflection. This type of Reynolds number is probably very small and hence the forgoing considerations may be very significant. Further verification of this effect would be desirable and could conceivably be obtained theoretically or experimentally.

3.2.2 Three dimensional effects in viscous flow

The forgoing discussion leads conveniently to consideration of another somewhat different three dimensional effect that is directly associated with the influence of viscosity. This one is most easily developed along the lines of boundary layer theory. The first work on this problem was carried out by Anderson and reported in Refs. 4 and 19.

His boundary layer was idealized as an annular region of uniform parallel subsonic flow between the cylindrical shell and the outer uniform supersonic flow. On the basis of this model, he was able to predict an attenuation in amplitude and a shift in phase of the pressure perturbations on either a stationary or oscillating wall with sinusoidal spatial dependence. The amount of attenuation and phase shift turned out to be strongly dependent on how three dimensional the shape of the surface deflection was and increased rapidly with this three dimensionality. However, inherent in this working model for the boundary layer was an ambiguity in choice of the thickness of and the Mach number in the subsonic layer. Subsequent work by Anderson (Ref. 5) indicates that his choice for this thickness in the earlier work was probably too large and consequently led to an over prediction of the boundary layer influence by an order of magnitude.

As mentioned in the introduction, the author's calculations seem to substantiate this last result. These calculations were based on a somewhat different boundary layer model - that of a parallel shear flow with a velocity distribution given by the mean velocity profile in a turbulent boundary layer - from that of Anderson's. Complete details of these calculations and discussions of the results are given in Appendix G. The main parameter which governs the influence of the boundary layer in the linearized problem is the ratio of boundary layer thickness to streamwise (axial) wave length of the wall deflection. The boundary layer influence decreases as this parameter decreases. For cylindrical shell flutter with a large number of circumferential waves, the pertinent streamwise wave lengths of interest are very large with respect to the boundary layer thickness (at least for the experimental configurations reported herein), so that the influence of the boundary layer is probably negligible. It must be emphasized however that for the case of axisymmetric flutter for which the pertinent axial wave lengths may be quite small, the influence of the boundary layer could still be important.

3.3 Flutter Boundaries

As mentioned in the introduction, no detailed comparison between experiment and theory for the supersonic flutter of a cylindrical shell has been available. Only a few qualitative remarks on this subject have appeared in the literature and as a result, some serious misconceptions have been perpetuated. In the following two sections, an attempt will be made to correct this situation in so far as available data and current theoretical techniques make it possible.

An extensive review of the panel flutter problem and analyses dealing with the flutter of cylindrical shells is given by Fung in Ref. 20. The subject is brought up to date again by Fung in Ref. 2, and an even more current review is that of Johns in Ref. 21.

In the following discussions, only flutter analyses pertaining to a finite cylindrical shell will be considered. Infinite length shell analyses are excluded on the grounds that their applicability to finite shells has not been proven. Furthermore, in the light of the experimental experiences, the exceedingly large critical shell thicknesses that result from such analyses make them rather suspect.

Of the available analyses pertaining to a finite shell, Voss's (Ref. 6) is probably the most extensive and will be used as a guide for the following studies. Following Voss, the problem is conveniently separated into two main categories. These are the low n case or membrane-type flutter and the high n case or plate-type flutter.

Early work indicated that the low n case would be the most critical for design purposes (see for example, Ref. 20). However, Voss gave an example in which just the opposite could be true and concluded that both cases should always be considered. In the following, the high n case is treated in greater detail than the low n one, since it was the only type of flutter observed in the experiments.

3.3.1 Flutter with many circumferential waves

As pointed out by Voss, the shallow shell type theory is sufficiently accurate for analyzing shell flutter with many circumferential waves. Hence, Donnell's cylinder equations are used in the form

$$D\nabla^4 w + \rho_s h \frac{\partial^2 w}{\partial t^2} + p = \bar{N}_x \frac{\partial^2 w}{\partial x^2} + \frac{\bar{N}_\theta}{R^2} \frac{\partial^2 w}{\partial \theta^2} - \frac{1}{R} \frac{\partial^2 F}{\partial x^2} \tag{3.10a}$$

$$\nabla^4 F = \frac{Eh}{R} \frac{\partial^2 w}{\partial x^2} \tag{3.10b}$$

where F is the usual stress function, or in the form

$$D\nabla^8 w + \nabla^4 \left[\rho_s h \frac{\partial^2 w}{\partial t^2} + p \right] = \nabla^4 \left[\bar{N}_x \frac{\partial^2 w}{\partial x^2} + \frac{\bar{N}_\theta}{R^2} \frac{\partial^2 w}{\partial \theta^2} \right] + \frac{Eh}{R^2} \frac{\partial^4 w}{\partial x^4} \,. \tag{3.11}$$

See Fig. 29 for shell geometry and coordinate system. The aerodynamic pressure which comes in through the p term in these equations is assumed to depend linearly on w. Structural damping is neglected, since it is not expected to be important for this type of flutter.

A modal solution to Eqs. (3.10) is assumed in the form

$$w(x, \theta, t) = \sin n\theta \, e^{i\omega t} \sum_{m=1}^{N} c_m \sin \alpha_m x \qquad (3.12)^*$$

where $\alpha_m = m\pi / L$. In general, ω will be complex in such a solution indicating that the amplitude is either growing or decaying exponentially with time. The condition for which the imaginary part of ω vanishes corresponds to a sustained oscillation in time and is defined as the flutter boundary.

The form of the solution (3.12) implies the satisfaction of the "freely supported" boundary conditions

$$v = w = \frac{\partial^2 w}{\partial x^2} = N_x = 0 \quad \text{at} \quad x = 0 \text{ and } L \, . \qquad (3.13)$$

---

* The common complex notation is used, so that the physical deflection is the real part of this expression.

The aerodynamic pressure term is conveniently put in the form

$$p(x, \theta, t) = \sin n\theta \, e^{i\omega t} \sum_{m=1}^{N} \left[p_{sm} \sin \alpha_m x + p_{cm} \cos \alpha_m x \right] c_m \quad (3.14)$$

where p_{sm} and p_{cm} are complex constants determined from the aerodynamic theory to be used in the analysis.

The solution (3.12) is substituted into the compatibility equation (3.10b) and the particular solution for F is obtained. Finally, w, F and p are substituted into the equilibrium equation (3.10a), which is then satisfied in the Galerkin sense by multiplying by $\sin \alpha_\ell x$, integrating over x from 0 to L and setting the result equal to zero. This procedure yields N homogeneous algebraic equations for the N modal amplitudes c_m in the form

$$\sum_{m=1}^{N} \left\{ \left[\rho_s h (\omega_{mn}^2 - \omega^2) + p_{sm} \right] \delta_{m\ell} + p_{cm} \Delta_{m\ell} \right\} c_m = 0 , \qquad \ell = 1, 2 \ldots N \quad (3.15)$$

where

$$\omega_{mn}^2 = \frac{1}{\rho_s h} \left\{ D \left[\alpha_m^2 + \left(\frac{n}{R}\right)^2 \right]^2 + \alpha_m^2 \bar{N}_x + \left(\frac{n}{R}\right)^2 \bar{N}_\theta + \frac{Eh}{R^2} \frac{\alpha_m^4}{\left[\alpha_m^2 + \left(\frac{n}{R}\right)^2 \right]^2} \right\} , \qquad \delta_{m\ell} = \begin{cases} 1 & \text{for } m = \ell \\ 0 & \text{for } m \neq \ell \end{cases} \quad (3.16)$$

and

$$\Delta_{m\ell} = \begin{cases} \dfrac{4\ell}{\pi(\ell^2 - m^2)} & \text{for } m + \ell \text{ odd} \\ \\ 0 & \text{otherwise} \end{cases} .$$

For the particular shell configuration used in the experiments, the membrane stress resultants $\bar{N}_x$ and $\bar{N}_\theta$ are

$$\bar{N}_x = -\frac{P_x}{2\pi R} , \qquad \bar{N}_\theta = Rp_m \tag{3.17}$$

where P_x is the total axial compressive load applied to the shell and p_m is the pressure differential across the shell skin.

The necessary and sufficient condition for the existence of a nontrivial solution to Eqs. (3.15) is that the determinant of the coefficients of the c_m's must vanish. This determinant is complex in general, and hence both the real and imaginary parts must vanish simultaneously. This yields two conditions for the determination of two eigenvalues. The constants obtained from the experimental conditions and used in the calculations to follow are

E	=	16 million psi
h	=	0.004 inches
L	=	15.4 inches
M_∞	=	3
R	=	8 inches
T_{t_∞}	=	120^o F
ν	=	0.35
ρ_s	=	0.000833 lb sec^2/in^4

The remaining unspecified variables in the determinant are p_m, P_x, n, ω and p_∞ (p_∞ will be seen to come in through p_{sm} and p_{cm}). Hence p_m and P_x may be specified and ω and p_∞ determined such that p_∞ is a minimum with respect to n. These calculations are carried out for two forms of aerodynamic theory - piston theory and the potential theory of Leonard and Hedgepeth (Ref. 7).

3.3.1a Piston theory

Using the piston theory approximation

$$p = \gamma p_\infty \left[\frac{1}{a_\infty} \frac{\partial w}{\partial t} + M_\infty \frac{\partial w}{\partial x} \right] \tag{3.18}$$

with the form of the solution (3.12) yields

$$p_{sm} = i \frac{\gamma \omega}{a_\infty} p_\infty \quad , \quad p_{cm} = \gamma M_\infty \alpha_m p_\infty \ . \tag{3.19}$$

As shown by Voss and others, Eqs. (3.15) can be solved in closed form when only two modes are considered (N = 2), and the results are especially revealing. Proceeding thusly yields the following conditions for flutter

$$\omega = \sqrt{\frac{\omega_{1n}^2 + \omega_{2n}^2}{2}} \tag{3.20a}$$

$$p_\infty = \frac{\rho_s h(\omega_{2n}^2 - \omega_{1n}^2)}{2\gamma\sqrt{\frac{64\, M_\infty^2 \alpha_1^2}{9\pi^2} - \frac{\omega^2}{a_\infty^2}}} \tag{3.20b}$$

In this case, the flutter frequency is the root mean square of the two modal frequencies ω_{1n} and ω_{2n}, and the static pressure at flutter is proportional to the difference between the squares of these two frequencies. The second term in the square root in Eq. (3.20b) is due solely to aerodynamic damping. For low enough flutter frequencies, this term may be neglected, and the minimum in p_∞ then corresponds to the minimum in $(\omega_{2n}^2 - \omega_{1n}^2)$. Voss and others have shown that when $n/R \gg \pi/L$, this minimum occurs at

$$n = n_{min} \approx 2.90\,(1 - \nu^2)^{1/6} \left[\left(\frac{R}{L}\right)\left(\frac{R}{h}\right)\right]^{1/3} \tag{3.21}$$

Using the constants shown on page 41 yields $n_{min} = 28$ and $p_{\infty\,min} = 0.30$ psia. This value of p_∞ is very close to the range of p_∞'s over which flutter was actually observed in the experiments.

The two mode solution also affords an especially interesting interpretation of the effect of the internal pressure differential p_m. It may be seen from the modal frequency expression (3.16) that the difference of squares ($\omega_{2n}^2 - \omega_{1n}^2$) is independent of p_m. Hence, within the framework of the two mode solution with aerodynamic damping neglected, the pressure differential p_m has no effect on the flutter boundary. On the other hand, the modal frequencies increase rapidly with p_m when n is large and consequently so does the flutter frequency ω. As a result the neglecting of aerodynamic damping will no longer be a good approximation when p_m is large. The importance of these considerations is revealed clearly in the sketch below where the minimum p_∞ from Eq. (3.20b) is plotted versus p_m along with the result obtained by neglecting aerodynamic damping.

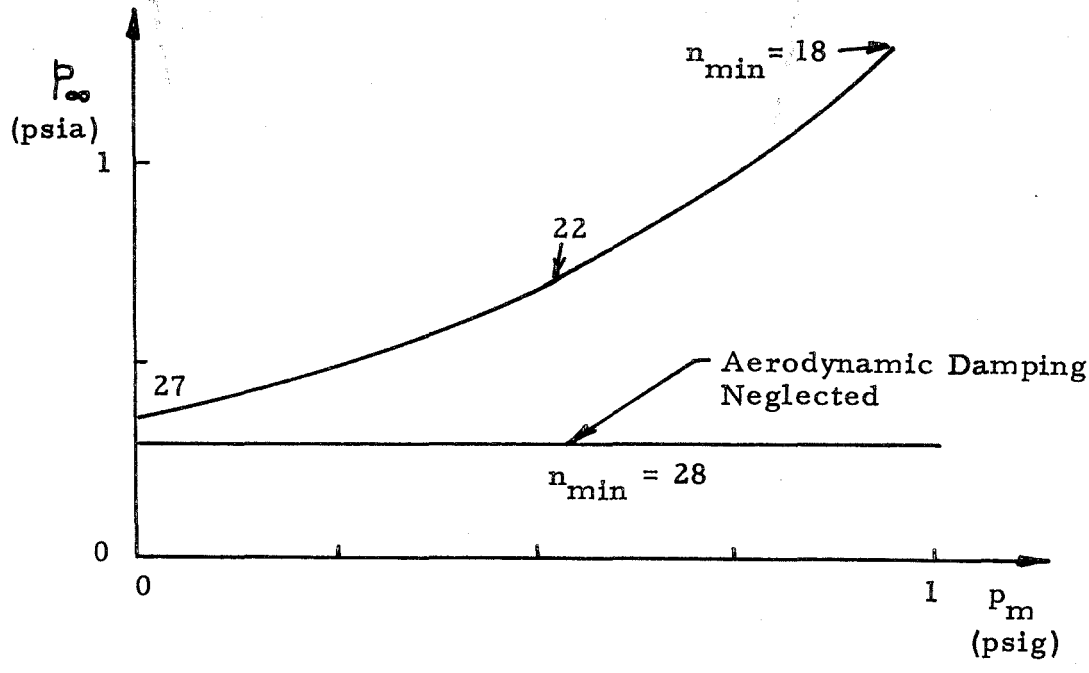

Sketch 2: Two Mode-Piston Theory Flutter Boundaries

Hence, within the approximation of the two mode solution, internal pressurization of the shell provides no direct stabilizing influence on flutter. This is due solely to the fact that for the particular shell configuration considered in this work, the internal pressurization produces no axial stress in the shell. Clearly if a hydrostatic type of internal pressure were considered, it would be directly stabilizing through the $\alpha_m^2 \bar{N}_x$ terms in the modal frequency expressions.

It is seen then that the stabilizing influence of internal pressure shown in Sketch 2 is directly attributable to the aerodynamic damping. Consequently, the flutter boundary predicted by this theory for high values of p_m is strongly influenced by the estimation of aerodynamic damping. This fact has already been pointed out by Kobayashi (Ref. 9), and will be discussed again in connection with possible explanations for discrepancy between theory and experiment.

The results from a four mode calculation using piston theory are shown in Fig. 30 along with the experimental flutter boundary. The values of n shown corresponded to a minimum in p_∞. These values of n correspond very closely to those actually observed in the experiments, and the trend of n decreasing with increasing p_m was also verified. However, this apparent agreement may be somewhat fortuitous and requires further interpretation. This will be given in Section 3.4.

Six mode calculations were carried out to verify the convergence and resulted in changes of only a few per cent in either p_∞ or ω. Some of these results are tabulated in Tables V and VI for $p_m = 0$. The results for non-zero p_m were very similar.

Fig. 31 shows an example of the flutter mode amplitude and phase angle variations in the axial direction. This example is typical of all the piston theory results even for non-zero p_m.

3.3.1b Potential theory

The potential theory solution due to Leonard and Hedgepeth was also used to predict flutter. This solution is for supersonic axial flow over an infinitely long cylindrical shell whose surface is oscillating in a standing wave pattern. The results are summarized in Appendix F. The pressure coefficients p_{sm} and p_{cm} are extremely complicated, and as a result, the flutter calculations become much more difficult than for piston theory.

The following method of calculation was used with the most success. The frequency term ω in Eqs. (3.15) was replaced by $\Omega = \omega - i\beta$ and the complex roots Ω of the complex determinant were followed as p_∞ was increased by small increments. The procedure was begun at $p_\infty = 0$ for which the roots were known to be $\Omega_m = \omega_{mn}$. The condition for flutter is that the damping factor β in one of the roots vanish (as β changes sign).

The results of such a calculation using six modes for $p_m = 0$ and $n = 20$ are exhibited in Figs. 32 and 33. The real part ω_m of each root is seen to decrease as p_∞ increases, and the imaginary part $-\beta_m$ is seen to first go positive and then come back and pass through zero. For this example, the first crossing occurs for the root which corresponds to the $m = 3$ mode at $p_\infty = 1.61$.

Although not shown, the m = 1 and 4 roots crossed at much higher values of p_∞. The first crossings for n = 21 and 22 also occurred for the m = 3 mode, whereas for n = 17, 18 and 19, it was the m = 2 mode.

The approximate values of ω and p_∞ for first flutter obtained by the forgoing method for each value of n were used as the first guesses in a final iteration procedure to evaluate them accurately. The more accurate values were then used for the determination of the modal amplitudes c_m. Another iteration procedure was used to follow these eigenvalues as p_m was increased in small steps. Finally, eight mode calculations were carried out to check the convergence for a few examples. The resulting changes in ω and p_∞ were less than one per cent. Some of the results from the six mode calculations at $p_m = 0$ are tabulated in Table VII, and the lowest values of p_∞ for non-zero p_m are plotted in Fig. 30.

Fig. 34 shows a typical example of the flutter mode amplitude and phase angle variations in the axial direction. A small amount of internal pressurization p_m seems to smoothen out the flutter mode and reduce the amount of phase shift along the shell. Further increases in p_m seem to have little effect. The peculiar waviness exhibited by the flutter mode for $p_m = 0$ was verified by an eight mode calculation.

The potential solution flutter boundaries are seen to be quite a bit higher than the piston theory ones. This is probably due to the fact mentioned in Section 3.2.1 that the potential solution pressure terms for the lowest modes are appreciably smaller than

the corresponding piston theory terms. On the other hand, both theories seem to predict the same stabilizing influence of the internal pressure p_m. This stabilizing influence must be due mainly to the increasing effect of aerodynamic damping associated with the increase in flutter frequency. See, for example, the discussion in Section 3.3.1a.

The values of n predicted by the potential theory are somewhat smaller than those for piston theory. As noted in Section 3.2.1, the potential theory pressure terms become strongly attenuated as n increases, whereas the piston theory is independent of n. Hence, lower values of n result from the potential theory.

It must be concluded from Fig. 30 that cylindrical shell flutter with many circumferential waves was actually observed in the experiment at a somewhat lower level of p_∞ than predicted by either of the theories considered here. In that narrow sense, the theory appears to be slightly unconservative. However, it is worth noting that the discrepancy between theory and experiment is not one of orders of magnitude as indicated by some of the literature. Furthermore, the point of view for comparing the two assumed in this work - that of comparing p_∞ levels for a particular shell geometry - is by far the most discriminating one.

A number of possible explanations for some of the apparent discrepancy between theory and experiment may be suggested. As mentioned in Section 3.2.1, the potential theory solution may actually overpredict the effect of three dimensionality of the flutter motions, so that piston theory may be the better approximation. On the other hand, both theories may overpredict

the influence of aerodynamic damping, and in turn, the stabilizing influence of the internal pressure p_m. Fig. 30 shows that p_m actually was stabilizing in the experiment but only above $p_m \approx 1$ psig.

The fact that the flutter phenomenon observed in the experiment was strongly influenced by nonlinear effects has already been emphasized in Section 2. Hence, it seems natural to ask whether or not the phenomenon may exist below the boundary predicted by linear theory because of nonlinear effects. An attempt will be made to answer this question in Section 3.4.

3.3.2 Axisymmetric flutter

For the low n or membrane type flutter of a finite shell, Voss (Ref. 6) has shown that n = 0 is most critical. Consequently, only this case need be considered here.

Krumhaar (Ref. 22) gives an exact solution for this case for a "freely supported" shell using piston theory. Flutter boundaries for structural damping ratios γ_1 of 0 and 0.0005 were calculated from these exact results and are shown in Fig. 30. Unfortunately, Krumhaar's results do not go high enough in his generalized eigenvalue A to provide results for higher values of structural damping. However, it is clear from Fig. 30 that the structural damping is extremely stabilizing to this kind of flutter. The amount of damping present in the experimental models for axisymmetric shell motions was probably at least 0.005. Voss has shown further that inclusion of the mid-plane inertia, which is neglected in Krumhaar's work, is also strongly stabilizing.

Hence, the combined effects of realistic amounts of structural damping and mid-plane inertia would push the axisymmetric flutter boundary in Fig. 30 far above the experiment. This would then explain why this kind of flutter was not observed in the experiments.

It is perhaps worth mentioning here that there seems to be an error in Krumhaar's application of his results to the initial GALCIT experiment. In Section 4.1 of Ref. 22, he calculates stability boundaries (thickness ratios required to prevent flutter versus Mach number) for an unpressurized copper cylinder with $L/R = 2$ at 50,000 feet altitude using shell properties from the experiment. These results are perfectly all right, of course. However, in Section 4.5, he states that the "tunnel was adjusted to the 50,000 feet altitude atmospheric conditions". This is completely misleading because it was impossible to make such an adjustment in the wind tunnel referred to there. That is, the 50,000 feet altitude values of a_∞, p_∞, and ρ_∞ could not be achieved simultaneously in the tunnel.

Therefore, Krumhaar's conclusion that his results are in conflict with the experiment seems to be incorrect. In fact, just the opposite is true. That is, if Krumhaar's results are applied to a 0.0060 inch thick shell (the shell used in the first GALCIT experiment, see Ref. 1) in the way outlined herein, the critical value of p_∞ that results is far beyond the capability of the wind tunnel. In that sense, his theory actually agrees with the experiment, since no axisymmetric flutter was observed in the test.

3.4 Limiting Amplitudes of Flutter

In order to answer the question posed in Section 3.3.1 b as to whether or not finite amplitude flutter may exist below the critical boundary for infinitesimal disturbances, a nonlinear analysis had to be developed. The equations that result from the well-known approximations of Donnell's shallow-shell theory are used for this purpose. These equations, commonly called Marguerre's equations, are (see Ref. 23)

$$D\nabla^4 w + \rho_s h \frac{\partial^2 w}{\partial t^2} + p = \overline{N}_x \frac{\partial^2 w}{\partial x^2} + \frac{\overline{N}_\theta}{R^2} \frac{\partial^2 w}{\partial \theta^2} - \frac{1}{R} \frac{\partial^2 F}{\partial x^2}$$

$$+ \frac{1}{R^2}\left[\frac{\partial^2 w}{\partial x^2} \frac{\partial^2 F}{\partial \theta^2} + \frac{\partial^2 w}{\partial \theta^2} \frac{\partial^2 F}{\partial x^2} - 2 \frac{\partial^2 w}{\partial x \partial \theta} \frac{\partial^2 F}{\partial x \partial \theta}\right] \qquad (3.22a)$$

and

$$\nabla^4 F = \frac{Eh}{R} \frac{\partial^2 w}{\partial x^2} - \frac{1}{R^2}\left[\frac{\partial^2 w}{\partial x^2} \frac{\partial^2 w}{\partial \theta^2} - \left(\frac{\partial^2 w}{\partial x \partial \theta}\right)^2\right] \qquad (3.22b)$$

where w is the radial deflection and F is the usual stress function. See Fig. 29 for coordinate system and shell geometry. The aerodynamic pressure term p is approximated by the piston theory expression

$$p = \gamma p_\infty \left[\frac{1}{a_\infty} \frac{\partial w}{\partial t} + M_\infty \frac{\partial w}{\partial x}\right] . \qquad (3.18)$$

A two mode solution for these equations is assumed in the form

$$w(x, \theta, t) = \sin n\theta \left(a_1(t) \sin \alpha x + a_2(t) \sin 2\alpha x \right) + \frac{n^2}{4R} \left[a_1(t) \sin \alpha x + a_2(t) \sin 2\alpha x \right]^2 \qquad (3.23)$$

where $\alpha = \pi/L$. The square bracketed terms were not present in the linear solution, but must be included here in order to satisfy the periodic continuity condition on the circumferential displacement v. See for example Ref. 24.

Substitution of Eq. (3.23) into the compatibility equation (3.22b) allows the latter to be solved for F. The resulting expressions for w and F, imply the satisfaction of the following boundary conditions:

(a) The displacements u, v and w, and their derivatives satisfy periodicity conditions of the form

$$v(x, \theta, t) = v(x, \theta + 2\pi, t)$$

(b) The radial displacement w goes to zero identically at the ends of the shell, i.e., at $x = 0$ and L.

(c) The boundary conditions for a shell having "freely-supported" ends are satisfied to a first approximation. In other words, the linear terms in the expression for N_x, M_x and v go to zero at the ends of the shell, but the nonlinear terms involving a_1^2, $a_1 a_2$ and a_2^2, etc. do not vanish there.

Finally, the expressions for w, F and p are substituted into Eq. (3.22a) and a Galerkin procedure is used to obtain two nonlinear ordinary differential equations for the modal amplitudes a_1 and a_2. The expressions $\partial w/\partial a_1$ and $\partial w/\partial a_2$ are used as the weighing functions in the Galerkin procedure. In semi-nondimensional form*, the resulting coupled equations (within order ε^2)** are

$$\frac{d^2\xi}{dt^2} + \Delta \frac{d\xi}{dt} + \omega_{1n}^2 \xi + \frac{1}{8}\varepsilon\left\{\xi\left[3\left(\frac{d\xi}{dt}\right)^2 + 2\left(\frac{d\eta}{dt}\right)^2\right] + \left[\frac{d^2\xi}{dt^2} + \Delta \frac{d\xi}{dt}\right]\left[3\xi^2 + 2\eta^2\right] + 4\eta\left[\xi \frac{d^2\eta}{dt^2} + \frac{d\xi}{dt}\frac{d\eta}{dt}\right] + 4\Delta\xi\eta \frac{d\eta}{dt}\right\} -$$

$$\varepsilon\,\xi\left[a\xi^2 + b\eta^2\right] - f\eta\left[1 + \frac{1}{5}\varepsilon\left(\xi^2 + \frac{4}{7}\eta^2\right)\right] = 0 \qquad (3.24a)$$

---

* It was not convenient to nondimensionalize the time t, since each of the equations has a different natural time scale.

** Terms with coefficients of order ε^2 arise naturally from the forgoing derivation but are neglected here. These terms are of the form $\xi\eta^4$, $\xi^2\eta^3$, etc., so that the approximation is justified for ξ and η up to and including order 1.

$$\frac{d^2\eta}{dt^2} + \Delta\frac{d\eta}{dt} + \omega_{2n}{}^2\eta + \frac{1}{8}\varepsilon\left\{\eta\left[3\left(\frac{d\eta}{dt}\right)^2 + 2\left(\frac{d\xi}{dt}\right)^2\right] + \left[\frac{d^2\eta}{dt^2} + \Delta\frac{d\eta}{dt}\right]\left[3\eta^2 + 2\xi^2\right] + 4\xi\left[\eta\frac{d^2\xi}{dt^2} + \frac{d\xi}{dt}\frac{d\eta}{dt}\right] + 4\Delta\xi\eta\frac{d\xi}{dt}\right\} -$$

$$\varepsilon\eta\left[16\,c\eta^2 + b\xi^2\right] + f\xi\left[1 + \frac{1}{5}\varepsilon\left(\xi^2 + \frac{4}{7}\eta^2\right)\right] = 0 \quad , \qquad (3.24b)$$

where the nondimensional modal amplitudes are

$$\xi = \frac{a_1}{h} \quad , \qquad \eta = \frac{a_2}{h} \quad ,$$

and the (small) nonlinearity parameter is

$$\varepsilon = \left(\frac{n^2 h}{R}\right)^2 \quad .$$

The linear undamped natural frequencies of the two modes are given by

$$\omega_{mn}{}^2 = \frac{1}{\rho_s h}\left\{D\left[(m\alpha)^2 + \left(\frac{n}{R}\right)^2\right]^2 + \frac{n^2 p_m}{R} + \frac{Eh}{R^2}\frac{(m\alpha)^4}{\left[(m\alpha)^2 + \left(\frac{n}{R}\right)^2\right]^2}\right\} \quad , \quad m = 1,\ 2 \ . \qquad (3.25)$$

The parameters

$$a = \frac{E\sigma^4}{\rho_s R^2}\left[\frac{1}{(1+\sigma^2)^2} - \frac{1}{16} - \frac{\varepsilon}{12(1-\nu^2)}\right]$$

$$b = \frac{E\sigma^4}{\rho_s R^2}\left[\frac{5}{2(1+\sigma^2)^2} + \frac{10}{(1+4\sigma^2)^2} - \frac{1}{4} - \frac{81}{16(4+\sigma^2)^2} - \frac{1}{16(4+9\sigma^2)^2} - \frac{41\,\varepsilon}{48(1-\nu^2)}\right]$$

$$c = \frac{E\sigma^4}{\rho_s R^2}\left[\frac{1}{(1+4\sigma^2)^2} - \frac{1}{16} - \frac{\varepsilon}{12(1-\nu^2)}\right]$$

where $\sigma = \alpha R/n$, depend only on the shell properties and mode shapes. The aerodynamic influence comes in through the two parameters

$$f = \frac{8\gamma M_\infty p_\infty}{3\rho_s L h}$$

$$\Delta = \frac{\gamma p_\infty}{\rho_s h a_\infty} .$$

Eqs. (3.24) are too complicated to be solved completely, but may be solved approximately by use of the method of Krylov and Bogoliubov, often called "The Method of Averaging". The experimental experiences indicate that the flutter motion is nearly sinusoidal in time, so that if Eqs. (3.24) are a reasonable approximation to the physical phenomenon, they should admit limit cycle oscillations. Hence solutions to these equations are sought in the form

$$\xi = A(t) \sin\left[\omega t + \varphi_1(t)\right] \tag{3.26a}$$

$$\eta = B(t) \sin\left[\omega t + \varphi_2(t)\right] \tag{3.26b}$$

where $A(t)$, $B(t)$, $\varphi_1(t)$ and $\varphi_2(t)$ are slowly varying functions of time. The second order differential Eqs. (3.24) are transformed into four first order equations by differentiating Eqs. (3.26) twice and imposing the subsidiary conditions

$$\frac{dA}{dt} \sin \theta_1 + \frac{d\varphi_1}{dt} A \cos \theta_1 = 0 \tag{3.27a}$$

$$\frac{dB}{dt} \sin \theta_2 + \frac{d\varphi_2}{dt} B \cos \theta_2 = 0 \quad , \tag{3.27b}$$

where $\theta_1 = \omega t + \varphi_1$ and $\theta_2 = \omega t + \varphi_2$. Then

$$\frac{d^2\xi}{dt^2} = \frac{dA}{dt}\,\omega\cos\theta_1 - A\omega\left(\omega + \frac{d\varphi_1}{dt}\right)\sin\theta_1 \quad , \qquad (3.28a)$$

$$\frac{d^2\eta}{dt^2} = \frac{dB}{dt}\,\omega\cos\theta_2 - B\omega\left(\omega + \frac{d\varphi_2}{dt}\right)\sin\theta_2 \quad , \qquad (3.28b)$$

and these expressions are then substituted into Eqs. (3.24).

The resulting equations exhibit a basic period of 2π in both θ_1 and θ_2. The quantities A, B, φ_1 and φ_2 were assumed to be slowly varying functions of time and so should change very little over one cycle of this basic motion. Hence, they are replaced by their averages over one cycle and the equations are integrated from 0 to 2π in either θ_1 or θ_2. This procedure yields the following equations for the quantities $d\bar{A}/dt$, $d\bar{B}/dt$, $d\bar{\varphi}_1/dt$ and $d\bar{\varphi}_2/dt$ (where the bars denote averages over one cycle).

$$2\omega\frac{d\bar{A}}{dt}\left[1 + \frac{1}{8}\varepsilon\left(\frac{3}{2}\bar{A}^2 + \bar{B}^2\right)\right] + K_1(\bar{A}, \bar{B}, \bar{\varphi}, \omega) = 0 \qquad (3.29a)$$

$$2\omega\frac{d\bar{B}}{dt}\left[1 + \frac{1}{8}\varepsilon\left(\bar{A}^2 + \frac{3}{2}\bar{B}^2\right)\right] + K_2(\bar{A}, \bar{B}, \bar{\varphi}, \omega) = 0 \qquad (3.29b)$$

$$2\omega\bar{A}\,\frac{d\bar{\varphi}_1}{dt}\left[1 + \frac{1}{8}\varepsilon\left(\frac{3}{2}\bar{A}^2 + \bar{B}^2\right)\right] + \frac{1}{2}\varepsilon\,\omega\,\bar{A}\bar{B}^2\,\frac{d\bar{\varphi}_2}{dt} +$$

$$K_3(\bar{A}, \bar{B}, \bar{\varphi}, \omega) = 0 \qquad (3.29c)$$

$$2\omega\bar{B}\ \frac{d\bar{\varphi}_2}{dt}\left[1+\frac{1}{8}\varepsilon(\bar{A}^2+\frac{3}{2}\bar{B}^2)\right]+\frac{1}{2}\varepsilon\omega\bar{A}^2\bar{B}\ \frac{d\bar{\varphi}_1}{dt}+$$

$$K_4(\bar{A},\ \bar{B},\ \bar{\varphi},\omega)\ =\ 0 \qquad (3.29d)$$

where K_1 to K_4 are given below. For steady state oscillations, $d\bar{A}/dt$, $d\bar{B}/dt$, $d\bar{\varphi}_1/dt$ and $d\bar{\varphi}_2/dt$ must all vanish. Hence, this procedure yields the following set of four algebraic equations for the four unknowns $\bar{A}$, $\bar{B}$, $\bar{\varphi}$ and ω.

$$K_1 = \Delta\omega\bar{A}+\frac{1}{4}\varepsilon\bar{A}\left\{\frac{1}{2}\Delta\omega\left[\frac{3}{4}\bar{A}^2+\bar{B}^2(1+\frac{1}{2}\cos 2\bar{\varphi})\right]-(b+\frac{1}{2}\omega^2)\times\right.$$

$$\left.\bar{B}^2\sin 2\bar{\varphi}\right\}-f\bar{B}\sin\bar{\varphi}\left[1+\frac{1}{5}\varepsilon(\frac{1}{4}\bar{A}^2+\frac{3}{7}\bar{B}^2)\right]\ =\ 0 \qquad (3.30a)$$

$$K_2 = \Delta\omega\bar{B}+\frac{1}{4}\varepsilon\bar{B}\left\{\frac{1}{2}\Delta\omega\left[\bar{A}^2(1+\frac{1}{2}\cos 2\bar{\varphi})+\frac{3}{4}\bar{B}^2\right]+\ (b+\frac{1}{2}\omega^2)\times\right.$$

$$\left.\bar{A}^2\sin 2\bar{\varphi}\right\}-f\bar{A}\sin\bar{\varphi}\left[1+\frac{1}{5}\varepsilon(\frac{3}{4}\bar{A}^2+\frac{1}{7}\bar{B}^2)\right]\ =\ 0 \qquad (3.30b)$$

$$K_3 = (\omega^2-\omega_{1n}^2)\bar{A}+\frac{1}{4}\varepsilon\bar{A}\left[3(a+\frac{1}{4}\omega^2)\bar{A}^2+(\omega^2+2b)\bar{B}^2\times\right.$$

$$(1+\frac{1}{2}\cos 2\bar{\varphi})+\frac{1}{4}\Delta\omega\bar{B}^2\sin 2\bar{\varphi}\left.\right]+f\bar{B}\cos\bar{\varphi}\left[1+\frac{3}{5}\varepsilon\times\right.$$

$$\left.(\frac{1}{4}\bar{A}^2+\frac{1}{7}\bar{B}^2)\right]\ =\ 0 \qquad (3.30c)$$

$$K_4 = (\omega^2 - \omega_{2n}^2)\,\bar{B} + \frac{1}{4}\varepsilon\,\bar{B}\left[(\omega^2 + 2b)\,\bar{A}^2\,(1 + \frac{1}{2}\cos 2\bar{\varphi}) + 3(16k + \frac{1}{4}\omega^2)\,\bar{B}^2 - \frac{1}{4}\Delta\omega\bar{A}^2 \sin 2\bar{\varphi}\right] - f\,\bar{A}\cos\bar{\varphi}\left[1 + \frac{3}{5}\varepsilon\,(\frac{1}{4}\,\bar{A}^2 + \frac{1}{7}\,\bar{B}^2)\right] = 0 \qquad (3.30d)$$

where $\bar{\varphi} = \bar{\varphi}_2 - \bar{\varphi}_1$.

Again it is desired to simulate the wind tunnel experimental results. This means that values of $\bar{A}$, $\bar{B}$, $\bar{\varphi}$ and ω that satisfy the forgoing equations are sought as functions of the aerodynamic pressure p_∞ for a given shell geometry, speed of sound and Mach number of the air-stream for various flutter modes, i.e., values of n. A procedure for doing this is outlined below.

3.4.1 Solving the algebraic equations

The aerodynamic pressure p_∞ comes into Eqs. (3.30) through the two parameters f and Δ, and for the case of no structural damping $\Delta = \kappa f$ where $\kappa = 3L/8M_\infty a_\infty$. Hence, the parameter f may be used to characterize the aerodynamic pressure. It is convenient for the calculations required herein to treat $\bar{A}$ as known and $\bar{B}$, ω, f and $\bar{\varphi}$ as unknowns. Letting the four component vector x_i (i = 1 to 4) denote the unknowns such that $x_1 = \bar{B}$, $x_2 = \omega$, $x_3 = f$ and $x_4 = \bar{\varphi}$, then Eqs. (3.30) are of the form

$$K_j(x_i) = 0 \qquad i, j = 1 \text{ to } 4 \quad . \qquad (3.31)$$

The solutions to these equations may be obtained numerically by a suitable generalization of Newton's method to four variables as follows. If x_{i_o} is a good initial approximation to the sought for solution x_i such that $x_{i_o} = x_i - \delta x_i$, then by expanding in Taylor series from x_{i_o} to x_i ,

$$K_j(x_{i_o}) + \left.\frac{\partial K_j}{\partial x_\ell}\right|_{x_i = x_{i_o}} \cdot \delta x_\ell \approx 0 \quad , \quad j = 1 \text{ to } 4 \quad , \quad \ell \text{ summed 1 to 4} \tag{3.32}$$

Now the δx_i may be found from Eqs. (3.32), since by definition $K_j(x_{i_o}) \neq 0$. When this is done, the new approximation for x_i is $x_{i_1} = x_{i_o} + (\delta x_i)$, and the forgoing procedure is repeated over again.

The initial solution used to start this process is that obtained from the linear flutter problem which is nothing but the linearization of Eqs. (3.30). This is easily seen to be

$$\left.\begin{aligned} \overline{A} &= \overline{B} \\ \omega^2 = \omega_o^2 &= \frac{\omega_{1n}^2 + \omega_{2n}^2}{2} \\ \overline{\varphi} = \overline{\varphi}_o &= \pi - \text{Arc sin}\,(\kappa \omega_o) \\ f = f_o &= \frac{\omega_{1n}^2 - \omega_{2n}^2}{2 \cos \overline{\varphi}_o} \end{aligned}\right\} \tag{3.33}$$

where $-\pi/2 < \text{Arcsin}\,(\kappa\omega_0) \leq \pi/2$. Initially $\bar{A}$ is taken to be a small number (of order .05), and the linear solution given above is used to start the iteration process. Thereafter, $\bar{A}$ is increased by a small amount and the solution for the previous value of $\bar{A}$ is used to start the iterations.

3.4.2 Stability of two mode steady state solution

The simplest approach to the study of the stability of the two mode steady state solution appears to be through the method of averaging and the relevant Eqs. (3.29). These equations may be put in the form

$$\frac{d\vec{x}}{dt} = A(\vec{x}) \quad , \tag{3.34}$$

where the vector $\vec{x}$ has the three components $\bar{A}$, $\bar{B}$, and $\bar{\varphi}$, and $A(\vec{x})$ has the three components G_1, G_2 and G_3 where (within order ε^2)

$$G_1 = -\frac{1}{2\omega}\left\{\Delta\omega\bar{A} + \frac{1}{4}\varepsilon\bar{A}\left[\frac{1}{4}\Delta\omega(\bar{B}^2\cos 2\bar{\varphi} - \frac{3}{2}\bar{A}^2) - \bar{B}^2(b+\frac{1}{2}\omega^2)\times \right.\right.$$

$$\left.\left.\sin 2\bar{\varphi}\right] - f\bar{B}\sin\bar{\varphi}\left[1 - \frac{11}{40}\varepsilon(\frac{1}{2}\bar{A}^2 + \frac{1}{7}\bar{B}^2)\right]\right\} \tag{3.35a}$$

$$G_2 = -\frac{1}{2\omega}\left\{\Delta\omega\bar{B} + \frac{1}{4}\varepsilon\bar{B}\left[\frac{1}{4}\Delta\omega(\bar{A}^2\cos 2\bar{\varphi} - \frac{3}{2}\bar{B}^2) + \bar{A}^2(b+\frac{1}{2}\omega^2)\times \right.\right.$$

$$\left.\left.\sin 2\bar{\varphi}\right] - f\bar{A}\sin\bar{\varphi}\left[1 + \frac{1}{40}\varepsilon(\bar{A}^2 - \frac{89}{14}\bar{B}^2)\right]\right\} \tag{3.35b}$$

$$G_3 = \frac{1}{2\omega}\left\{\omega_{2n}^2 - \omega_{1n}^2 + \frac{1}{4}\varepsilon\left[(3a - 2b + \frac{1}{2}\omega^2 - \frac{1}{4}\omega_{1n}^2 - \frac{1}{2}\omega_{2n}^2)\times\right.\right.$$

$$\bar{A}^2 + (2b - 48c - \frac{1}{2}\omega^2 + \frac{1}{4}\omega_{2n}^2 + \frac{1}{2}\omega_{1n}^2)\times$$

$$\left.\bar{B}^2 + (b + \frac{1}{2}\omega^2)(\bar{B}^2 - \bar{A}^2)\cos 2\bar{\varphi} + \frac{1}{4}\Delta\omega(\bar{A}^2 + \bar{B}^2)\sin 2\bar{\varphi}\right]$$

$$\left. + \frac{f\cos\bar{\varphi}}{\bar{A}\,\bar{B}}\left[\bar{A}^2 + \bar{B}^2 + \frac{1}{40}\varepsilon(\frac{53}{7}\bar{A}^2\bar{B}^2 - \frac{11}{7}\bar{B}^4 - \bar{A}^4)\right]\right\} \quad (3.35c)$$

The steady state solution $\vec{x}_o$ (i.e., $A(\vec{x}_o) = 0$) is perturbed slightly by letting

$$\vec{x} = \vec{x}_o + \vec{\xi} \quad (3.36)$$

where $\vec{\xi}$ has three components which represent perturbations to $\bar{A}$, $\bar{B}$ and $\bar{\varphi}$ respectively. Substituting this expression into Eq. (3.34) and noting that $d\vec{x}_o/dt = A(\vec{x}_o) = 0$ yields the variational equations

$$\frac{d\vec{\xi}}{dt} = \left.\frac{\partial A}{\partial \vec{x}}\right|_{\vec{x}=\vec{x}_o} \cdot \vec{\xi}\ , \quad (3.37)$$

where all nonlinear terms in the perturbation quantities $\vec{\xi}$ have been neglected. The substitution $\vec{\xi} = \vec{\xi}_o e^{\lambda t}$ reduces Eqs. (3.37) to the following eigenvalue problem for λ

$$\text{Det} \left| B - I\lambda \right| = 0 \quad , \qquad (3.38)$$

where I is the 3 x 3 identity matrix and $B = \frac{\partial A}{\partial \vec{x}}\Big|_{\vec{x} = \vec{x}_o}$ is a 3 x 3 real nonsymmetric matrix. Hence, the stability of the two mode steady state solution is completely determined by the nature of the eigenvalues of the matrix $\frac{\partial A}{\partial \vec{x}}\Big|_{\vec{x} = \vec{x}_o}$ provided it is non-singular. That is, if any of the eigenvalues of this matrix have positive real parts, the perturbations will increase with time and consequently the solution will be unstable.

The matrix involved in the forgoing formulation turned out to be extremely cumbersome. Consequently, it was practically impossible to derive an analytic criterion for stability, and a numerical approach was employed in the following way. At each step in $\bar{A}$ used in the calculations described in the last section, the components of the matrix $\frac{\partial A}{\partial \vec{x}}\Big|_{\vec{x} = \vec{x}_o}$ were evaluated. The eigenvalues for this matrix were then calculated and their real parts were examined.

3.4.3 Results

The preceding calculations were carried out for the following two cases:

(a) $p_m = 0 \quad , \quad n = n_{min} = 27$

(b) $p_m = 0.5$ psig , $n = n_{min} = 23$.

Note that n_{min} is the value of n which results in minimum static pressure for flutter for each value of p_m according to the two mode piston theory result. (See Eq. (3.20) and related discussion). The results for case (b) are shown in Figs. 35 and 36 and are very similar to those from case (a) as well.

It is especially interesting to note from Fig. 35 that the modal amplitude versus static pressure curves do not continue with positive slope indefinitely but rather bend back and continue indefinitely with negative slope. As one might well have expected from simple physical arguments, the stability calculations showed that only those portions of these curves with positive slope represent stable limit cycle oscillations. Hence, only the portions of the curves in Fig. 35 between points a(a') and b(b') represent physically realizable flutter motion.

Fig. 36 shows how the flutter frequency and phase angle between the two modes varies with amplitude. The flutter frequency is seen to decrease slowly with increasing amplitude. This is typical of the so-called "softening" type of nonlinearity and was to be expected here from previous work. (See for example Ref. 11). The phase angle between the two modes $\bar{\varphi}$ also decreases with increasing amplitude.

The fact that the modal amplitude versus static pressure curves do not continue indefinitely with positive slope leads to a rather interesting explanation of how the shell must flutter as the static pressure increases monotonically. To facilitate this explanation, results for various values of n near n_{min} are plotted versus the unnormalized aerodynamic parameter f in Fig. 37. This figure may be

interpretted as follows. As f (or static pressure p_∞) is increased for p_m held constant, nothing happens until f reaches the f_o corresponding to n = 23 or 1.406×10^5. At this point, given an initial disturbance (turbulence in the air-stream for example) the shell will begin to flutter with n = 23 and a frequency ω_o corresponding to n = 23. For f slightly larger than f_o, the amplitude of this oscillation will grow exponentially with time until the limiting amplitudes for $\bar{A}$ and $\bar{B}$ shown in Fig. 37 for n = 23 are reached. As f is further increased, these amplitudes will increase until f reaches 1.52×10^5 where the modal amplitude curves for n = 23 have vertical tangents. At this point, the flutter mode (i.e., value of n) must change or jump - probably to n = 22, since the curves for it are closest. This change in flutter mode would be accompanied by a change in flutter frequency and amplitude. It is clear from Fig. 37 that this type of change or jump would occur over and over again as f is increased continuously. It is also clear that some of the jumps in amplitude could be rather dramatic as for example when the flutter mode changes from n = 21 to 25 at $f = 1.58 \times 10^5$.

The experimental results shown in Fig. 14 seem to indicate that something like the forgoing process actually took place in the experiment. The actual stable limit cycle amplitudes shown in Fig. 37 (0.5 to 1.5) agree remarkably well with the experimental values. See for example, Fig. 19. However, the circumferentially travelling wave type of flutter, which was observed in the experiments, is not predictable with the forgoing analysis. An additional degree of freedom in the analysis would be required to obtain this phenomenon. This analysis is left for a later study.

The results, as for example shown in Fig. 35, revealed no appreciable region of stable limit cycles below the stability boundary for infinitesimal disturbances. Hence, within the framework of the two-mode piston theory limit cycle analysis, it may be concluded that for all practical purposes, flutter does not exist below the linear stability boundary.

3.5 Conclusions

The most serious limitation in the theoretical foundation for cylindrical shell flutter still seems to lie with the aerodynamic theory. The question as to what is the best theory to use for any particular configuration is still largely unanswered.

Within the framework of the present study, it appears that, contrary to what had previously been thought, the boundary layer does not play an important role in shell flutter with many circumferential waves. Furthermore, the detailed comparison between experiment and linearized theory presented herein indicates that:

(1) The pressurized cylindrical shells fluttered at a lower level of free stream energy than predicted by either piston theory or potential theory.

(2) Of these two theoretical results, that using piston theory appears to correspond closest to the experiment both in stability boundary and in critical values of circumferential wave number n.

(3) Both theories predict a larger stabilizing influence of the internal pressure differential p_m than observed in the experiment.

The results from the two mode limit cycle analysis indicate that for practical purposes cylindrical shell flutter does not occur below the stability boundary for infinitesimal disturbances.

The limit cycle amplitudes predicted by this analysis seem to agree very well with the experimentally observed ones. These results further indicate that the flutter amplitude, frequency and mode shape should change discontinuously (or jump) as the aerodynamic pressure is increased beyond the value for first flutter.

APPENDIX A

FLUTTER MODEL

A.1 General Description

The circular cylinder panel flutter model is shown installed in the wind tunnel in Figs. 1 and 2. The model is a sting mounted ducted body of revolution with the outer surface of the center section forming the thin test shell. The supporting structure consists of a nose, a center section which supports the flutter model and instrumentation, and the tail section which connects the center section to the wind tunnel sting. A ducted body allows a larger model size for a given cross sectional area without choking the wind tunnel.

The shape of the nose was chosen to best provide a rapid pressure recovery and uniform flow conditions over the center test section. Cowl number six of Ref. 8 was employed for this purpose. The complete nose section is composed of this cowl plus a four inch long straight cylindrical section forming the base of the cowl. Four symmetrically arranged static pressure orifices are located near the downstream end of this base. These were used to align the model cylinder axis with the free stream direction during the wind tunnel tests.

The tail section commences at the downstream end of the thin shell section and attaches the model to the wind tunnel sting. It is also used to support the instrumentation and pressure line connections between the model and sting.

Details of the center section are shown in Figs. 4 and 6. The nose section, which has been removed for the picture, is attached to the bolts at the right hand end of this section. Installation or removal of a thin shell (with end rings soldered to the shell) is accomplished by removing this nose section and the thrust plate and sliding the shell over the center section and instrumentation. The shell's end rings are then slipped onto the "0" ring seals at each end. The "0" rings are made of neoprene rubber and have a 0.039 inch diameter cross section. The shell end rings and the "0" ring seals are lubricated with Dow Chemical Vacuum Grease. The diametrical interference between the "0" rings and the inside surface of the shell end rings is about 0.010 inches and provides the required sealing of the annular cavity under the shell. An axial force of about 20 pounds is required to slide the shell over the "0" rings, 10 pounds for each one. Consequently, the net axial load in the shell at any time may be of the order of 10 pounds.

Figure 3 gives the over-all dimensions of the flutter model.

A.2 Thin Shells

The making of the thin shell flutter models was the most tedious and crucial task associated with the flutter tests. These shells were thin walled monocoque circular cylinders made by an electroplating process following Babcock (Ref. 25).

In this process, a layer of wax (two parts refined parafin to one part Mobil Cerese 2305 wax by volume) over 1/4 inch thick was cast onto a hollow aluminum mandrel 22 inches long by 15 1/2 inches outside diameter. The waxed mandrel was then machined

to the desired diameter on a large lathe. This finished surface was then sprayed with two coats of conductive silver paint.

The plating was carried out in a Cupric Fluoborate solution of specific gravity 1.15. The 23 inch diameter cylindrical anode used as the material source was made from a 0.10 inch thick copper sheet. This anode was covered by a bag made from dynel cloth to collect the impurities discharged from the anode during the plating. Although the bag collected most of these impurities, in the four hours required to plate a shell, enough would get into the solution to noticeably increase the surface roughness of the shell. In order to minimize this roughness, the solution was continuously filtered during the plating process. To further promote smoothness, each shell was removed from the bath half way through the plating process and carefully sanded. Uniformity in thickness around the circumference was ensured by continuously rotating the mandrel during the plating.

After the plating was completed, the mandrel was again placed on the lathe. The shell was cut to length with a very narrow chisel-like cutting tool, and the excess copper (about three inches at each end) was discarded. These end pieces were not uniform in thickness because of the nonuniformity of the electric field in the plating bath caused by the mandrel and anode end effects. By throwing them away, the maximum variation in shell thickness in the longitudinal direction was kept below $\pm$ 3 percent.

The wax at the lower end of the mandrel was scraped off and a narrow jig was strapped around the mandrel to support the shell during melting of the wax. The mandrel was then clamped into the empty wax-casting tank and melted wax slowly poured over it.

The entire assembly was heated until all the wax was melted. The melted wax was then drained from the tank, the mandrel recovered, and the shell slipped off. The excess wax on the shell was removed with Benzene, and the clean shell was then weighed. This weight and the known length and diameter of the shell were used to evaluate the average thickness using a value of 8.9 gm/cc as the density of the electroplated copper.

Each shell was soldered to two copper end rings as shown in Fig. 5 using Johnson's Flux -'N-Solder (a powdered solder - 50 percent tin and 50 percent lead - in a liquid flux). The outside diameter of the end rings were made 0.003 inches smaller than the inside diameter of the shell to leave room for this solder. The actual soldering process involved the following steps: The outside diametrical surface of the front end ring was given a thin coat of the liquid solder. This ring was then placed front side down on a flat, rigid, aluminum plate. The inside surface near one end of the shell was then given a thin coat of the solder and the shell slipped over the end ring. The inside surface at the other end of the shell and the outside surface of the other end ring were then painted with the solder and slipped together. The step on the outside surface of the back end ring kept it from falling into the shell. This whole assembly still on the flat plate was then placed in an oven and slowly heated to the melting point of the solder (about 360 degrees F). After allowing enough time for equilibrium to be reached at the high temperature, the oven was gradually turned down and the temperature very slowly returned to the room level. In this way, stresses induced in the shell by differential cooling were minimized.

Many people at the GALCIT have contributed to the evaluating of the material properties of the electroplated copper. The Young's Modulus E was determined by pulling and simultaneously measuring the deflection of 1/2 inch wide by 200 inch long specimens

obtained by spirally cutting the cylindrical shell while still on the wax. The value was found to be 16×10^6 psi. The load-deflection curves were linear up to a stress level of 10,000 psi. Values of Poisson's Ratio ν in the range 0.35 to 0.38 were found from the ratios of longitudinal and transverse strains in these tensile specimens as measured with strain gauges. A value of the density of 8.9^+ gm/cc was found by weighing samples of the electroplated copper in air and immersed in distilled water. Further details may be found in Ref. 26.

A.3 Instrumentation and Experimental Measurements

Radial motion of the shell was measured by three inductance type pickups numbered 1 to 3 in Fig. 6. The change in inductance as a function of the distance between the shell and pickup permits static and dynamic measurements of the skin position to be made without mechanical contact. Pickups 1 and 2 are mounted on a drum which is rotated by a small electric motor a full 360 degrees at an angular rate of 24 degrees per second or a surface speed of 3.3 inches per second. Pickup 1 is moved longitudinally between $x/L = 0.15$ and 0.67 by another motor and lead-screw mechanism at 0.5 inches per second. Pickup 2 is located at $x/L = 0.72$. Pickup 3 is fixed to the center body at $x/L = 0.84$. A potentiometer connect by gears to each traversing mechanism supplies a D.C. voltage proportional to the distance or angle traversed. The pickups were manufactured by Electroproducts Incorporated of Chicago, and the carrier system was especially developed for panel flutter testing by the electronics laboratory at the GALCIT. This system uses a 100 kilocycles per second carrier signal.

The static calibration curve for each pickup is shown in Figure A.1. The nominal spacing between each pickup and the shell

skin was 0.130 inches and the corresponding sensitivities were as follows:

Pickup No. 1:	15.2 mv/0.001 inch
Pickup No. 2:	16.7 mv/0.001 inch
Pickup No. 3:	18.2 mv/0.001 inch.

The maximum change in the spacing between the pickups and the shell skin that occurred when the pickups were traversed was approximately 0.010 inches. This resulted in a maximum change in pickup sensitivity of approximately 5 percent. Since this change was only of the order of the accuracy of the experimental measurements, it was ignored in the data reduction.

The root-mean-square values of the signals from the three pickups were measured on a Ballantine Model 320 "True-root-mean-square" voltmeter, and two of these signals were continuously monitored on a Dumont Model 411 dual beam cathode ray oscilloscope. All signals were recorded by an FM system on an Ampex FR-100 tape recorder. Figure A.2 shows a partial view of the instrument arrangement in the tunnel control room.

A twelve-tube boundary layer rake was mounted on the model near the downstream end of the shell as shown in Fig. 2. The tubes were 0.032 inch outside diameter by 0.006 inch wall stainless steel. The ends of the four innermost tubes were flattened to reduce their interference with the flow, as shown in Fig. A.3. The leading edge of the tubes was located 3/4 inches upstream from the downstream end of the shell.

All tunnel testing parameters such as M_∞, p_∞, p_{t_∞} and T_{t_∞} as well as the pressures from the four static ports on the nose section and from the twelve boundary layer rake tubes were measured on NASA equipment. All pressures were measured by calibrated pressure cells. In addition, the four pressures from the static ports on the nose section were monitored on a manometer board using Dibutyl alcohol (specific gravity = 1.03) as the manometer fluid and p_∞ as reference.

The pressure in the rubber tubes of the axial loading mechanism p_r and the pressure in the model cavity were controlled and measured by GALCIT equipment in the tunnel control room. The p_r was measured on a standard absolute pressure gauge, and when the shell was to be unloaded, the rubber tubes were vented to p_∞. The pressure from one of the static ports on the nose section was used as the reference for p_m, the pressure differential across the shell skin. The large values of p_m were measured on a standard pressure differential gauge and the small values were measured with an alcohol (specific gravity = 0.81) U-tube manometer.

A.4 Axial Loading Mechanism

The peculiar axial loading mechanism used in these experiments resulted from the following design considerations:

1. The cylindrical shells were to be loaded in axial compression quickly and remotely during the wind tunnel tests.
2. The circumferential distribution of longitudinal stress in the shell had to be as uniform as possible, and the maximum load had to be about 1000 pounds.
3. The loading mechanism could not interfere with the external air flow.

Experience has shown that one of the most difficult aspects of buckling experiments is that of attaining uniform circumferential distributions of longitudinal stress. See for example, Ref. 25. This difficulty is a direct consequence of the thin-walled nature of cylindrical shells and the need to apply the axial load as uniformly around the circumference as possible is evident. This consideration led to the idea of applying the axial load through a uniform circumferential distribution of pressure. This in turn finally led to the idea of a pressurized, confined rubber tube at each end of the shell. The tubes used in the final design were made of amber rubber and had a 3/16 inch inside diameter and a 1/16 inch thick wall.

A specially instrumented shell was made to check the uniformity of the stress distribution that resulted from this loading technique. The shell used was 0.012 inches thick and was made in the same way as were the shells for flutter testing. SR-4 Wire Strain Gauges (type A-3, resistance 120 ohms, gauge factor 2) were attached with Eastman 9-10 cement to the inner and outer surfaces at 30 degree intervals around the circumference of the shell 2.5 inches from the downstream end. Preliminary loadings of this shell showed that the difference in the strains and hence the stresses in the inside and outside surfaces of the shell were at most of the order of 5 percent of the mean stress level. This indicated that the amount of bending induced by the loading mechanism was very small and could therefore be neglected. Thereafter, the signals from the gauges on the inside and outside surfaces at a particular circumferential position were averaged by connecting the gauges in series, and this average was used as the strain and hence stress level at that circumferential position.

In order to provide a calibration of the axial loading mechanism, this instrumented shell had to be calibrated itself. This was done on a testing machine in the laboratory. The shell was loaded in steps up to 1200 pounds and the strain gauge readings were recorded at each step. A plot of the average of all the strain gauge readings versus axial load was prepared and used as the calibration of this shell.

The shell was then placed on the flutter model and loaded in axial compression by pressurizing the rubber tubes. The resulting distributions of strain and hence stress are plotted in Fig. A.4. The value of the axial load for each setting of the pressure p_r was obtained from the calibration described in the above paragraph and is plotted versus p_r in Fig. A.5. This curve was used as the calibration for the axial load in the shells of the flutter tests.

APPENDIX B

TAPE DATA HANDLING

B.1 Recording

The data recorded on tape consisted of the output of three carrier amplifier channels which provided a measure of the shell motion and the output of either one of the potentiometers connected to the traversing mechanisms on the flutter model which provided a measure of the positions of the inductance pickups.

A seven channel Ampex FR-100 tape recorder was used to record data on one inch magnetic tape at a tape speed of 7.5 inches per second. Tape recorder channels 1, 2 and 3 were used to record the three shell motion data measurements, while the potentiometer data was recorded on channel 4. The data recording amplifiers were FM (frequency modulated) and were capable of recording data in the frequency range from D. C. to 1250 cps. Voice identifications were recorded at the start and end of each record using a direct reproduce amplifier on channel 7. The two remaining channels were unused.

A calibration panel provided a convenient method for recording calibration voltages onto magnetic tape. Consequently, zeros and known voltage levels in the range of $\pm$ 1.4 volts (D. C.)

were recorded frequently during actual data taking in order to assure that the tape recorder amplifier circuits were in proper adjustment and to provide reference levels for subsequent tape data playback.

When the record and reproduce amplifiers of the tape recorder are in average condition, and when care is used in performing calibrations and data monitoring, the recording of data on magnetic tape will result in accuracies of signal voltages to approximately 1 percent of full range, i.e., $\pm$ 0.015 volts, on the assumption that the recorder is operating in a linear manner.

Credit for the development of the foregoing tape recording technique with its corresponding accuracy must be given to Schmidt (Ref. 27).

A schematic view of the data recording circuitry is shown in Fig. B.1.

B.2 Analyzing

The power spectral density distribution for each tape record was obtained with a Technical Products (Models TP 627 plus TP 626) harmonic analyzer. Typical plots are shown in Fig. 13.

Traverse plots were made on a Moseley Model 2D-2A XY plotter. The mean squaring circuit of a Ballantine True RMS Voltmeter was used to obtain the mean square amplitude of the signal that was to be plotted. This mean square of the signal was applied to the Y input of the plotter and the output of channel 4 (traverse potentiometer signal) of the tape recorder was applied to the X input.

The plots of the mean square amplitude of flutter were obtained by feeding the outputs of the tape recorder channels 1 and 2 (signals from pickups 1 or 2 respectively) directly into the Ballantine. On the other hand, the plots of the mean square of the difference between the signals from a moving and a fixed pickup were obtained by subtracting the output of tape recorder channel 3 (signal from pickup 3) from that of channel 1 or 2 with an Epsco D. C. amplifier and feeding this difference into the Ballantine.

Phase angle measurements were made on an AD-YU Model 405 phase meter that works on the zero crossing principle. This phase meter also provides a D. C. output (from a 0.1 second time constant integrating circuit) proportional to the phase angle being measured and this output was used to make phase angle plots.

APPENDIX C

ANALYTIC EXPRESSION OF THE FLUTTER MODES

C.1 Standing Wave Approximation

Consider the standing wave type of deflection shape

$$w(x, \theta, t) = f(x) \sin n\theta \sin \omega t \ . \qquad \text{(C-1)}$$

The function f(x) may be complex, but this will have no bearing on the following arguments. Squaring it, we obtain

$$\begin{aligned} w^2(x, \theta, t) &= f^2(x) \sin^2 n\theta \sin^2 \omega t \\ &= \frac{f^2(x)}{4} (1 - \cos 2n\theta)(1 - \cos 2\omega t) \ . \end{aligned} \qquad \text{(C-2)}$$

Taking the mean, we obtain

$$\overline{w^2}(x, \theta) = \frac{f^2(x)}{4} (1 - \cos 2n\theta) \ . \qquad \text{(C-3)}$$

Hence,we see that the mean square amplitude of the deflection would vary between zero and a maximum 2n times around the circumference if the flutter mode were of the standing wave type represented by Eq. C-1 .

C.2 Circumferentially Travelling Wave Approximation

Consider a deflection shape of the form

$$w(x,\ \theta,\ t) = f(x)\left[A \sin n\theta \sin\omega t + B \cos n\theta \cos\omega t\right]. \quad (C\text{-}4)$$

Squaring it, we obtain

$$\begin{aligned} w^2(x,\ \theta,\ t) &= f^2(x)\Big[A^2\sin^2 n\theta \sin^2\omega t + B^2\cos^2 n\theta \cos^2\omega t \\ &\quad + 2AB \sin n\theta \cos n\theta \sin\omega t \cos\omega t\Big] \\ &= \frac{f^2(x)}{4}\Big[A^2(1 - \cos 2\omega t) \sin^2 n\theta \\ &\quad + B^2(1 + \cos 2\omega t)\cos^2 n\theta + AB \sin 2\omega t \sin 2n\theta\Big]. \end{aligned} \quad (C\text{-}5)$$

Taking the mean, we obtain

$$\begin{aligned} \overline{w^2}\,(x,\ \theta) &= \frac{f^2(x)}{2}\left[A^2 \sin^2 n\theta + B^2 \cos^2 n\theta\right] \\ &= \frac{f^2(x)}{4}\left[(A^2 + B^2) - (A^2 - B^2)\cos 2n\theta\right]. \end{aligned} \quad (C\text{-}6)$$

Now if A and B are approximately equal, we see that $\overline{w^2}\ (x,\ \theta)$ is approximately equal to $(A^2 f^2(x))/2$ which is independent of θ. Hence, the mean square amplitude of motion is constant around the circumference for the type of flutter mode expressed by Eq. C-4.

Now if we take

$$w_1(\theta,\ t) = A \left[\sin n\theta \sin \omega t + \cos n\theta \cos \omega t \right] \qquad \text{(C-7)}$$

and

$$w_3(t) = C \sin \omega t \quad , \qquad \text{(C-8)}$$

and then subtract w_3 from w_1, we obtain

$$\Delta w(\theta,\ t) = w_1(\theta,\ t) - w_3(t) = A \left[\sin n\theta \sin \omega t + \cos n\theta \cos \omega t \right] - C \sin \omega t \qquad \text{(C-9)}$$

Now

$$(\Delta x)^2 = w_1^{\,2} - 2 w_1 w_3 + w_3^{\,2} \qquad \text{(C-10)}$$

and taking the mean, we have

$$\overline{(\Delta w)^2} = \overline{w_1^{\,2}} - \overline{2 w_1 w_3} + \overline{w_3^{\,2}} \quad . \qquad \text{(C-11)}$$

Multiplying w_1 and w_3 together, we obtain

$$\begin{aligned} w_1 w_3 &= AC \left[\sin n\theta \sin^2 \omega t + \cos n\theta \sin \omega t \cos \omega t \right] \\ &= \frac{AC}{2} \left[\sin n\theta \, (1 - \cos 2\omega t) + \cos n\theta \sin 2\omega t \right] . \end{aligned} \tag{C-12}$$

Therefore taking the mean, we obtain

$$\overline{w_1 w_3} = \frac{AC}{2} \sin n\theta \quad . \tag{C-13}$$

We also have that

$$\overline{w_1^2} = \frac{A^2}{2} \quad , \quad \text{and} \quad \overline{w_3^2} = \frac{C^2}{2} \quad . \tag{C-14}$$

Therefore, combining Eqs. C-11, 13 and 14, we obtain

$$\overline{(\Delta w)^2} = \frac{A^2 + C^2}{2} - AC \sin n\theta \quad . \tag{C-15}$$

Therefore, if A and C are approximately equal, the mean square of the difference between w_1 and w_3 is approximately given by

$$\overline{(\Delta w)^2} = \overline{(w_1 - w_3)^2} = A^2(1 - \sin n\theta) \quad . \qquad \text{(C-16)}$$

Hence, the mean square of the difference between w_1 and w_3 varies approximately between zero and a maximum n times as θ goes from 0 to 360 degrees. Therefore, it may be concluded that the type of flutter mode expressed by Eq. C-4 will fit the experimental results, but the one expressed by Eq. C-1 will not.

APPENDIX D

BENCH TESTS

Some still air vibration tests were performed on shells similar to the ones used in the flutter tests. A model D-40 Jensen acoustic driver unit was used to drive the shells into resonance. The acoustic output of the driver was focused onto a 1/4 inch diameter circular area on the shell surface through a conical nozzle positioned about 0.010 inches from the shell skin. The driver was excited by a sinusoidal signal generator and amplifier. The resonance modes were easily determined in the same way as were the flutter modes. The frequency of the excitation signal was measured with a Berkeley EPUT electronic counter.

The results of such a vibration test on a shell of thickness 0.0040 inches are plotted in Fig. 27. The modes with one half a wave along the length of the shell (m = 1) and those with one full wave (m = 2) were relatively easy to obtain, but the modes with three half waves (m = 3) and two full waves (m = 4) were much harder. As a consequence, the measured frequencies for these latter modes were not as accurate as for the former ones. The ratio of the damping to critical damping was estimated from some resonance plots to be about 0.001 for modes with many circumferential waves.

Three shells were buckled under axial compression on the flutter model with zero internal pressure. The thickness of these shells were 0.0041, 0.0040 and 0.0044 inches and the loads at which they buckled were 390, 350 and 400 pounds respectively. These loads are about 40 percent of the classical buckling loads for these shells and are a little higher than most of those shown in Fig. 12 of Ref. 28 for the same radius to thickness ratio (2000). The buckling modes were of the well-known diamond pattern type with the diamonds distributed around the circumference of the shells but concentrated near the downstream end. This concentration of the buckles near the rear end was probably a consequence of the difference in the geometry of the end rings of the shells. This difference in geometry results in a difference in the boundary conditions on the two ends of the shell. These boundary conditions can have a strong influence on the character of the axial buckling. See for example, Ref. 29.

A 0.0040 inch thick shell was buckled by evacuating the annular cavity under the shell. This buckling occurred when the pressure difference across the shell was 0.050 psig as measured with an alcohol manometer. The buckling mode was made up of fifteen waves around the circumference and one half a wave along the length of the shell. The buckles were very shallow and the buckling pressure was repeatable within about 1 percent. The theoretical buckling pressure for this shell was 0.047 psig as calculated from Ref. 30 for the case of radial external pressure loading rather than for hydrostatic loading, since the particular geometry of the flutter model is more closely described by that case.

APPENDIX E

STATIC PRESSURE TEST

E.1 Static Pressure Model and Instrumentation

The 0.020 inch thick shell used for the static pressure model was constructed in the same way as were the thin shell models used in the flutter tests. See for example, Section A.2 of Appendix A.

Fifty-three static pressure ports, 0.0135 inches in diameter, were drilled in the shell with the distribution shown in Fig. E.1. Eleven of the holes lie along the cylindrical generator labeled number 8 and six along each of the other seven generators as shown in the figure.

Figure E.2 shows the arrangement for delivering the pressure to the manometers. A number 70 (0.028 inch diameter) hole was drilled through the wall of a piece of 0.061 O.D. (outside diameter) brass tube. One end was then pinched off and the tube bent as shown was held over one of the holes in the shell with a jig. A short length of 0.009 inch diameter steel wire was inserted through the hole into the brass tube. A small amount of "aluminum Devcon type F2" was then poured over the tube into the shape shown and allowed to set. After the Devcon had hardened, the wire was removed leaving a sealed conduit open only to the pressure port. A 0.050 I.D.

(inside diameter) vinyl spaghetti tube was then forced over the free end of the brass tube and sealed with Glyptol. This process was repeated for all fifty-three ports. The vinyl tubes were carefully fixed to the inside of the shell and were brought together at the back end.

The shell was placed on the flutter model by slipping it over the "0" ring seals from the upstream end of the model (left hand side of Fig. 4) after removing the thrust plate. The vinyl tubes were then placed inside one of the conduits in the tail section. They were attached to the inside of a sealed manifold at the sting end of the conduit. The manifold had fifty-three short pieces of the 0.061 O.D. brass tubing soldered into a piece of 3/16 inch thick brass plate. When the model was installed in the wind tunnel, the pressure leads from a multiple tube manometer bank containing dibutyl alcohol (specific gravity = 1.03) were attached to the free ends of the manifold tubes. The free stream static pressure p_∞ was used as the reference for this manometer bank and was obtained from a static pressure port in the ceiling of the wind tunnel test section a short distance upstream of the model.

A ten-tube boundary layer rake similar to the one shown in Fig. A.3 was mounted on the model near the downstream end of the shell. The tubes were 0.032 inch O.D. by 0.006 inch wall stainless steel. Pressure lines from a second manometer bank containing liquid mercury were attached to the rake tubes.

The pressure difference across the shell p_m was controlled by varying the pressure in the sealed annular region under the shell.

The pressures at the four symmetrically distributed static ports on the downstream end of the nose section were monitored and were made equal by lining up the model axis with the free stream flow.

Maximum deviations of the shell surface from a truly perfect cylinder were estimated to be $\pm$ 0.001 inches.

E.2 Experimental Procedure

The procedure for start-up of the tunnel was the same as for the flutter tests. See Section 2.2. The test conditions are given in Table IV. The test point with correlation number 1 was used solely for aligning the model. After p_{t_∞} was established, about ten minutes were allowed for the manometer readings to come to equilibrium before the data was recorded. Photographs of each manometer board were taken for each data point.

E.3 Results and Discussions

The pressure distribution data are plotted in Figs. E.3, E.4 and E.5. The q_∞ shown in Table IV and used in calculating C_p was obtained from inviscid theory.

The boundary layer data is plotted in Figs. E.6(a), (b) and (c). The static pressure was assumed to be constant through the boundary layer in the radial direction and again inviscid theory was used to calculate the local Mach number from the measured total pressure.

Overlooking local irregularities, the static pressure distribution in the axial direction deteriorates as the Mach number is decreased. At $M_\infty = 3.4$, the static pressure is very uniform over the entire length of the shell, at $M_\infty = 3.0$, it begins to increase slightly near the downstream end of the shell and at $M_\infty = 2.6$ it is increasing over the entire length of the shell. Some of this trend is probably due to the nose shape as outlined in the introduction, but some is probably due to the wind tunnel. Strength considerations dictated that the model be located in the downstream part of the test section and wind tunnel calibrations indicate that flow uniformity there deteriorates somewhat at lower Mach numbers.

The surprising dependence of C_p on q_∞ at $M_\infty = 3.4$ shown in Fig. E.3 is probably due to the so-called "shock wave-boundary layer interaction". See, for example, Ref. 31, pages 340 to 342. Boundary layer theory shows that the displacement thickness of a laminar boundary layer on an insulated flat plate at high Mach numbers is proportional to the Mach number equared and inversely proportional to the square root of the Reynolds number. Qualitatively similar results can be expected here even though the model is not a flat plate and the flow is not laminar. The data of Fig. E.6 substantiate this expectation. Hence as the Mach number increases, the displacement thickness increases rapidly until some critical Mach number range is reached when it is no longer small compared to the model thickness. Then it will begin to have an appreciable effect on the inviscid flow outside the boundary layer. For constant Mach number in this critical range, decreasing q_∞ decreases the Reynolds number which further increases the displacement thickness. Therefore, the effective thickness ratio of the model increases, thus producing an increase in C_p.

In conclusion, it seems that the best flow conditions for the flutter tests would be in the vicinity of $M_{\infty} = 3.0$. The lower Mach numbers should be avoided because of the poor distributions of static pressure accompanying them. On the other hand, at the higher Mach numbers, the static pressure distribution is very favorable, but the boundary layer thickness changes markedly with free stream dynamic pressure. Consequently, the higher Mach numbers should also be avoided.

APPENDIX F

POTENTIAL SOLUTION OF LEONARD AND HEDGEPETH

Leonard and Hedgepeth (Ref. 7) have developed an exact expression for the linearized aerodynamic pressure acting on a cylindrical shell of infinite length, which is exposed externally to an axially-directed air stream and where the shell is deformed by a travelling wave with sinusoidal spatial dependence. It is fairly easy to superimpose solutions for waves travelling in both the upstream and downstream directions to obtain the solution for a standing wave. The results obtained by doing this are given below for the conditions of interest herein.

For a shell deformation given by

$$w = c_m e^{i\omega t} \sin n\theta \sin \alpha_m x \quad , \tag{F.1}$$

the resulting aerodynamic pressure may be put in the form

$$p = c_m e^{i\omega t} \sin n\theta \left[p_{sm} \sin \alpha_m x + p_{cm} \cos \alpha_m x \right] \quad , \tag{F.2}$$

where p_{sm} and p_{cm} are as follows:

(i) For $M_1 = M_\infty (1 - k) > 1$, $k = \dfrac{\omega}{\alpha_m U_\infty} > 0$

$$p_{sm} = \frac{\gamma \alpha_m p_\infty}{2} \left[\frac{M_1^2}{\sqrt{M_1^2 - 1}} H_1(z_1; n) + \frac{M_2^2}{\sqrt{M_2^2 - 1}} H_2(z_2; n) \right], \quad \text{(F. 3a)}$$

$$p_{cm} = \frac{i\gamma \alpha_m p_\infty}{2} \left[\frac{M_1^2}{\sqrt{M_1^2 - 1}} H_1(z_1; n) - \frac{M_2^2}{\sqrt{M_2^2 - 1}} H_2(z_2; n) \right]; \quad \text{(F. 3b)}$$

(ii) For $|M_1| < 1$,

$$p_{sm} = \frac{\gamma \alpha_m p_\infty}{2} \left[\frac{M_1^2}{\sqrt{1 - M_1^2}} K(z_3; n) + \frac{M_2^2}{\sqrt{M_2^2 - 1}} H_2(z_2; n) \right], \quad \text{(F. 4a)}$$

$$p_{cm} = \frac{i\gamma \alpha_m p_\infty}{2} \left[\frac{M_1^2}{\sqrt{1 - M_1^2}} K(z_3; n) - \frac{M_2^2}{\sqrt{M_2^2 - 1}} H_2(z_2; n) \right], \quad \text{(F. 4b)}$$

where

$$M_2 = M_\infty (1 + k) > 1 \quad ,$$

$$H_1(z;\, n) = \frac{H_n^{(1)}(z)}{\frac{dH_n^{(1)}}{dz}(z)} \quad ,$$

$$H_2(z;n) = \frac{H_n^{(2)}(z)}{\frac{dH_n^{(2)}}{dz}(z)} \quad ,$$

$$K(z;\, n) = \frac{K_n(z)}{\frac{dK_n}{dz}(z)} \quad ,$$

$$z_1 = \alpha_m \sqrt{M_1^2 - 1}\, R \quad , \quad |M_1| > 1 \quad ,$$

$$z_2 = \alpha_m \sqrt{M_2^2 - 1}\, R \quad , \quad |M_2| > 1 \quad ,$$

$$z_3 = \alpha_m \sqrt{1 - M_1^2}\, R \quad , \quad |M_1| < 1 \quad ,$$

and $H_n^{(1)}(z)$ and $H_n^{(2)}(z)$ are the Hankel functions (Bessel functions of the third kind) and $K_n(z)$ is the modified Hankel function (modified Bessel function of the third kind).

APPENDIX G

THE BOUNDARY LAYER PERTURBATION PROBLEM ASSOCIATED WITH THE SUPERSONIC FLUTTER OF CYLINDRICAL SHELLS

G.1 Nomenclature

A	$(V''/V')_c$
a	speed of sound in gas
B	$\left[2/3\ (V'''/V') - 1/2\ (V''/V')^2 \right]_c$
C	arbitrary constant in power series solution of P_+ near critical point of Eq. (G.22)
C_p	specific heat of gas at constant pressure
F, G, H	z dependent amplitudes of x, z, y components of perturbation velocities respectively; cf. Eqs. (G.8) to (G.10).
i	$\sqrt{-1}$
k	reduced frequency of wall oscillation, $\omega^*/\alpha U_\infty^*$
M	Mach number
P	z dependent amplitude of pressure perturbations; cf. Eq. (G.12).

P_s, P_c	amplitude of $\sin \alpha x$ and $\cos \alpha x$ components of perturbation pressure on wall respectively; cf. Eq. (G.46).
p	pressure perturbation
$\overline{p}$	mean component of pressure in unperturbed gas flow
Q	P'/P
R	universal gas constant
R_e	Reynold's number
S	z dependent amplitude of density perturbations; cf. Eq. (G.11)
T	temperature perturbation
$\overline{T}$	mean component of temperature in unperturbed gas flow
t	time
U	mean component of velocity in unperturbed gas flow
u_x, u_y, u_z	x, y, z components of velocity perturbations respectively
V	$M_\infty (U \pm k)/\sqrt{\overline{T}}$
w	wall deflection
x	coordinate in plane of wall and parallel to free stream direction
y	coordinate in plane of wall and normal to free stream direction
z	coordinate normal to wall

α	wave number of perturbations in x direction
β	wave number of perturbations in y direction
γ	ratio of specific heats of gas
δ	boundary layer thickness
η	z/δ
η_c	value of η for which $U = k$
Θ	z dependent amplitude of temperature perturbations; cf. Eq. (G.13).
κ	$\alpha\delta$, boundary layer thickness parameter
π	3.14159265
ρ	density perturbation
$\overline{\rho}$	mean component of density in unperturbed gas flow
σ	β/α, three dimensionality parameter
φ_s, φ_c	phase angles of coefficients of $\sin \alpha x$ and $\cos \alpha x$ components of perturbation pressure on wall respectively; cf. Eq. (G.46).
ω	frequency of wall oscillation

Subscripts

i	imaginary part
r	real part
∞	free stream value
+, -	parts of perturbations which have form of travelling waves in + and - x directions, respectively.

Superscripts

*	denotes dimensional quantities (Note: the variables α, β, x, y, z, δ, w, C_p, R are also dimensional)

Miscellaneous Functionals

$\mathcal{R}e$ ( )	real part of ( )
$\mathcal{I}m$ ( )	imaginary part of ( )
$\lvert ( ) \rvert$	modulus of ( )
Arg ( )	argument of ( )
$[\ ]_c$	$[\ ]$ evaluated at critical point ($\eta = \eta_c$)
ℓn ( )	natural logarithm of ( )

G. 2 Introduction

The importance of including the effect of the viscous boundary layer in analyzing certain types of panel flutter has been fairly well established. The preliminary work of Miles (Ref. 32), McClure (Ref. 33) and Anderson and Fung (Ref. 4) which pertains to this problem is summarized by Fung in Ref. 2. Miles showed that a parallel shear flow may reduce the degree of instability of an axisymmetric travelling wave on an infinitely long cylindrical shell in an external supersonic flow by an order of magnitude. McClure showed that the boundary layer on a flat panel in the low supersonic Mach number range is very stabilizing to two-dimensional flutter. This seems to be a transonic phenomenon in that the effect of the boundary layer vanished as the Mach number approached $\sqrt{2}$. Anderson and Fung's work with an idealized step-boundary layer model on a cylindrical shell showed a significant three-dimensional effect. An increase in the number of circumferential waves in the flutter mode was accompanied by significant changes in the amplitude and phase of the aerodynamic pressure on the shell wall.

In more recent work, McClure (Ref. 34) has developed a "pseudo-laminar" theory for travelling-wave disturbances in the fully turbulent boundary layer on the basis of an analogy with laminar viscous flow. The assumed point of view which has been basic to the development of the classical aerodynamic pressure operators for use in flutter calculations is that regular perturbations are induced in the flow by a prescribed wall motion. He considers three postulated interactions between 1) these regular disturbances and 2) the mean steady flow (mean plus turbulent components). The alternative postulates are designated: the "linear interaction" in which 1) and 2) are completely independent; the "quasi-linear interaction" in which 1) depend only slightly on 2); and the "non-linear interaction" in which 1) and 2) are highly dependent on each other. He shows that the

"linear interaction" model is an adequate representation of the phenomenon under the restrictions that i) the wall motion has a negligible random component, and ii) the disturbance has small enough amplitude and phase velocity (compared to the free stream velocity).

The experimental results (Section 2.3) seem to indicate that these restrictions are indeed satisfied for the cylindrical shell flutter. Power spectral analysis of the shell wall motions during flutter showed no measurable power at any frequencies except the flutter frequency (or frequencies in the cases when more than one flutter mode was present). In addition, there was no measurable change in the boundary layer profile after the onset of flutter.

On the basis of these justifications, the "linear interaction, pseudo-laminar" model is assumed from the outset in the present work. Furthermore, only the inviscid solution to the resulting perturbation equations is considered. In analogy to the laminar case, this inviscid solution corresponds to the so-called zeroth order solution of an asymptotic solution of the complete linearized perturbation equations based on an expansion in powers of $1/\alpha R_e$. Hence, this solution can be expected to be a reasonable approximation as long as αR_e is very large. For the intended applications, this will indeed be the case.

For most applications, the boundary layer will be thin compared to the radius of the shell. Hence, the cylindrical surface may be considered esentially flat and the boundary layer perturbation problem may be solved for a flat wall. This will simplify the computations considerably.

G. 3 Formulation of Boundary Layer Perturbation Problem

G. 3.1 Differential Equations for Infinitesimal Disturbances

The geometry to be considered is that of a supersonic stream flowing approximately parallel to the flexible surface wall defined by the plane z = 0. Some kind of a turbulent boundary layer exists near the wall. The flow that exists when the wall is perfectly flat and stationary is called the undisturbed flow, and the quantities which define this flow such as velocity and temperature are composed of two parts, the mean or time-independent components and the turbulent or randomly-fluctuating components. The mean components depend on the space coordinates x (the stream wise direction) and z but not on y.

The mathematical problem is formulated by assuming that the undisturbed flow is exactly parallel to the plane z = 0 and extends in the x direction from $-\infty$ to $+\infty$. As a result, the mean components of the undisturbed flow quantities depend only on z. The effective Prandtl number for the flow is assumed to be unity and the wall is taken as insulated so that the mean component of temperature $\overline{T}^*(z)$ is related to the mean component of velocity $U^*(z)$ by

$$C_p \overline{T}^* + \frac{1}{2} U^{*2} = \text{constant} . \qquad (G.1)$$

With the usual assumption that the mean component of pressure is constant across the boundary layer, the mean component of density $\overline{\rho}^*(z)$ is proportional to the inverse of the mean component of temperature from the perfect gas law.

The wall z = 0 is assumed to be oscillating in the z direction with infinitesimal amplitude in a standing wave pattern so that its deflection is given by $w(x, y, t) = e^{-i\omega^* t} \sin \alpha x \sin \beta y$. The common complex notation is employed for the time dependence, and the deflection amplitude is taken to be unity for convenience. The oscillating wall induces regular perturbations in velocity (u_x^*, u_y^*, u_z^*), pressure p^*, density ρ^* and temperature T^* in the gas flow adjacent to it. It is assumed that these perturbations do not affect the undisturbed flow quantities so that the total flow quantities such as velocity and temperature are just the sum of corresponding undisturbed flow quantities and these perturbation quantities.

Substitution of the total flow quantities into the conservation laws of mass, momentum and energy, subtracting off the boundary layer equations which the undisturbed flow quantities were assumed to satisfy, dropping all nonlinear terms in turbulent and perturbation quantities and neglecting viscous and heat conduction terms yields the following set of perturbation equations:

Continuity:

$$\frac{1}{U_\infty^*} \frac{\partial \rho}{\partial t} + \bar{\rho} \left[\frac{\partial u_x}{\partial x} + \frac{\partial u_y}{\partial y} + \frac{\partial u_z}{\partial z} \right] + \frac{d\bar{\rho}}{dz} u_z + U \frac{\partial \rho}{\partial x} = 0 \qquad \text{(G. 2)}$$

Momentum:

$$\bar{\rho} \left[\frac{1}{U_\infty^*} \frac{\partial u_x}{\partial t} + U \frac{\partial u_x}{\partial x} + \frac{dU}{dz} u_z \right] = -\frac{1}{\gamma M_\infty^2} \frac{\partial p}{\partial x} \qquad \text{(G. 3)}$$

$$\bar{\rho} \left[\frac{1}{U_\infty^*} \frac{\partial u_y}{\partial t} + U \frac{\partial u_y}{\partial x} \right] = -\frac{1}{\gamma M_\infty^2} \frac{\partial p}{\partial y} \qquad \text{(G. 4)}$$

$$\bar{\rho}\left[\frac{1}{U_\infty^*}\frac{\partial u_z}{\partial t} + U\frac{\partial u_z}{\partial x}\right] = -\frac{1}{\gamma M_\infty^2}\frac{\partial p}{\partial z} \qquad (G.5)$$

Energy:

$$\bar{\rho}\left[\frac{1}{U_\infty^*}\frac{\partial T}{\partial t} + U\frac{\partial T}{\partial x} + \frac{d\bar{T}}{dz}u_z\right] = -(\gamma-1)\left[\frac{\partial u_x}{\partial x} + \frac{\partial u_y}{\partial y} + \frac{\partial u_z}{\partial z}\right] \qquad (G.6)$$

State:

$$p = \frac{\rho}{\bar{\rho}} + \frac{T}{\bar{T}} \quad , \quad \bar{\rho}\,\bar{T} = 1 \qquad (G.7)$$

where the following nondimensionalization has been included:

$$U(z) = \frac{U^*(z)}{U_\infty^*} \quad , \quad \underset{y}{\overset{u_x}{z}}(x, y, z, t) = \frac{\underset{y}{\overset{u_x^*}{z}}(x, y, z, t)}{U_\infty^*}$$

$$M_\infty = \frac{U_\infty^*}{a_\infty^*} = \frac{U_\infty^*}{\sqrt{\gamma R T_\infty^*}}$$

$$p(x, y, z, t) = \frac{p^*(x, y, z, t)}{p_\infty^*} \quad , \quad \bar{p} = \frac{\bar{p}^*}{p_\infty^*} = 1$$

$$\rho(x, y, z, t) = \frac{\rho^*(x, y, z, t)}{\rho_\infty^*} \quad , \quad \bar{\rho}(z) = \frac{\bar{\rho}^*(z)}{\rho_\infty^*}$$

$$T(x,\ y,\ z,\ t) = \frac{T^*(x,\ y,\ z,\ t)}{T_\infty^*} \quad , \quad \overline{T}(z) = \frac{\overline{T}^*(z)}{T_\infty^*}$$

$$k = \frac{\omega^*}{\alpha U_\infty^*}$$

Now as a result of the simplifying assumptions, these equations have coefficients which depend only on z. Hence the dependence of the perturbation quantities on x, y and t may be assumed to be exponential, and in particular periodic. It may be seen that the following assumed form of the solutions will satisfy the equations and the boundary conditions.

$$u_x(x, y, z, t) = \sin\beta y \left[F_+(z) e^{i(\alpha x - \omega^* t)} + F_-(z) e^{-i(\alpha x + \omega^* t)} \right] \qquad (G.8)$$

$$u_y(x, y, z, t) = i \cos\beta y \left[H_+(z) e^{i(\alpha x - \omega^* t)} + H_-(z) e^{-i(\alpha x + \omega^* t)} \right] \qquad (G.9)$$

$$u_z(x, y, z, t) = i \sin\beta y \left[G_+(z) e^{i(\alpha x - \omega^* t)} + G_-(z) e^{-i(\alpha x + \omega^* t)} \right] \qquad (G.10)$$

$$\rho(x, y, z, t) = \sin\beta y \left[S_+(z) e^{i(\alpha x - \omega^* t)} + S_-(z) e^{-i(\alpha x + \omega^* t)} \right] \qquad (G.11)$$

$$p(x, y, z, t) = \sin\beta y \left[P_+(z) e^{i(\alpha x - \omega^* t)} + P_-(z) e^{-i(\alpha x + \omega^* t)} \right] \qquad (G.12)$$

$$T(x, y, z, t) = \sin\beta y \left[\Theta_+(z) e^{i(\alpha x - \omega^* t)} + \Theta_-(z) e^{-i(\alpha x + \omega^* t)} \right] \qquad (G.13)$$

The plus and minus sign subscripts denote the portions of the solution which have the form of traveling-waves in the plus and minus x directions respectively. Substituting these quantities into Eqs. (G. 2) to (G. 7) yields

Continuity:

$$\left[S_+(U-k)+\bar{\rho}\left(F_+-\frac{\beta}{\alpha}H_+ +\frac{1}{\alpha}\frac{dG_+}{dz}\right)+\frac{1}{\alpha}\frac{d\bar{\rho}}{dz}G_+\right]e^{i\alpha x} \quad +$$

$$\left[S_-(U+k)+\bar{\rho}\left(F_- +\frac{\beta}{\alpha}H_- -\frac{1}{\alpha}\frac{dG_-}{dz}\right)-\frac{1}{\alpha}\frac{d\bar{\rho}}{dz}G_-\right]e^{-i\alpha x}=0 \qquad \text{(G.14)}$$

Momentum:

$$\left[F_+(U-k)+\frac{1}{\alpha}\frac{dU}{dz}G_+ +\frac{P_+}{\gamma M_\infty^2\bar{\rho}}\right]e^{i\alpha x} \quad +$$

$$\left[F_-(U+k)-\frac{1}{\alpha}\frac{dU}{dz}G_- +\frac{P_-}{\gamma M_\infty^2\bar{\rho}}\right]e^{-i\alpha x}=0 \qquad \text{(G.15)}$$

$$\left[H_+(U-k)-\frac{\beta P_+}{\alpha\gamma M_\infty^2\bar{\rho}}\right]e^{i\alpha x} \quad +$$

$$\left[H_-(U+k)+\frac{\beta P_-}{\alpha\gamma M_\infty^2\bar{\rho}}\right]e^{-i\alpha x}=0 \qquad \text{(G.16)}$$

$$\left[G_+(U-k)-\frac{1}{\alpha\gamma M_\infty^2\bar{\rho}}\frac{dP_+}{dz}\right]e^{i\alpha x} \quad +$$

$$\left[G_-(U+k)+\frac{1}{\alpha\gamma M_\infty^2\bar{\rho}}\frac{dP_-}{dz}\right]e^{-i\alpha x}=0 \qquad \text{(G.17)}$$

Energy:

$$\left[\Theta_+(U-k) + \frac{1}{\alpha}\frac{d\bar{T}}{dz}G_+ + \frac{\gamma-1}{\bar{\rho}}\left(F_+ - \frac{\beta}{\alpha}H_+ + \frac{1}{\alpha}\frac{dG_+}{dz}\right)\right]e^{i\alpha x} +$$

$$\left[\Theta_-(U+k) - \frac{1}{\alpha}\frac{d\bar{T}}{dz}G_- + \frac{\gamma-1}{\bar{\rho}}\left(F_- + \frac{\beta}{\alpha}H_- - \frac{1}{\alpha}\frac{dG_-}{dz}\right)\right]e^{-i\alpha x} = 0 \qquad \text{(G.18)}$$

State:

$$\left[P_+ - \frac{S_+}{\bar{\rho}} - \frac{\Theta_+}{\bar{T}}\right]e^{i\alpha x} + \left[P_- - \frac{S_-}{\bar{\rho}} - \frac{\Theta_-}{\bar{T}}\right]e^{-i\alpha x} = 0 \,. \qquad \text{(G.19)}$$

Since the $e^{i\alpha x}$ and $e^{-i\alpha x}$ are independent, the coefficients of these terms must all vanish individually. Hence there is one set of six total differential equations for the six dependent variables F_+, G_+, H_+ S_+, P_+ and Θ_+ and another set of the other six F_-, G_-, H_-, S_-, P_- and Θ_-. Each set of six may be combined to form one second order equation in only one variable, and it will be convenient here to let that variable be the pressure P_+ or P_-. When this is done, the resulting equation is

$$\frac{d^2P_+}{dz^2} + \left[\frac{1}{\bar{T}}\frac{d\bar{T}}{dz} - \frac{2}{U-k}\frac{dU}{dz}\right]\frac{dP_+}{dz}$$

$$+\left[\alpha^2\left(\frac{M_\infty{}^2(U-k)^2}{\bar{T}} - 1\right) - \beta^2\right]P_+ = 0 \,. \qquad \text{(G.20)}$$

The corresponding equation for P_- may be obtained from Eq. (G.20) by simply replacing P_+ by P_-, α by $-\alpha$ and k by -k. Introducing the nondimensional independent variable $\eta = z/\delta$ where δ is the boundary layer thickness and the function

$$V_+(\eta) = \frac{M_\infty \left[U(\eta) - k \right]}{\sqrt{\overline{T}(\eta)}} \quad , \tag{G. 21}$$

Eq. (G. 20) becomes

$$P_+'' - \frac{2V_+'}{V_+} P_+' + \kappa^2 \left[V_+^2 - (1 + \sigma^2) \right] P_+ = 0 \tag{G. 22}$$

where $\kappa = \alpha\delta$, $\sigma = \beta/\alpha$ and primes denote differentiation with respect to η. Similarly the equation for P_- is

$$P_-'' - \frac{2V_-'}{V_-} P_-' + \kappa^2 \left[V_-^2 - (1 - \sigma^2) \right] P_- = 0 \tag{G. 23}$$

where

$$V_-(\eta) = \frac{M_\infty \left[U(\eta) + k \right]}{\sqrt{\overline{T}(\eta)}} \quad . \tag{G. 24}$$

The form of $\overline{T}(\eta)$ may be obtained from Eq. (G.1) and is

$$\overline{T}(\eta) = 1 + \frac{\gamma - 1}{2} M_\infty^2 \left[1 - U^2(\eta) \right] \quad . \tag{G. 25}$$

G. 3. 2 Boundary Conditions

Since the viscosity and heat conduction have been neglected in the perturbation equations, the only boundary condition that may be satisfied at the wall is that the normal perturbation velocity be equal to the velocity of the wall. For the given wall deflection, this condition takes the form

$$u_z(x, y, 0, t) = \frac{1}{U_\infty^*} \frac{\partial w}{\partial t} = \frac{-i\omega^*}{U_\infty^*} e^{-i\omega^* t} \sin \alpha x \sin \beta y \,. \qquad \text{(G. 26)}$$

Now from Eq. (G.10),

$$u_z(x, y, 0, t) = i \sin\beta y \left[G_+(0) e^{i(\alpha x - \omega^* t)} + G_-(0) e^{-i(\alpha x + \omega^* t)} \right]$$

$$= i \sin\beta y \, e^{-i\omega^* t} \left[(G_+(0) + G_-(0)) \cos\alpha x + i(G_+(0) - G_-(0)) \sin\alpha x \right] . \qquad \text{(G. 27)}$$

Hence combining Eqs. (G. 26) and (G. 27) yields

$$G_+(0) = - G_-(0) = \frac{i\alpha k}{2} \,. \qquad \text{(G. 28)}$$

This may be easily converted into boundary conditions on P_+ and P_- by using Eqs. (G.17). In nondimensional form, these are

$$P_+'(0) = \frac{-i\alpha\kappa k^2\gamma M_\infty^2}{2 + (\gamma - 1)M_\infty^2} \qquad \text{(G. 29a)}$$

and

$$P_-'(0) = \frac{i\alpha\kappa k^2\gamma M_\infty^2}{2 + (\gamma - 1)M_\infty^2} \; . \qquad \text{(G. 29b)}$$

The outer boundary conditions may be obtained by considering Eqs. (G. 22) and (G. 23) as η becomes large. As $\eta \to \infty$, $U(\eta) \to 1$, $\bar{T}(\eta) \to 1$ so that $V_+' \to 0$ and $V_+ \to M_\infty(1 - k)$. Hence Eq. (G. 22) becomes

$$P_+'' + \kappa^2\left[M_\infty^2(1 - k)^2 - (1 + \sigma^2)\right] P_+ = 0 \; . \qquad \text{(G. 30)}$$

Hence the behavior of P_+ for large η is

$$P_+ \sim \exp\left[\pm i\kappa\sqrt{M_\infty^2(1 - k)^2 - (1 + \sigma^2)}\;\eta\right] \qquad \text{(G. 31a)}$$

or

$$P_+ \sim \exp\left[\pm \kappa\sqrt{1 + \sigma^2 - M_\infty^2(1 - k)^2}\;\eta\right] \qquad \text{(G. 31b)}$$

If $M_\infty{}^2(1 - k)^2$ is greater than or less than $(1 + \sigma^2)$ respectively. In the first case, the Sommerfeld radiation condition is used to determine which sign is appropriate. This condition requires that the perturbations be functions of $(x - c\eta)$ as $\eta \to \infty$ for supersonic outer flow. Since the P_+ is multiplied by $e^{i\alpha x}$ in the pressure perturbation expression, the minus sign in expression (G. 31a) must therefore be chosen. In the second case, the minus sign in expression (G. 31b) is chosen in order that the perturbation not grow unbounded as $\eta \to \infty$. Hence, the outer boundary conditions for P_+ become

$$\frac{P_+'}{P_+} = -i\kappa\sqrt{M_\infty{}^2(1 - k)^2 - (1 + \sigma^2)} \qquad \text{(G. 32a)}$$

or

$$\frac{P_+'}{P_+} = -\kappa\sqrt{1 + \sigma^2 - M_\infty{}^2(1 - k)^2} \qquad \text{(G. 32b)}$$

as $\eta \to \infty$ for these two cases.

A similar analysis for P_- leads to the outer boundary conditions

$$\frac{P_-'}{P_-} = i\kappa\sqrt{M_\infty{}^2(1 + k)^2 - (1 + \sigma^2)} \qquad \text{(G. 33a)}$$

or

$$\frac{P_-'}{P_-} = -\kappa\sqrt{1 + \sigma^2 - M_\infty{}^2(1 + k)^2} \qquad \text{(G. 33b)}$$

if $M_\infty{}^2(1 + k)^2$ is greater than or less than $(1 + \sigma^2)$ respectively.

G.4 Solution of Pressure Perturbation Equations

It has been customary in the past to solve the inviscid equation for the stability of the laminar boundary layer in the form of a convergent series in powers of α^2 (or κ^2). However, this approach proves unsatisfactory for high Mach numbers because of the resulting slow convergence. It would also be unsatisfactory for the case in which σ^2 is large. Hence, in the present problem a numerical solution to Eqs. (G. 22) and (G. 23) is required. The approach outlined by Reshotko (Ref. 35) for solving the laminar boundary layer stability problem will be followed here.

The mean velocity profile for the turbulent boundary layer is taken to be the well-known one seventh power law between $\eta = 0.1$ and 0.9. For $\eta > 0.9$, the profile is taken to be exponential such that U and U' are continuous at $\eta = 0.9$ and $U \to 1$ as $\eta \to \infty$. For $\eta < 0.1$, a power series of the form $U = a\eta + b\eta^7 + c\eta^8 + d\eta^9$ is assumed and the parameters a, b, c and d are chosen so as to make U, U', U'' and U''' continuous at $\eta = 0.1$. As shown in Figure G.1 this assumed profile provides a good fit for the experimental data of Coles (Ref. 36).

G.4.1 Numerical Solution of Equation for P_+

By the standard transformation

$$Q_+ = \frac{P_+'}{P_+} \quad , \tag{G. 34}$$

Eq. (G. 22) can be converted into the following first order nonlinear equation of the Riccati type

$$Q_+' = \frac{2V_+'}{V_+} Q_+ - Q_+^2 + \kappa^2\left[1 + \sigma^2 - V_+^2\right] \quad . \qquad \text{(G. 35)}$$

Eq. (G. 35) is a complex equation and can be broken up into real and imaginary parts

$$Q_{+_r}' = \frac{2V_+'}{V_+} Q_{+_r} - (Q_{+_r}^2 - Q_{+_i}^2) + \kappa^2\left[1 + \sigma^2 - V_+^2\right] \qquad \text{(G. 36a)}$$

$$Q_{+_i}' = \frac{2V_+'}{V_+} Q_{+_i} - 2Q_{+_r} Q_{+_i} \quad . \qquad \text{(G. 36b)}$$

Eqs. (G. 32) lead to the outer boundary conditions

$$Q_{+_r} = -\kappa\sqrt{1 + \sigma^2 - M_\infty^2(1 - k)^2} \quad , \quad Q_{+_i} = 0 \qquad \text{(G. 37a)}$$

or

$$Q_{+_r} = 0 \quad , \quad Q_{+_i} = -\kappa\sqrt{M_\infty^2(1 - k)^2 - (1 + \sigma^2)} \qquad \text{(G. 37b)}$$

as $\eta \to \infty$ depending on whether $1 + \sigma^2$ is greater than or less than $M_\infty^2(1 - k)^2$ respectively.

For a given wall oscillation and boundary layer geometry, κ , σ , M_∞ and k are known. Hence Q_+ for large η is known and Eqs. (G. 36) can be integrated numerically in through the boundary layer (i. e. $\eta \to 0$). However, for most applications $k < 1$, and hence V_+ goes to zero somewhere in the boundary layer. The point where this occurs is defined by η_c and is the so-called critical layer from hydrodynamic stability problems. Eq. (G. 22) has a regular singularity at $\eta = \eta_c$ as a result of the neglecting of viscosity and heat conduction for the perturbation quantities. It is clear that the inviscid solution cannot fully describe the physical phenomenon in the vicinity of η_c. However, in the laminar problem (Ref. 35), as long as $\propto R_e(1 - k) \gg 1$ the effects of viscosity and heat conductivity die out rapidly with distance on either side of the critical layer and have very little effect on the solution a finite distance away from this layer. The same results should hold true in the present problem.

The solution in the neighborhood of the singular point η_c is obtained by series expansion (method of Frobenius), the details of which are given in Appendix H. The resulting behavior of Q_+ about the critical point is as follows:

$$Q_{+_r} = -\kappa^2(1+\sigma^2)(\eta - \eta_c)\left\{1 - C_r(\eta - \eta_c) + \left[B + \kappa^2(1+\sigma^2) - A(A + C_r) + \frac{\left[V_+'^2\right]}{1+\sigma^2}c\right](\eta - \eta_c)^2 + (\eta - \eta_c)\,A\,\ell n\left|\eta - \eta_c\right|\cdot \left[1 + A(\eta - \eta_c) + \left(\kappa^2(1+\sigma^2) + \frac{1}{2}(B + A^2)\right)(\eta - \eta_c)^2\right]\right\} , \quad \text{(G. 38)}$$

for $(\eta - \eta_c) > 0$

$$\frac{Q_{+_i}}{\kappa^2(1+\sigma^2)} = C_i(\eta-\eta_c)^2\left\{1 + A(\eta-\eta_c) + \left[\kappa^2(1+\sigma^2) + \frac{1}{2}(B + A^2)\right](\eta-\eta_c)^2\right\}, \quad \text{(G. 39a)}$$

for $(\eta - \eta_c) < 0$

$$Q_{+_i} = \kappa^2(1+\sigma^2)(A\pi + C_i)(\eta-\eta_c)^2\left\{1 + A(\eta-\eta_c) + \left[\kappa^2(1+\sigma^2) + \frac{1}{2}(B + A^2)\right](\eta-\eta_c)^2\right\}, \quad \text{(G. 39b)}$$

where

$$A = \left[\frac{V_+''}{V_+'}\right]_c, \quad \text{(G. 40a)}$$

$$B = \left[\frac{2}{3}\frac{V_+'''}{V_+'} - \frac{1}{2}\left(\frac{V_+''}{V_+'}\right)^2\right]_c, \quad \text{(G. 40b)}$$

$C = C_r + iC_i$ = arbitrary constant which may be complex.

The actual numerical integration is slightly different for the two different sets of boundary conditions (G. 37a) and (G. 37b), and may be conveniently broken into two cases as follows:

Case 1: $1 + \sigma^2 \geq M_\infty^2 (1 - k)^2$

In this case, $Q_{+_i} \equiv 0$ for $\eta > \eta_c$ so that $C_i \equiv 0$.
The nature of the solution for Q_+ is depicted in the following sketch.

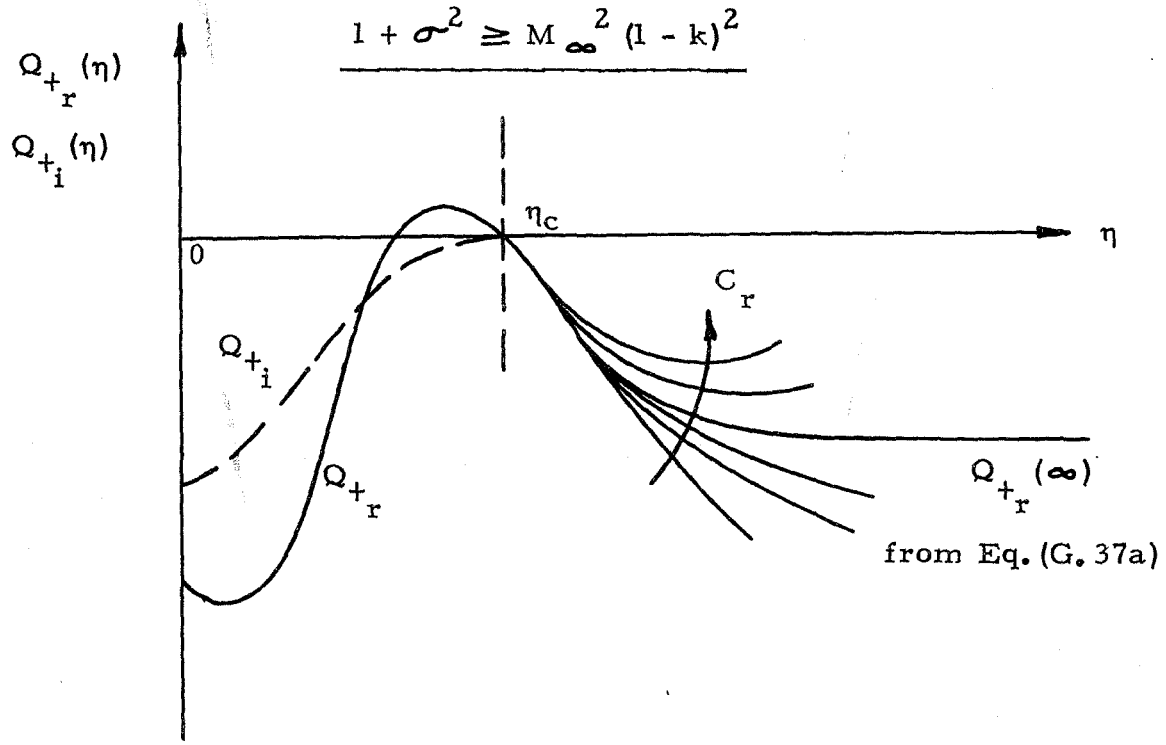

From Eq. (G. 38), it can be seen that Q_{+_r} has a slope of $-\kappa^2(1 + \sigma^2)$ at the critical point, but the curvature is logarithmically singular. Each value of C_r defines a Q_{+_r} curve for $\eta > \eta_c$, but only one value will result in a curve that becomes asymptotic to $Q_{+_r}(\infty)$, the required outer boundary condition. Once this constant is determined, the integration can proceed inward from the critical layer to the wall.

The actual integration for this case then is as follows:

Integration from Infinity in to Critical Layer

(1) Given κ , σ , k and M_∞ , calculate η_c from mean profile, calculate A and B from Eqs. (G.40a and G.40b) and evaluate the outer boundary condition from Eq. (G. 37a).

(2) Integrate Eq. (G. 36a) from infinity ($\eta \approx 2.5$) into the vicinity of η_c. Obtain a first estimate of C_r by inverting Eq. (G. 38).

(3) Using this value of C_r in Eq. (G. 38), evaluate Q_{+_r} for a small positive value of $(\eta - \eta_c)$.

(4) Continue calculating Q_{+_r} by integrating Eq. (G. 36a) out to infinity. Compare the result with the value from step (1).

(5) Repeat steps (3) and (4) adjusting C_r until the outer boundary condition is satisfied.

Integration from Critical Layer into Wall

(6) Using the value of C_r from step (5), evaluate Q_{+_r} and Q_{+_i} for some small negative value of $(\eta - \eta_c)$.

(7) Continue calculation of Q_{+_r} and Q_{+_i} by simultaneous integration of Eqs. (G. 36) in to $\eta = 0$.

Case 2: $M_\infty{}^2(1 - k)^2 > 1 + \sigma^2$

In this case, $Q_{+_i} \neq 0$ for $\eta > \eta_c$, so that $C_i \neq 0$. The nature of the solution for Q_+ is depicted in the following sketch.

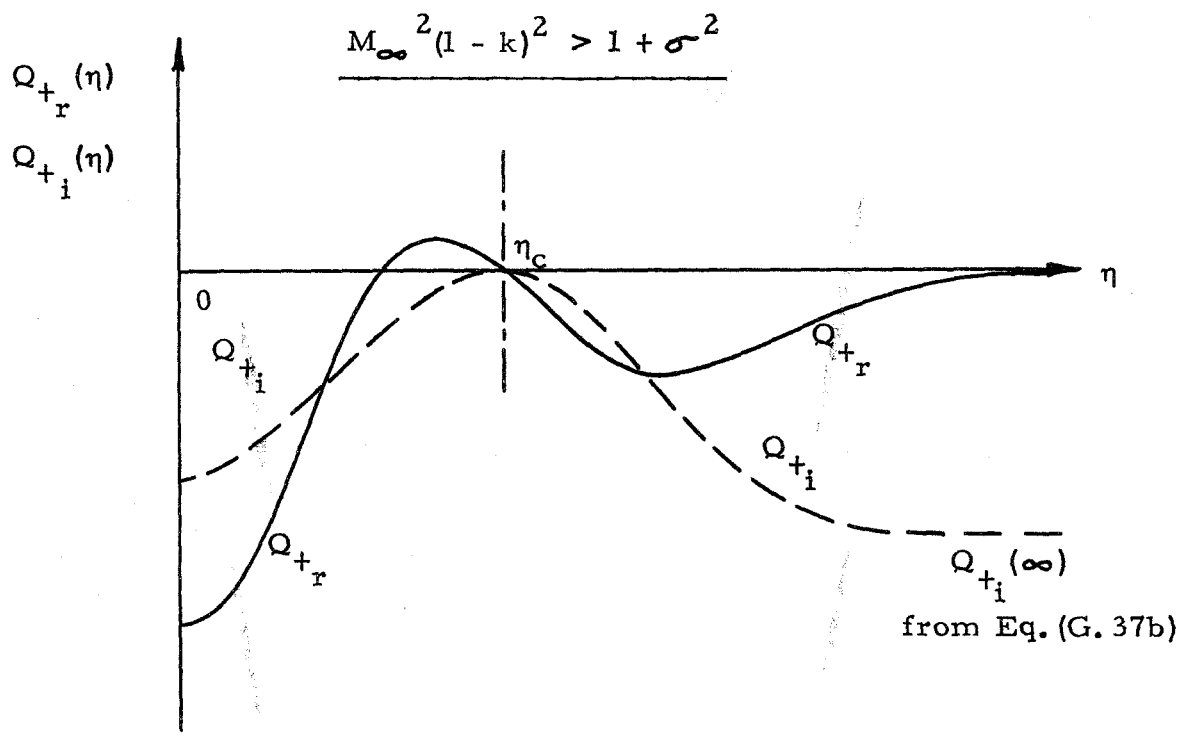

The explanation for this case is the same as for Case 1 except that now there are two constants C_r and C_i to be determined so that the outer boundary condition (G. 37b) is satisfied. Once these constants are determined, the integration can again proceed inward from the critical layer to the wall.

The actual integration follows the same lines as in Case 1 except that in steps (2) and (3) simultaneous integration of Eqs. (G. 36) is required for $\eta > \eta_c$ as well. Steps (5) and (6) now read C_r and C_i instead of just C_r .

G. 4. 2 Numerical Solution of Equation for P_-

Following the same procedure as for P_+, the differential equations for

$$Q_- = \frac{P_-'}{P_-} \qquad \text{(G. 41)}$$

are

$$Q_{-r}' = \frac{2V_-'}{V_-} Q_{-r} - (Q_{-r}^2 - Q_{-i}^2) + \kappa^2 \left[1 + \sigma^2 - V_-^2 \right], \qquad \text{(G. 42a)}$$

$$Q_{-i}' = \frac{2V_-'}{V_-} Q_{-i} - 2Q_{-r} Q_{-i} \quad , \qquad \text{(G. 42b)}$$

where $V_-(\eta)$ is defined by Eq. (G. 24) . Eqs. (G. 34) lead to the outer boundary conditions

$$Q_{-r} = -\kappa \sqrt{1 + \sigma^2 - M_\infty^2 (1 + k)^2} \quad , \quad Q_{-i} = 0 \qquad \text{(G. 43a)}$$

or

$$Q_{-r} = 0 \quad , \quad Q_{-i} = \kappa \sqrt{M_\infty^2 (1 + k)^2 - (1 + \sigma^2)} \qquad \text{(G. 43b)}$$

as $\eta \to \infty$ depending on whether $1 + \sigma^2$ is greater than or less than $M_\infty{}^2(1 + k)^2$ respectively.

Since $V_-(\eta)$ does not vanish anywhere in the region of interest, the numerical integration of Eqs. (G.42) from infinity into the wall can be carried out straightaway. The nature of the solution for Q_- is depicted in the following two sketches:

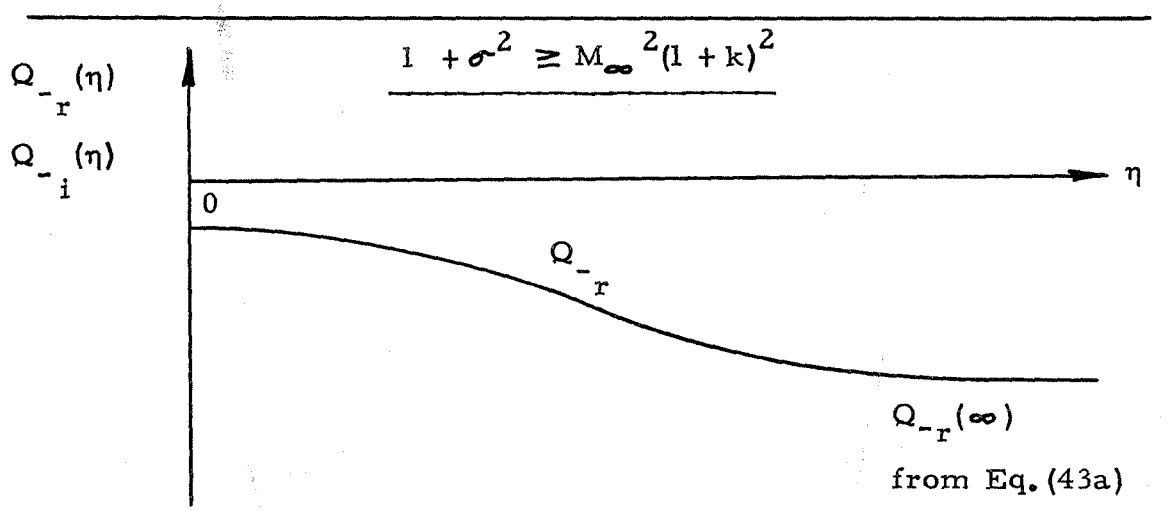

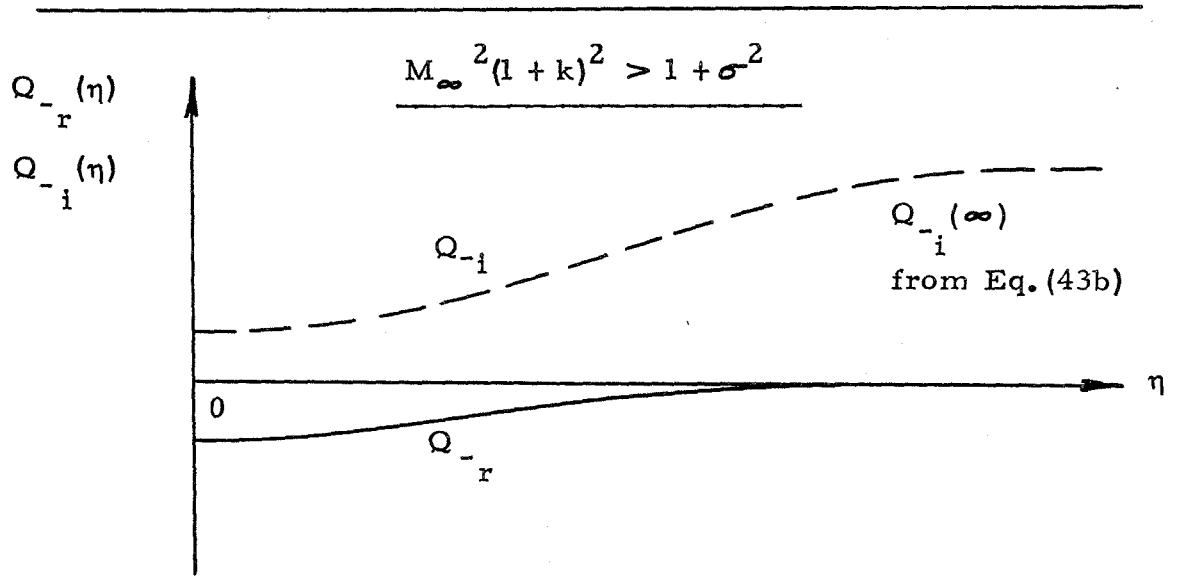

G.4.3 Pressure Perturbation on Wall

Once the solutions for Q_+ and Q_- are known on the wall, the pressure perturbation on the wall may be calculated from Eqs. (G.12). Solving Eqs. (G.34) and (G.41) for real and imaginary parts yields

$$R'\ell\ P_{\pm}(0) = \frac{\ell'_m Q_{\pm}(0) \cdot \ell'_m P'_{\pm}(0)}{\left| Q_{\pm}(0) \right|^2} , \qquad \text{(G.44a)}$$

and

$$\ell'_m\ P_{\pm}(0) = \frac{R'\ell\ Q_{\pm}(0) \cdot \ell'_m P_{\pm}'(0)}{\left| Q_{\pm}(0) \right|^2} , \qquad \text{(G.44b)}$$

where from Eq. (G.29)

$$\ell'_m\ P_{\pm}'(0) = \mp \frac{\alpha \gamma k^2 \kappa\ M_\infty{}^2}{2 + (\gamma - 1)\ M_\infty{}^2} . \qquad \text{(G.45)}$$

Evaluating Eq. (G.12) at the wall and substituting from Eqs. (G.44) and (G.45) yields the pressure on the oscillating wall

$$p(x, y, t) = \sin\beta y \, e^{-i\omega^* t} \left[P_s e^{i\varphi_s} \sin\alpha x + P_c e^{i\varphi_c} \cos\alpha x \right], \quad \text{(G.46)}$$

where

$$\left.\begin{aligned} P_s &= \left| P_+(0) - P_-(0) \right| , \\ \varphi_s &= \mathrm{Arg}\left[P_+(0) - P_-(0) \right] + \frac{\pi}{2} , \\ P_c &= \left| P_+(0) + P_-(0) \right| , \\ \varphi_c &= \mathrm{Arg}\left[P_+(0) + P_-(0) \right] . \end{aligned}\right\} \quad \text{(G.47)}$$

G.5 Results and Discussions

The calculations described in Section G.4 were performed on the IBM 7090/7094 of the California Institute of Technology Computing Center. The method of Runge-Kutta-Gill was used for the numerical integration of the differential equations.

The results for k = 0.5 and 0.75 are shown in Figs. G.2 to G.5 along with the corresponding results from potential theory and piston theory. It is seen that the boundary layer results rapidly approach the potential solution results as the boundary layer thickness parameter κ decreases. It is also interesting to note that both of these results approach the piston theory result as the three dimensionality parameter σ goes to zero.

As noted in Section 2.3, the boundary layer thickness for the experimental configurations reported herein was about 0.2 inches.* Hence, κ would be about 0.02, 0.04 and 0.06 for the observed flutter modes. The results in Figs. G.2 to G.5 indicate that for these values of κ, the boundary layer results are reasonably close to the potential solution results. Hence, in that sense, the influence of the boundary layer may be ignored. However, it must be emphasized that the present analysis is not valid for disturbances with very short wave lengths in the streamwise direction, so that the foregoing statements may not be valid then.

The peculiar singularities shown in Figs. G.2 to G.5 at particular values of σ are a result of singularities in the outer boundary conditions which the pressure perturbation quantities P_+ and P_- are forced to satisfy. For example, as shown in Eqs. (G.32), the outer boundary condition which $Q_+ = P_+'/P_+$ satisfies, has a branch point at $\sigma = \sigma_{cr}$ where

$$\sigma_{cr}^2 = M_\infty^2(1 - k)^2 - 1.$$

The same thing is true for $Q_- = P_-'/P_-$ with

$$\sigma_{cr}^2 = M_\infty^2(1 + k)^2 - 1 \quad .$$

---

* The measurement of 0.4 inches was obtained at the downstream end of the shell, so that 0.2 inches represents some sort of average over the whole shell.

At these critical values of σ, the outer boundary condition changes from one of radiation to one of exponential decay, and the resulting singularity simply reflects the breakdown of the inviscid theory. It is interesting to note that these singularities do not occur for the cylindrical potential theory results (Appendix F), apparently because of the attenuating effect of the cylindrical geometry. However, the results do show "resonance" peaks. See for example, Ref. 19.

APPENDIX H

SERIES SOLUTION OF P_+ EQUATION IN APPENDIX G ABOUT CRITICAL POINT

In treating the equation for P_+ (the z dependent amplitude of that part of the pressure perturbation which has the form of a traveling wave in the + x direction) a regular singularity appears at the critical point (where U = k). The solution of this equation in the neighborhood of the critical point is obtained by a series expansion that is sometimes called the Method of Frobenius. Although the numerical solution is performed on the equivalent first order nonlinear equation, the series expansion will be performed on the second order linear equation (Eq. G. 22).

$$P'' - \frac{2V'}{V} P' + \kappa^2 \left[V^2 - (1 + \sigma^2) \right] P = 0 \quad , \qquad (H.1)$$

where

$$V = \frac{M_\infty (U(\eta) - k)}{\sqrt{\overline{T}(\eta)}} \quad . \qquad (H.2)$$

The plus sign subscripts have been dropped for clarity.

Let $\xi = \eta - \eta_c$ and assume a solution of the form

$$P = \xi^s (a_o + a_1\eta + a_2\eta^2 + \ldots) \quad . \tag{H.3}$$

Since $V = 0$ at $\xi = 0$, in the neighborhood of the critical point

$$\frac{2V'}{V} = \frac{2}{\xi} + A + B\xi + \ldots \quad , \tag{H.4}$$

and

$$V^2 = \left[(V')^2\right]_c \xi^2 + \left[V'V''\right]_c \xi^3 + \ldots \quad , \tag{H.5}$$

where

$$A = \left[\frac{V''}{V'}\right]_c \tag{H.6}$$

and

$$B = \left[\frac{2}{3}\,\frac{V'''}{V'} - \frac{1}{2}\left(\frac{V''}{V'}\right)^2\right]_c \quad . \tag{H.7}$$

Relations (H.3) to (H.5) are substituted into Eq. (H.1), and the coefficients of each power of ξ are made to vanish. The leading power of ξ is ξ^{s-2}, and its coefficient vanishes when

$$a_o \left[s(s-1) - 2s \right] = 0 \quad . \qquad \text{(H. 8)}$$

Since $a_o \neq 0$, $s = 0$ or 3. The coefficient a_o is set equal to 1 without loss of generality. The values of a_1, a_2 ... for the solution corresponding to $s = 3$ (designated P_1) are found from the condition that the coefficients of the ξ^{s-1}, ξ^s, ... terms vanish. The resulting solution is

$$P_1 = \xi^3 + \frac{3}{4} A \xi^4 + \frac{\kappa^2(1+\sigma^2) + 3(B + A^2)}{10} \xi^5 + \ldots \quad . \qquad \text{(H. 9)}$$

Since the characteristic exponents differ by an integer, the second linearly independent solution of Eq. (H.1) has the form

$\underline{\xi > 0}$

$$P_2 = KP_1 \ln\xi + 1 + b_1\xi + b_2\xi^2 + b_3\xi^3 + b_4\xi^4 + \ldots \qquad \text{(H.10a)}$$

$\underline{\xi < 0}$

$$P_2 = KP_1(\ln|\xi| - i\pi) + 1 + b_1\xi + b_2\xi^2 + b_3\xi^3 + b_4\xi^4 + \ldots \qquad \text{(H.10b)}^*$$

---

* The negative sign for the π term in the second equation is chosen to provide the proper analytic continuation of the solution about the critical point. A treatment of the full viscous equations shows that the proper path of integration lies below the critical point in the complex η plane for the case when $U_c' > 0$; cf. Appendix G of Ref. 37.

Substitution of Eqs. (H.10) into Eq. (H.1) yields for P_2:

$\underline{\xi > 0}$

$$P_2 = -\frac{\kappa^2(1+\sigma^2)A}{3} P_1 \ell n\,\xi + 1 - \frac{\kappa^2(1+\sigma^2)}{2}\xi^2 -$$

$$\frac{\kappa^2}{4}\left\{(1+\sigma^2)\left[B + \kappa^2(1+\sigma^2) - \frac{11}{12}A^2\right] + \left[(V')^2\right]_c\right\}\xi^4 + b_3 P_1 + \ldots \qquad \text{(H.11a)}$$

$\underline{\xi < 0}$

Now, replace $\ell n\,\xi$ by $\ell n|\xi| - i\pi$ in Eq. (H.11a). (H.11b)

The coefficient b_3 is not determined in the procedure and so remains arbitrary. Hence Eqs. (H.11) represent the general solution to Eq. (H.1).

For use in the numerical solution for P_+, Eqs. (H.11) are expressed in terms of $Q = P_2'/P_2$. This becomes

$$Q = -\kappa^2(1+\sigma^2)\xi\left\{1 + A\xi\,\ell n\xi - C\xi + \left[A^2(\ell n\xi - 1) + B + \kappa^2(1+\sigma^2) - AC + \frac{\left[(V')^2\right]_c}{1+\sigma^2}\right]\xi^2 + A\xi^3\left[\kappa^2(1+\sigma^2) + \frac{1}{2}(B + A^2)\right]\ell n\,\xi + \ldots\right\}, \qquad \text{(H.12)}$$

where C is an arbitrary constant which may be complex (i.e. $C = C_r + iC_i$) and $\ell n\ \xi$ is replaced by $\ell n\ |\xi| - i\pi$ for $\xi < 0$. Hence the real and imaginary parts of Q are as follows:

$$Q_r = -\kappa^2(1+\sigma^2)\ \xi \left\{ 1 + A\xi\ \ell n\ |\xi| - C_r\xi + \left[A^2(\ell n\ |\xi| - 1) + B + \kappa^2(1+\sigma^2) - AC_r + \frac{\left[(V')^2\right]_c}{1+\sigma^2} \right] \xi^2 + A\xi^3 \left[\kappa^2(1+\sigma^2) + \frac{1}{2}(B + A^2) \right] \ell n\ |\xi| + \ldots \right\} \qquad \text{(H.13)}$$

For $\xi > 0$

$$Q_i = \kappa^2(1+\sigma^2)\ C_i\xi^2 \left\{ 1 + A\xi + \left[\kappa^2(1+\sigma^2) + \frac{1}{2}(B + A^2) \right] \xi^2 + \ldots \right\} \qquad \text{(H.14a)}$$

For $\xi < 0$

$$Q_i = \kappa^2(1+\sigma^2)\ (C_i + A\pi)\ \xi^2 \left\{ 1 + A\xi + \left[\kappa^2(1+\sigma^2) + \frac{1}{2}(B + A^2) \right] \xi^2 + \ldots \right\} . \qquad \text{(H.14b)}$$

REFERENCES

1. Stearman, R. O., Lock, M. H., and Fung, Y. C., "Ames Tests on the Flutter of Cylindrical Shells", GALCIT Structural Dynamics Report SM 62-37, December 1962.
2. Fung, Y. C., "Some Recent Contributions to Panel Flutter Research", AIAA Journal, 1, pp. 898-909, 1963.
3. Fung, Y. C., and Sechler, E. E., "Instability of Thin Elastic Shells". Structural Mechanics. Proceedings of First Symposium on Naval Structural Mechanics, pp. 115 - 167, Pergamon Press, 1960.
4. Anderson, W. J., and Fung, Y. C., "The Effect of an Idealized Boundary Layer on the Flutter of Cylindrical Shells in Supersonic Flow", GALCIT Structural Dynamics Report SM 62-49, December 1962.
5. Anderson, W. J., "Supersonic Wind Tunnel Tests of Wavy-Walled Cylinders", Aerospace Research Laboratories, 65-203, USAF, October 1965.
6. Voss, H. M., "The Effect of an External Supersonic Flow on the Vibration Characteristics of Thin Cylindrical Shells", Institute of Aerospace Sciences, Vol. 28, No. 12, pp. 945-956, 1961.
7. Leonard, R. W. and Hedgepeth, J. M., "On Panel Flutter and Divergence of Infinitely Long Unstiffened and Ring-Stiffened Thin-Walled Circular Cylinders", NACA Report 1302, 1957.
8. Samanich, N. E., "Pressure Drag of Axisymmetric Cowls Having Large Initial Lip Angles at Mach Numbers from 1.9 to 4.9", NACA Memorandum 1-10-59E, January 1959.

9. Kobayashi, S., "Supersonic Panel Flutter of Unstiffened Circular Cylindrical Shells Having Simply Supported Ends", Japan Society for Aeronautical and Space Sciences, Vol. 6, No. 9, 1963.

10. Evensen, D. A., "Non-Linear Flexural Vibrations of Thin Circular Rings", Ph.D. Thesis, California Institute of Technology, June 1964. (Later published as NASA TR-227, December 1965).

11. Olson, M. D., "Some Experimental Observations on the Non-Linear Vibration of Cylindrical Shells", AIAA Journal, 3, pp. 1775-1777, 1965.

12. Arnold, R. N. and Warburton, G. B., "Flexural Vibrations of the Walls of Thin Cylindrical Shells Having Freely Supported Ends", Proceedings of the Royal Society (London), Series A, Vol. 197, p. 238, 1949.

13. Fung, Y. C., Sechler, E. E. and Kaplan, A., "On the Vibrations of Thin Cylindrical Shells under Internal Pressure", Journal of Aeronautical Sciences, Vol. 24, No. 9, pp. 650-660, 1957.

14. Arnold, R. N. and Warburton, G. B., "The Flexural Vibrations of Thin Cylinders", Journal and Proceedings of the Institution of Mechanical Engineers (London), Vol. 167, pp. 62-74, 1953.

15. Forsberg, K., "Influence of Boundary Conditions on the Modal Characteristics of Thin Cylindrical Shells", AIAA Journal, Vol. 2, No. 12, pp. 2150-2157, 1964.

16. Young, D. and Felgar, R. P., Jr., "Tables of Characteristic Functions Representing Normal Modes of Vibration of a Beam", Engineering Research Series No. 44, University of Texas, Bureau of Engineering Research, July 1949.

17. Felgar, R. P., Jr., "Formulas for Integrals Containing Characteristic Functions of Vibrating Beam", University of Texas, Circular No. 14, Bureau of Engineering Research, 1950.

18. Krumhaar, H., "The Accuracy of Applying Linear Piston Theory to Cylindrical Shells", GALCIT Structural Dynamics Report SM 62-50, March 1963.

19. Anderson, W. J., "Oscillatory Pressures in an Idealized Boundary Layer with an Application to the Panel Flutter of Cylindrical Shells", AIAA Symposium on Structural Dynamics and Aeroelasticity, Boston, Massachusetts, August 30 - September 1, 1965.

20. Fung, Y. C., "A Summary of the Theories and Experiments on Panel Flutter", GALCIT Report AFOSR TN 60-224, May 1960. (Also published as "Panel Flutter", Agard Manual on Aeroelasticity, November 1959).

21. Johns, D. J., "A Survey on Panel Flutter", Structures and Materials Panel of AGARD, November 1965. (To be published as an AGARD Report).

22. Krumhaar, H., "Supersonic Flutter of a Cylindrical Shell of Finite Length in an Axisymmetric Mode", GALCIT Report AFOSR 1574, October 1961. (Later published in International Journal of Solids and Structures, Vol. 1, pp. 23-57 (1965), Pergamon Press, London).

23. Reissner, E., "Non-Linear Effects in Vibrations of Cylindrical Shells", Aeromechanics Report No. AM 5-6, Ramo-Woolridge Corporation, August 1955.

24. Evensen, D. A., "Some Observations on the Nonlinear Vibrations of Thin Cylindrical Shells" , AIAA Journal, Vol. 1, No. 12, pp. 2857-2758, December 1963.

25. Babcock, C. D., Jr., "The Buckling of Cylindrical Shells with an Initial Imperfection under Axial Compression Loading", Ph. D. Thesis, California Institute of Technology, June 1962.

26. Parmerter, R. R., "The Buckling of Clamped Shallow Spherical Shells under Uniform Pressure", GALCIT Structural Dynamics Report SM 63-53, AFOSR 5362 , November 1963.

27. Schmidt, L. V., "Measurements of Fluctuating Air Loads on a Circular Cylinder", Ph. D. Thesis, California Institute of Technology, June 1963.

28. Weingarten, V. I., Morgan, E. J. and Seide, P., "Final Report on Development of Design Criteria for Elastic Stability of Thin Shell Structures", STL/TR-60-0000-19425, Space Technology Laboratories, Inc., December 31, 1960.

29. Babcock, C. D., and Sechler, E. E., "The Effect of End Slope on the Buckling Stress of Cylindrical Shells", NASA TN D-2537, December 1964.

30. Becker, H. and Gerard, G., "Handbook of Structural Stability, Part III", NACA TN 3783, 1957-58.

31. Liepmann, H. W. and Roshko, A., Elements of Gasdynamics, John Wiley and Sons, February 1960.

32. Miles, J. W., "On Panel Flutter in the Presence of a Boundary Layer", Journal Aerospace Science 26, pp. 81-93, 1959.

33. McClure, J. D., "On Perturbed Boundary Layer Flows", MIT Fluid Dynamics Research Laboratory Report 62-2, June 1962.

34. McClure, J. D., "Regular Disturbances in the Turbulent Boundary Layer", Boeing Scientific Research Laboratories, D1-82-0397, January 1965.

35. Reshotko, E., "Stability of the Compressible Laminar Boundary Layer", GALCIT Hypersonic Research Project Memorandum No. 52, January 1960.

36. Coles, D., "Measurements in the Boundary Layer on a Smooth Flat Plate in Supersonic Flow III. Measurements in a Flat Plate Boundary Layer at the Jet Propulsion Laboratory", Jet Propulsion Laboratory Report No. 20-71, California Institute of Technology, June 1953.

37. Gold, H., "Stability of Laminar Wakes", Ph.D. Thesis, California Institute of Technology, June 1963.

TABLE I

FLUTTER DATA FOR SHELL NO. 1 ($h = 0.0040$ INCHES AND $P_x = 0$)

Corr. No.	Run No.	p_{t_∞} (psfa)	T_{t_∞} (^oF)	p_m (psig)	M_∞	$\frac{w_{rms}^1}{h}$	$\frac{x}{L}$	$\frac{w_{rms}^2}{h}$	θ (deg)	$\frac{w_{rms}^3}{h}$	j**	n**	f* (cps)
18	1	694	68.7	2.45	2.993	0.04	0.35	0.04	108	0.02	-	-	(a)
19	1	1045	73.5	2.45	2.993	0.05	0.35	0.06	108	0.03	-	-	(a)
20	1	1400	81.0	2.21	3.381	0.06	0.35	0.07	108	0.03	-	-	(a)
21	1	1754	87.9	2.21	3.381	0.07	0.35	0.08	108	0.03	-	-	(a)
22	2	1755	94.9	1.00	3.381	0.08	0.35	0.09	108	0.03	-	-	(a)
23	2	1934	98.4	0.98	3.381	0.07	0.35	0.10	108	0.03	-	-	(a)
24	2	2115	102.1	0.98	3.381	0.09	0.35	0.12	108	0.03	-	-	(a)
25	2	2248	104.4	0.98	3.381	0.09	0.35	0.11	108	0.03	-	-	(a)
26	2	2395	107.7	0.98	3.381	0.09	0.35	0.13	108	0.04	-	-	(a)

* The frequencies f were obtained from power spectral analysis of the pickup signals. The letters in the brackets indicate which one of the motions depicted in figure 12 was present.

** The circumferential wave number n and the circumferential nodal line number j were obtained from traverse plots.

TABLE I (cont.)

FLUTTER DATA FOR SHELL NO. 1 (h = 0.0040 INCHES AND P_x = 0)

Corr. No.	Run No.	p_{t_∞} (psfa)	T_{t_∞} (^oF)	p_m (psig)	M_∞	$\frac{w_{rms}^1}{h}$	$\frac{x}{L}$	$\frac{w_{rms}^2}{h}$	θ (deg)	$\frac{w_{rms}^3}{h}$	j	n	f (cps)
27	2	2539	111.0	0.98	3.381	0.09	0.35	0.14	108	0.05	-	-	(a)
28	2	2679	114.6	0.98	3.381	0.11	0.35	0.14	108	0.04	-	-	(a)
29	2	2814	117.2	0.98	3.381	0.11	0.35	0.14	108	0.05	-	-	(a)
30	2	2961	121.7	0.98	3.381	0.12	0.35	0.14	108	0.06	-	-	(a)
31	2	2961	122.4	0.74	3.381	0.12	0.35	0.14	108	0.06	-	-	(a)
32	2	2961	120.9	0.52	3.381	0.12	0.35	0.14	108	0.06	-	-	(a)
33	2	2962	123.7	0.29	3.381	0.12	0.35	0.14	108	0.06	-	-	(a)
34	2	3176	128.8	0.98	3.381	0.12	0.35	0.14	108	0.06	-	-	(a)
35	2	3178	128.7	0.52	3.381	0.13	0.35	0.14	108	0.06	-	-	(a)
36	2	2818	121.4	0.49	3.381	0.12	0.35	0.14	108	0.04	-	-	(a)
37	2	2459	115.7	0.49	3.381	0.11	0.35	0.12	108	0.04	-	-	(a)
38	2	2113	107.9	0.49	3.381	0.09	0.35	0.11	108	0.03	-	-	(a)
39	2	1760	101.2	0.49	3.381	0.07	0.35	0.08	108	0.03	-	-	(a)

TABLE I (cont.)

FLUTTER DATA FOR SHELL NO. 1 ($h = 0.0040$ INCHES AND $P_x = 0$)

Corr. No.	Run No.	p_{t_∞} (psfa)	T_{t_∞} (^oF)	p_m (psig)	M_∞	$\frac{w_{rms}^1}{h}$	$\frac{x}{L}$	$\frac{w_{rms}^2}{h}$	θ (deg)	$\frac{w_{rms}^3}{h}$	j	n	f (cps)
40	2	1405	94.3	0.49	3.381	0.06	0.35	0.07	108	0.03	-	-	(a)
41	2	1047	90.0	0.49	3.381	0.05	0.35	0.05	108	0.02	-	-	(a)

TABLE II

FLUTTER DATA FOR SHELL NO. 2 ($h = 0.0039$ INCHES AND $M_\infty = 2.993$)

Corr. No.	Run No.	p_{t_∞} (psfa)	T_{t_∞} (^oF)	p_m (psig)	P_x (lb)	$\frac{w_{rms}^1}{h}$	$\frac{x}{L}$	$\frac{w_{rms}^2}{h}$	θ (deg)	$\frac{w_{rms}^3}{h}$	j	n	f* (cps)
109	3	699	71.4	0.98	0	0.04	0.3	0.02	-58	0.03	-	-	(a)
110	3	1047	77.2	0.98	0	0.04	0.3	0.04	-58	0.04	-	-	(a)
111	3	1402	84.9	0.98	0	0.06	0.3	0.04	-58	0.04	-	-	(a)
112	3	1758	94.0	0.98	0	0.15	0.3	0.12	-58	0.07	1**	20	652(b)
113	3	2113	102.3	0.98	0	0.24	0.3	0.32	-58	0.24	-	-	649(b)
114	3	2461	111.5	0.98	0	0.13	0.3	0.14	-58	0.11	-	-	(a)
115	3	2824	119.5	0.98	0	0.24	0.3	0.46	-58	0.49	-	-	653(c)
116	3	3168	133.6	0.98	0	0.17	0.3	0.31	-58	0.38	-	-	829(c)
117	3	3056	133.5	0.37	0	0.17	0.3	0.18	-58	0.16	-	-	502(c)

* See note under Table I

** This j was estimated from the phase angle relation between w_1 and w_2, since no axial traverse was recorded for this Corr. No.

TABLE II (cont.)

FLUTTER DATA FOR SHELL NO. 2 ($h = 0.0039$ INCHES AND $M_\infty = 2.993$)

Corr. No.	Run No.	p_{t_∞} (psfa)	T_{t_∞} (^oF)	p_m (psig)	P_x (lb)	$\frac{w_{rms}^1}{h}$	$\frac{x}{L}$	$\frac{w_{rms}^2}{h}$	θ (deg)	$\frac{w_{rms}^3}{h}$	j	n	f^* (cps)
118	3	2814	128.2	0.37	0	0.22	0.3	0.24	-58	0.23	-	-	507(b)
119	3	2465	121.5	0.37	0	0.16	0.3	0.15	-58	0.14	-	-	516(c)
120	3	2108	114.8	0.37	0	0.10	0.3	0.07	-58	0.08	-	-	(a)
121	3	1757	107.9	0.37	0	0.08	0.3	0.08	-58	0.05	-	-	(a)
122	3	1400	99.2	0.37	0	0.06	0.3	0.05	-58	0.05	-	-	(a)
123	3	1053	92.7	0.37	0	0.05	0.3	0.06	-58	0.04	-	-	(a)
124	3	702	86.9	0.37	0	0.04	0.3	0.04	-58	0.04	-	-	(a)
125	4	2110	108.8	0.98	0	0.14	0.3	0.22	-58	0.17	2	20	653(b)
126	4	2819	127.0	0.98	0	0.30	0.5	0.46	-58	0.42	2	25	835(b)
130	5	2111	114.1	0.25	0	0.10	0.3	0.03	-58	0.08	-	-	(a)
132	5	2113	114.4	0.10	0	0.11	0.3	0.03	-58	0.08	-	-	(a)
133	5	2113	114.7	0.066	0	0.11	0.3	0.03	-58	0.09	-	-	(a)
134	5	2112	114.2	0.040	0	0.10	0.3	0.03	-58	0.09	-	-	(a)

TABLE II (cont.)

FLUTTER DATA FOR SHELL NO. 2 ($h = 0.0039$ INCHES AND $M_\infty = 2.993$)

Corr. No.	Run No.	p_{t_∞} (psfa)	T_{t_∞} (^oF)	p_m (psig)	P_x (lb)	$\frac{w_{rms}^1}{h}$	$\frac{x}{L}$	$\frac{w_{rms}^2}{h}$	θ (deg)	$\frac{w_{rms}^3}{h}$	j	n	f (cps)
135	5	2111	114.4	0.024	0	0.10	0.3	0.03	-58	0.08	-	-	(a)
136	5	2112	114.7	0.018	0	0.10	0.3	0.03	-58	0.10	-	-	(a)
137	5	2113	115.5	0.006	0	0.10	0.3	0.03	-58	0.08	-	-	(a)
138	5	2113	115.2	0	0	0.11	0.3	0.03	-58	0.09	-	-	(a)
139	5	2112	116.1	-0.004	0	0.12	0.3	0.05	-58	0.09	-	-	(a)
146	6	1047	77.0	3.93	0	0.05	0.3	0.04	-58	0.03	-	-	(a)
147	6	1403	84.7	3.93	0	0.07	0.3	0.05	-58	0.04	-	-	(a)
148	6	1755	92.1	3.93	0	0.08	0.3	0.05	-58	0.05	-	-	(a)
149	6	2110	100.8	3.93	0		0.3	0.05	-58	0.05	-	-	(a)
150	6	2464	111.1	3.93	0	0.09	0.3	0.06	-58	0.06	-	-	(a)
151	6	2816	121.8	3.93	0	0.10	0.3	0.07	-58	0.08	-	-	(a)
152	6	3172	132.1	3.93	0	0.11	0.3	0.06	-58	0.08	-	-	(a)
153	7	3171	133.1	3.93	190	0.09	0.3	0.06	-58	0.08	-	-	(a)

TABLE II (cont.)

FLUTTER DATA FOR SHELL NO. 2 (h = 0.0039 INCHES AND M_∞ = 2.993)

Corr. No.	Run No.	p_{t_∞} (psfa)	T_{t_∞} (^oF)	p_m (psig)	P_x (lb)	$\frac{w_{rms}^1}{h}$	$\frac{x}{L}$	$\frac{w_{rms}^2}{h}$	θ (deg)	$\frac{w_{rms}^3}{h}$	j	n	f (cps)
154	7	3174	137.3	3.93	400	0.08	0.3	0.06	-58	0.08	-	-	(a)
155	7	3170	135.4	3.93	580	0.09	0.3	0.06	-58	0.08	-	-	(a)
156[/]	7	3173	136.6	3.93	700	0.11	0.3	0.09	-58	0.11	-	-	(a)
157	8	2821	131.3	0.98	0	0.91	0.3	0.94	-58	0.99	-	-	573(c)
158	8	2819	130.3	0.35	0	0.51	0.3	0.42	-58	0.56	0	14	242(c)
159	8	2818	129.5	0.25	0	1.18	0.3	1.04	-58	0.79	-	-	238(c)
160	8	2820	127.7	0.16	0	1.13	0.3	1.06	-58	0.79	0	15	195(c)
161	8	2820	128.6	0.070	0	1.10	0.3	1.12	-58	0.97	-	-	129(d)
162	8	2819	130.4	0.020	0	1.55	0.3	1.29	-58	0.99	0	local*	92(d)
163	8	2820	127.9	0.003	0	1.21	0.3	1.18	-58	0.73	-	-	75(d)

[/] Buckling in single bellows mode occurred here.

* Indicates localized flutter. Cf. figure 22.

TABLE II (cont.)

FLUTTER DATA FOR SHELL NO. 2 ($h = 0.0039$ INCHES AND $M_\infty = 2.993$)

Corr. No.	Run No.	p_{t_∞} (psfa)	T_{t_∞} (^oF)	p_m (psig)	P_x (lb)	$\frac{w_{rms}^1}{h}$	$\frac{x}{L}$	$\frac{w_{rms}^2}{h}$	θ (deg)	$\frac{w_{rms}^3}{h}$	j	n	f (cps)
164	8	2467	122.8	0.002	0	0.84	0.3	0.81	-58	0.63	-	-	82(d)
165	9	2111	112.2	0.002	0	0.16	0.3	0.12	-58	0.11	-	-	(a)
166	9	2112	112.1	-0.013	0	0.15	0.3	0.12	-58	0.12	-	-	(a)
167	9	2466	119.0	0.014	0	1.10	0.3	1.00	-58	0.96	0	local	90(d)
168	9	2466	119.4	0	0	0.20	0.3	0.20	-58	0.21	-	-	(a)
169	9	2466	118.0	-0.006	0	0.25	0.3	0.29	-58	0.23	-	-	(a)
170	9	2466	119.5	-0.013	0	0.22	0.3	0.18	-58	0.20	-	-	(a)
171	9	2466	117.2	-0.017	0	0.24	0.3	0.20	-58	0.21	-	-	(a)
172	9	2465	117.5	-0.023	0	0.24	0.3	0.23	-58	0.27	-	-	(a)
173	9	2465	118.9	0.054	0	0.79	0.3	0.72	-58	0.51	-	-	138(c)
174	9	2464	118.8	0.099	0	1.01	0.3	0.89	-58	0.73	0	15	164(c)
175	10	2818	127.5	0.039	0	1.00	0.3	0.89	-58	0.70	-	-	132(c)
176	10	2817	129.0	0.001	0	1.05	0.3	0.89	-58	0.90	-	-	79(d)

TABLE II (cont.)

FLUTTER DATA FOR SHELL NO. 2 ($h = 0.0039$ INCHES AND $M_\infty = 2.993$)

Corr. No.	Run No.	p_{t_∞} (psfa)	T_{t_∞} (^oF)	p_m (psig)	P_x (lb)	$\frac{w_{rms}^1}{h}$	$\frac{x}{L}$	$\frac{w_{rms}^2}{h}$	θ (deg)	$\frac{w_{rms}^3}{h}$	j	n	f (cps)
177	10	2818	128.7	-0.006	0	0.94	0.3	0.77	-58	0.82	-	-	63(d)
178	10	2816	127.6	-0.012	0	0.81	0.3	0.66	-58	0.72	-	-	55(d)
179	10	2818	127.1	-0.017	0	0.73	0.3	0.61	-58	0.72	-	-	45(d)

Lateral buckling occurred here at $p_m = -0.023$ psig.

TABLE III

FLUTTER DATA FOR SHELL NO. 3 (h = 0.0040 INCHES AND M_∞ = 2.993)

Corr. No.	Run No.	p_{t_∞} (psfa)	T_{t_∞} (^oF)	p_m (psig)	P_x (lb)	$\frac{w_{rms}{}^1}{h}$	$\frac{x}{L}$	$\frac{w_{rms}{}^2}{h}$	θ (deg)	$\frac{w_{rms}{}^3}{h}$	j	n	f* (cps)
187	11	1769	93.6	3.93	0	0.09	0.3	0.05	-58	0.04	-	-	(a)
188	11	1769	95.1	1.96	0	0.07	0.3	0.05	-58	0.05	-	-	(a)
189	11	1769	95.4	0.98	0	0.14	0.3	0.10	-58	0.11	1	-	745(b)
190	11	1770	98.3	0.37	0	0.12	0.3	0.10	-58	0.10	1	-	332(b)
191	11	1769	98.4	0.11	0	0.08	0.3	0.06	-58	0.06	-	-	(a)
192	11	1768	100.7	-0.002	0	0.09	0.3	0.06	-58	0.05	-	-	(a)
193	11	1768	99.1	-0.005	0	0.09	0.3	0.06	-58	0.06	-	-	(a)
194	11	1768	101.3	-0.012	0	0.08	0.3	0.06	-58	0.06	-	-	(a)
195	11	1767	100.1	-0.018	0	0.09	0.3	0.06	-58	0.06	-	-	(a)
196	11	1768	102.7	-0.024	0	0.09	0.3	0.06	-58	0.06	-	-	(a)
197	12	1767	101.9	-0.015	90	0.09	0.3	0.06	-58	0.06	-	-	(a)

* See note under Table I

TABLE III (cont.)

FLUTTER DATA FOR SHELL NO. 3 ($h = 0.0040$ INCHES AND $M_\infty = 2.993$)

Corr. No.	Run No.	p_{t_∞} (psfa)	T_{t_∞} (^oF)	p_m (psig)	P_x (lb)	$\frac{w_{rms}{}^1}{h}$	$\frac{x}{L}$	$\frac{w_{rms}{}^2}{h}$	θ (deg)	$\frac{w_{rms}{}^3}{h}$	j	n	f (cps)
198	12	1767	101.6	-0.012	90	0.09	0.3	0.06	-58	0.06	-	-	(a)
199	12	1767	101.3	-0.006	90	0.09	0.3	0.06	-58	0.06	-	-	(a)
200	12	1767	102.1	0.002	90	0.09	0.3	0.06	-58	0.06	-	-	(a)
201	12	1767	102.2	0.006	90	0.09	0.3	0.08	-58	0.06	-	-	(a)
202	12	1767	101.2	0.37	90	0.15	0.3	0.11	-58	0.08	-	-	325(d)
203	12	1767	101.8	0.98	90	0.66	0.3	0.46	-58	0.45	1	20	642(c)
204	12	1767	102.2	1.47	90	0.13	0.3	0.09	-58	0.09	1	21	825(c)
205	12	1767	103.1	1.96	90	0.07	0.3	0.05	-58	0.05	-	-	(a)
206	12	1767	102.5	3.93	90	0.07	0.3	0.05	-58	0.05	-	-	(a)
207	13	1767	103.4	3.93	200	0.07	0.3	0.05	-58	0.05	-	-	(a)
208	13	1767	103.7	1.96	200	0.07	0.3	0.05	-58	0.05	-	-	(a)
209	13	1767	102.9	0.98	200	0.51	0.3	0.28	-58	0.28	1	20	648(c)
210	13	1767	102.8	0.49	200	0.15	0.3	0.10	-58	0.09	-	-	537(c)

TABLE III (cont.)

FLUTTER DATA FOR SHELL NO. 3 ($h = 0.0040$ INCHES AND $M_\infty = 2.993$)

Corr. No.	Run No.	p_{t_∞} (psfa)	T_{t_∞} (^oF)	p_m (psig)	P_x (lb)	$\frac{w_{rms}^1}{h}$	$\frac{x}{L}$	$\frac{w_{rms}^2}{h}$	θ (deg)	$\frac{w_{rms}^3}{h}$	j	n	f (cps)
211	13	1767	104.0	0.17	200	0.09	0.3	0.06	-58	0.05	-	-	(a)
212	13	1767	103.7	-0.003	200	0.09	0.3	0.06	-58	0.05	-	-	(a)
213	14	1767	103.9	0.25	300	0.11	0.3	0.07	-58	0.06	-	-	(a)
214	14	1767	103.4	0.49	300	0.13	0.3	0.09	-58	0.07	-	-	(a)
215	14	1767	103.4	0.98	300	0.58	0.3	0.34	-58	0.37	1	19	614(c)
216	14	1767	103.9	1.42	300	0.08	0.3	0.06	-58	0.05	-	-	(a)
217	14	1767	103.4	2.43	300	0.07	0.3	0.05	-58	0.05	-	-	(a)
218	15	1767	103.1	3.93	400	0.07	0.3	0.05	-58	0.04	-	-	(a)
219	15	1767	103.9	1.96	400	0.07	0.3	0.05	-58	0.05	-	-	(a)
228	16	2120	97.2	3.93	0	0.12	0.3	0.07	-58	0.06	-	-	(a)
229	16	2114	101.2	1.96	0	0.11	0.3	0.07	-58	0.07	-	-	(a)
230	16	2115	102.2	0.98	0	0.15	0.3	0.11	-58	0.10	-	-	(a)
231	16	2117	102.8	0.39	0	0.15	0.3	0.11	-58	0.10	-	-	(a)

TABLE III (cont.)

FLUTTER DATA FOR SHELL NO. 3 ($h = 0.0040$ INCHES AND $M_\infty = 2.993$)

Corr. No.	Run No.	p_{t_∞} (psfa)	T_{t_∞} (^oF)	p_m (psig)	P_x (lb)	$\frac{w_{rms}^1}{h}$	$\frac{x}{L}$	$\frac{w_{rms}^2}{h}$	θ (deg)	$\frac{w_{rms}^3}{h}$	j	n	f (cps)
232	16	2120	106.9	0.10	0	0.15	0.3	0.12	-58	0.10	-	-	(a)
234	16	2120	108.6	0	0	0.77	0.3	0.51	-58	0.26	-	-	104(d)
235	16	2120	108.4	-0.007	0	0.91	0.3	0.57	-58	0.30	0	local	94(d)
236	17	2119	109.5	0.37	90	0.13	0.3	0.11	-58	0.11	-	-	(a)
237	17	2119	107.6	0.74	90	0.09	0.3	0.13	-58	0.13	-	-	606(c)
238	17	2120	108.5	0.98	90	0.59	0.3	0.46	-58	0.44	1	20	652(c)
239	17	2121	108.6	1.24	90	0.13	0.3	0.08	-58	0.10	-	-	(a)
240	17	2120	108.5	1.96	90	0.10	0.3	0.07	-58	0.08	-	-	(a)
241	17	2123	108.6	0.12	90	0.15	0.3	0.11	-58	0.10	-	-	(a)
242	17	2123	108.9	0.003	90	0.56	0.3	0.40	-58	0.24	0	local	100(d)
243	17	2122	108.2	-0.006	90	0.82	0.3	0.47	-58	0.24	0	local	93(d)
244	17	2123	108.6	-0.012	90	0.90	0.3	0.52	-58	0.30	0	local	85(d)
245	18	2121	108.5	-0.011	0	1.04	0.3	0.64	-58	0.36	0	local	90(d)

TABLE III (cont.)

FLUTTER DATA FOR SHELL NO. 3 ($h = 0.0040$ INCHES AND $M_\infty = 2.993$)

Corr. No.	Run No.	p_{t_∞} (psfa)	T_{t_∞} (^oF)	p_m (psig)	P_x (lb)	$\frac{w_{rms}^1}{h}$	$\frac{x}{L}$	$\frac{w_{rms}^2}{h}$	θ (deg)	$\frac{w_{rms}^3}{h}$	j	n	f (cps)
246	18	2122	108.4	-0.018	0	1.22	0.3	0.72	-58	0.37	-	-	82(d)
247	18	2122	108.8	-0.023	0	1.22	0.3	0.71	-58	0.35	-	-	75(d)
248	19	2122	108.6	2.45	200	0.10	0.3	0.06	-58	0.06	-	-	(a)
249	19	2122	108.7	1.13	200	0.10	0.3	0.09	-58	0.08	-	-	(a)
250	19	2122	109.0	1.01	200	0.59	0.3	0.51	-58	0.52	1	19	625(c)
251	19	2121	108.0	0.78	200	0.56	0.3	0.43	-58	0.44	-	-	585(c)
252	19	2121	106.7	0.60	200	0.43	0.3	0.36	-58	0.34	1	21	550(b)
253	19	2122	107.8	0.54	200	0.15	0.3	0.11	-58	0.10	-	-	(a)
254	19	2121	107.9	0.26	200	0.13	0.3	0.11	-58	0.10	-	-	(a)
255	19	2120	107.9	0.11	200	0.15	0.3	0.12	-58	0.10	-	-	(a)
256	20	2121	107.1	0.25	300	0.20	0.3	0.12	-58	0.12	-	-	(a)
257	20	2125	108.1	0.68	300	0.51	0.3	0.43	-58	0.43	1	20	552(c)
258	20	2123	107.1	0.98	300	0.61	0.3	0.48	-58	0.47	1	19	612(c)

TABLE III (cont.)

FLUTTER DATA FOR SHELL NO. 3 ($h = 0.0040$ INCHES AND $M_\infty = 2.993$)

Corr. No.	Run No.	p_{t_∞} (psfa)	T_{t_∞} (^oF)	p_m (psig)	P_x (lb)	$\frac{w_{rms}^1}{h}$	$\frac{x}{L}$	$\frac{w_{rms}^2}{h}$	θ (deg)	$\frac{w_{rms}^3}{h}$	j	n	f (cps)
259	20	2122	107.6	1.15	300	0.15	0.3	0.11	-58	0.11	-	-	661(c)
260	20	2122	108.6	1.96	300	0.09	0.3	0.07	-58	0.07	-	-	(a)
261	21	2122	108.0	1.96	400	0.11	0.3	0.07	-58	0.07	-	-	(a)
262	21	2122	107.8	3.93	400	0.09	0.3	0.05	-58	0.06	-	-	(a)
263	22	2478	116.9	3.93	0	0.12	0.3	0.05	-58	0.07	-	-	(a)
264	22	2474	114.8	1.98	0	0.12	0.3	0.08	-58	0.09	-	-	(a)
265	22	2477	117.8	0.94	0	0.25	0.3	0.18	-58	0.19	-	-	636(c)
266	22	2476	117.9	0.82	0	0.43	0.3	0.33	-58	0.33	1	21	633(c)
267	22	2477	117.3	0.71	0	0.49	0.3	0.37	-58	0.40	-	-	590(c)
268	22	2475	117.4	0.51	0	0.23	0.3	0.18	-58	0.18	1	24	596(c)
269	22	2478	118.5	0.22	0	0.20	0.3	0.14	-58	0.12	-	-	(a)
270	22	2477	117.9	0	0	0.56	0.3	0.33	-58	0.22	-	-	100(d)
271	23	2475	118.3	0.11	90	0.20	0.3	0.15	-58	0.12	-	-	(a)

TABLE III (cont.)

FLUTTER DATA FOR SHELL NO. 3 ($h = 0.0040$ INCHES AND $M_\infty = 2.993$)

Corr. No.	Run No.	p_{t_∞} (psfa)	T_{t_∞} (^oF)	p_m (psig)	P_x (lb)	$\frac{w_{rms}^1}{h}$	$\frac{x}{L}$	$\frac{w_{rms}^2}{h}$	θ (deg)	$\frac{w_{rms}^3}{h}$	j	n	f (cps)
272	23	2476	119.6	0.41	90	0.33	0.3	0.28	-58	0.28	1	23	522(c)
273	23	2476	117.4	0.59	90	0.49	0.3	0.40	-58	0.40	-	-	577(b)
274	23	2476	117.5	0.83	90	0.74	0.3	0.64	-58	0.62	1	20	606(c)
275	23	2478	117.2	1.07	90	0.38	0.3	0.30	-58	0.32	-	-	676(c)
276	23	2477	116.2	1.30	90	0.21	0.3	0.12	-58	0.19	-	-	907(c)
277	23	2477	117.4	1.95	90	0.14	0.3	0.08	-58	0.09	-	-	(a)
278	23	2477	118.2	0	90	0.21	0.3	0.15	-58	0.12	-	-	(a)
279	23	2478	118.6	-0.006	90	0.20	0.3	0.15	-58	0.14	-	-	(a)
280	23	2473	119.4	-0.013	90	0.18	0.3	0.15	-58	0.14	-	-	(a)
281	24	2475	118.2	-0.002	0	0.20	0.3	0.17	-58	0.15	-	-	(a)
282	24	2476	116.9	-0.005	0	0.20	0.3	0.17	-58	0.14	-	-	(a)
283	24	2476	117.3	-0.012	0	0.21	0.3	0.17	-58	0.15	-	-	(a)
284	24	2477	117.6	-0.018	0	0.20	0.3	0.15	-58	0.15	-	-	(a)

TABLE III (cont.)

FLUTTER DATA FOR SHELL NO. 3 (h = 0.0040 INCHES AND M_∞ = 2.993)

Corr. No.	Run No.	p_{t_∞} (psfa)	T_{t_∞} (^oF)	p_m (psig)	P_x (lb)	$\frac{w_{rms}^1}{h}$	$\frac{x}{L}$	$\frac{w_{rms}^2}{h}$	θ (deg)	$\frac{w_{rms}^3}{h}$	j	n	f (cps)
285	24	2475	120.6	-0.023	0	0.21	0.3	0.17	-58	0.14	-	-	(a)
286	25	2475	118.1	-0.001	200	0.20	0.3	0.12	-58	0.12	-	-	(a)
287	25	2475	118.0	0.25	200	0.17	0.3	0.13	-58	0.12	-	-	(a)
288	25	2476	116.9	0.38	200	0.23	0.3	0.20	-58	0.21	-	-	480(c)
289	25	2474	118.1	0.68	200	0.48	0.3	0.36	-58	0.36	1	21	580(c)
290	25	2474	119.8	1.18	200	0.30	0.3	0.23	-58	0.21	-	-	670(b)
291	25	2475	118.7	1.96	200	0.13	0.3	0.08	-58	0.08	-	-	(a)
292	26	2474	117.5	1.96	300	0.12	0.3	0.08	-58	0.08	-	-	(a)
293	26	2474	118.0	1.09	300	0.41	0.3	0.30	-58	0.29	-	-	643(b)
294	26	2475	118.5	0.93	300	0.61	0.3	0.51	-58	0.51	1	19	595(c)
295	26	2474	118.7	0.48	300	0.46	0.3	0.36	-58	0.34	-	-	499(c)
296	26	2473	118.2	0.30	300	0.17	0.3	0.14	-58	0.12	-	-	(a)
297	27	2475	117.9	1.96	400	0.12	0.3	0.08	-58	0.09	-	-	(a)

TABLE III (cont.)

FLUTTER DATA FOR SHELL NO. 3 ($h = 0.0040$ INCHES AND $M_\infty = 2.993$)

Corr. No.	Run No.	p_{t_∞} (psfa)	T_{t_∞} (^oF)	p_m (psig)	P_x (lb)	$\frac{w_{rms}{}^1}{h}$	$\frac{x}{L}$	$\frac{w_{rms}{}^2}{h}$	θ (deg)	$\frac{w_{rms}{}^3}{h}$	j	n	f (cps)
298	27	2473	117.4	3.93	400	0.12	0.3	0.06	-58	0.07	-	-	(a)
299	28	2827	129.1	3.93	0	0.12	0.3	0.07	-58	0.08	-	-	(a)
300	28	2830	130.8	1.96	0	0.15	0.3	0.08	-58	0.11	-	-	(a)
301	28	2828	129.2	0.98	0	0.25	0.3	0.21	-58	0.22	-	-	652(c)
302	28	2828	128.3	0.92	0	0.49	0.3	0.37	-58	0.44	1	20	630(b)
303	28	2827	128.8	0.67	0	0.69	0.3	0.54	-58	0.55	-	-	582(c)
304	28	2828	127.8	0.39	0	0.54	0.3	0.45	-58	0.44	-	-	422(c)
305	28	2829	129.1	0.21	0	0.18	0.3	0.15	-58	0.17	-	-	(a)
306	28	2828	128.5	0.008	0	0.56	0.3	0.37	-58	0.34	0	local	100(d)
307	28	2827	128.2	-0.001	0	0.64	0.3		-58	0.32	-	-	92(d)
308	28	2826	128.6	-0.006	0	0.77	0.3		-58	0.41	-	-	86(d)
309	28	2827	127.2	-0.014	0	0.69	0.3	0.46	-58	0.37	-	-	77(d)
310	28	2828	127.4	-0.019	0	0.76	0.3	0.54	-58	0.41	0	local	71(d)

TABLE III (cont.)

FLUTTER DATA FOR SHELL NO. 3 ($h = 0.0040$ INCHES AND $M_\infty = 2.993$)

Corr. No.	Run No.	p_{t_∞} (psfa)	T_{t_∞} (^oF)	p_m (psig)	P_x (lb)	$\frac{w_{rms}^1}{h}$	$\frac{x}{L}$	$\frac{w_{rms}^2}{h}$	θ (deg)	$\frac{w_{rms}^3}{h}$	j	n	f (cps)
311	28	2827	127.4	-0.024	0	0.59	0.3	0.37	-58	0.28	-	-	64(d)
312	29	2827	127.7	-0.018	90	0.23	0.3	0.17	-58	0.17	-	-	(a)
313	29	2828	127.6	-0.013	90	0.21	0.3	0.15	-58	0.17	-	-	(a)
314	29	2825	129.7	-0.006	90	0.20	0.3	0.18	-58	0.15	-	-	(a)
315	29	2827	129.2	0.002	90	0.20	0.3	0.17	-58	0.17	-	-	(a)
316	29	2826	128.5	0.008	90	0.20	0.3	0.17	-58	0.15	-	-	(a)
317	29	2826	129.6	0.34	90	0.46	0.3	0.42	-58	0.32	-	-	395(b)
318	29	2826	128.2	0.98	90	0.66	0.3	0.51	-58	0.48	1	20	651(c)
319	29	2826	129.4	1.47	90	0.30	0.3	0.14	-58	0.26	-	-	957(c)
320	29	2826	130.0	1.86	90	0.13	0.3	0.08	-58	0.10	-	-	(a)
321	30	2827	129.4	1.96	200	0.13	0.3	0.08	-58	0.10	-	-	(a)
322	30	2826	129.6	1.20	200	0.33	0.3	0.17	-58	0.29	2	24	866(c)
323	30	2827	129.2	1.00	200	0.69	0.3	0.60	-58	0.44	1	-	618(c)

TABLE III (cont.)

FLUTTER DATA FOR SHELL NO. 3 ($h = 0.0040$ INCHES AND $M_\infty = 2.993$)

Corr. No.	Run No.	p_{t_∞} (psfa)	T_{t_∞} (^oF)	p_m (psig)	P_x (lb)	$\frac{w_{rms}^1}{h}$	$\frac{x}{L}$	$\frac{w_{rms}^2}{h}$	θ (deg)	$\frac{w_{rms}^3}{h}$	j	n	f (cps)
324	30	2828	129.6	0.43	200	0.53	0.3	0.42	-58	0.39	-	-	503(c)
325	30	2826	128.9	0.18	200	0.18	0.3	0.17	-58	0.14	-	-	(a)
326	31	2474	123.8	-0.013	90	0.20	0.3	0.15	-58	0.14	-	-	(a)
327	31	2476	123.1	-0.018	90	0.20	0.3	0.15	-58	0.14	-	-	(a)
328	31	2474	121.6	-0.023	90	0.20	0.3	0.17	-58	0.14	-	-	(a)
329	31	2474	121.9	-0.026	90	0.21	0.3	0.11	-58	0.12	-	-	(a)
330	31	2475	122.6	-0.029	90	0.18	0.3	0.11	-58	0.14	-	-	(a)
331	31	2474	122.2	-0.032	90	0.21	0.3	0.18	-58	0.15	-	-	(a)
332	31	2474	121.3	-0.037	90	0.25	0.3	0.21	-58	0.18	-	-	(a)
Shallow longitudinal buckles appeared here.													
333	32	2475	121.3	-0.001	200	0.17	0.3	0.12	-58	0.22	-	-	(a)
334	32	2475	120.2	-0.003	200	0.17	0.3	0.14	-58	0.25	-	-	(a)
335	32	2475	120.2	-0.006	200	0.12	0.3	0.14	-58	0.28	-	-	(a)

TABLE III (cont.)

FLUTTER DATA FOR SHELL NO. 3 (h = 0.0040 INCHES AND M_∞ = 2.993)

Corr. No.	Run No.	p_{t_∞} (psfa)	T_{t_∞} (^oF)	p_m (psig)	P_x (lb)	$\frac{w_{rms}^1}{h}$	$\frac{x}{L}$	$\frac{w_{rms}^2}{h}$	θ (deg)	$\frac{w_{rms}^3}{h}$	j	n	f (cps)
336	32	2473	121.4	-0.010	200	0.17	0.3	0.14	-58	0.28	-	-	(a)
Shallow diamond pattern buckles appeared here.													
336A	32	2473	121.4	0.015	200	0.82	0.3	0.15	-58	0.18	-	-	(d)
337	32	2473	122.8	0.49	200	0.13	0.3	0.09	-58	0.10	-	-	(a)
338	33	2474	121.7	0.49	240	0.13	0.3	0.08	-58	0.10	-	-	(a)
339	34	2475	119.8	0.27	240	0.13	0.3	0.09	-58	0.12	-	-	(a)
Complete buckling occurred here at p_m = 0.098 psig. Buckling pattern is shown in figures 8 and 9.													

TABLE IV

TEST CONDITIONS FOR STATIC PRESSURE TEST

Correlation Number	M_∞	p_{t_∞} (psf)	p_∞ (psf)	T_t (^oF)	p_∞ (psf)
1	3.400	2449		125.4	40.2
2	"	2444	299.1	126.3	40.2
3	"	2040	249.7	117.3	34.6
4	"	1631	199.6	108.6	29.1
5	3.003	2039	348.9	120.1	58.3
6	"	1747	298.9	114.4	50.8
7	"	1459	249.6	106.1	43.3
9	2.605	1583	374.2	109.6	85.1
10	"	1255	296.7	102.8	68.7
11	"	1898	448.7	117.5	101.5

TABLE V

FOUR MODE-PISTON THEORY RESULTS, $P_x = p_m = 0$

n	p_∞ (psia)	ω (rad/sec)	$\lvert c_2 \rvert^*$	ϕ_2^* (deg)	$\lvert c_3 \rvert$	ϕ_3 (deg)	$\lvert c_4 \rvert$	ϕ_4 (deg)
23	0.5944	1468.67	1.0618	161.63	0.3690	-22.87	0.0935	162.47
24	0.5769	1588.85	1.0709	160.38	0.3982	-24.81	0.1081	160.43
25	0.5729	1716.07	1.0822	159.15	0.4328	-26.85	0.1273	158.17
26	0.5804	1849.89	1.0952	157.98	0.4718	-28.93	0.1519	155.72
27	0.5972	1989.92	1.1089	156.86	0.5126	-31.03	0.1819	153.13

* The modal amplitudes $\lvert c_m \rvert$ and phases ϕ_m are normalized by taking $c_1 = 1$.

TABLE VI

SIX MODE - PISTON THEORY RESULTS, $P_x = p_m = 0$

n	p_∞ (psia)	ω (rad/sec)	$\lvert c_2 \rvert^*$	ϕ_2^* (deg)	$\lvert c_3 \rvert$	ϕ_3 (deg)
23	0.6131	1470.53	1.0679	161.76	0.3846	-22.92
24	0.6006	1591.12	1.0802	160.59	0.4209	-24.86
25	0.6052	1719.09	1.0972	159.53	0.4678	-26.84
26	0.6274	1854.26	1.1207	158.69	0.5284	-28.80

n	$\lvert c_4 \rvert$	ϕ_4 (deg)	$\lvert c_5 \rvert$	ϕ_5 (deg)	$\lvert c_6 \rvert$	ϕ_6 (deg)
23	0.0917	162.39	0.0340	-18.87	0.0133	164.99
24	0.1074	160.26	0.0384	-20.45	0.0158	163.14
25	0.1295	157.85	0.0464	-22.16	0.0195	161.09
26	0.1610	155.20	0.0582	-24.02	0.0252	158.84

* See note under Table V

TABLE VII

SIX MODE - POTENTIAL THEORY RESULTS, $P_x = p_m = 0$

n	p_∞ (psia)	ω (rad/sec)	$\lvert c_2 \rvert^*$	ϕ_2^* (deg)	$\lvert c_3 \rvert$	ϕ_3 (deg)
17	1.8836	705.98	0.3145	91.94	0.0424	-150.86
18	1.9951	802.87	0.2537	90.22	0.0456	-172.34
19	1.9314	914.16	0.2847	95.65	0.0762	-157.38
20	1.6109	1058.16	2.9031	102.88	3.1632	-160.42
21	1.6444	1152.51	0.5290	92.49	0.2997	-172.92

n	$\lvert c_4 \rvert$	ϕ_4 (deg)	$\lvert c_5 \rvert$	ϕ_5 (deg)	$\lvert c_6 \rvert$	ϕ_6 (deg)
17	0.0015	90.31	0.0011	-21.12	0.0002	-179.00
18	0.0011	24.03	0.0007	-11.11	0.0002	-119.54
19	0.0050	77.28	0.0016	-74.61	0.0004	151.20
20	0.3856	20.15	0.0876	-160.74	0.0310	64.54
21	0.0257	-21.75	0.0028	-160.50	0.0017	68.48

* See note under Table V

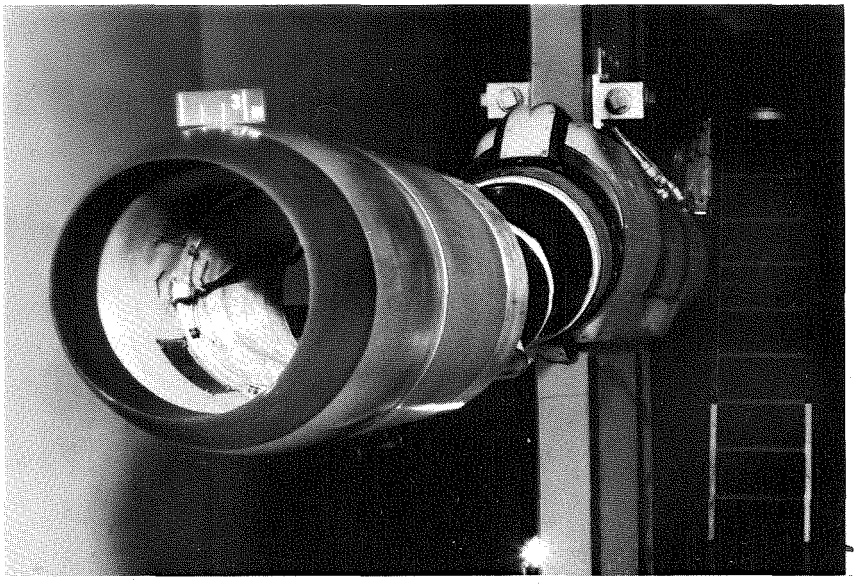

Figure 1: Front View of Cylindrical Panel Flutter Model in Tunnel

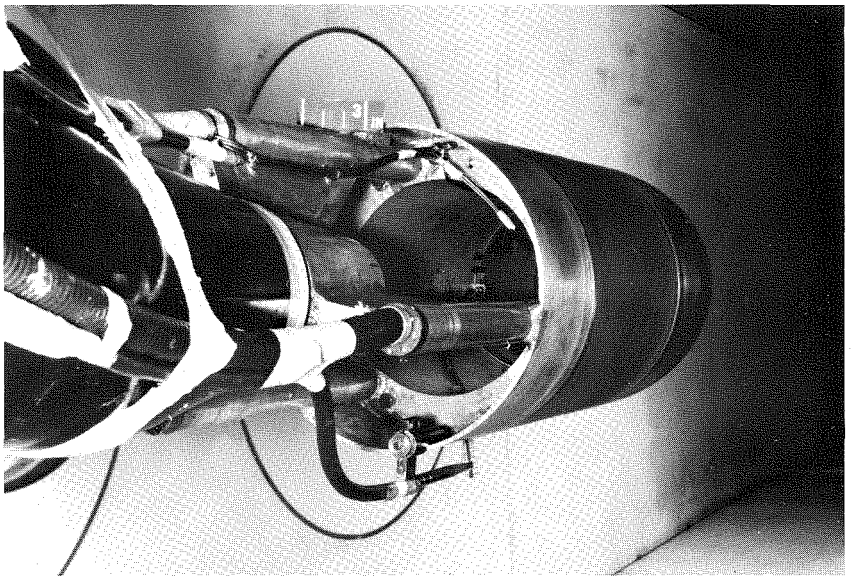

Figure 2: Back View of Cylindrical Panel Flutter Model in Tunnel

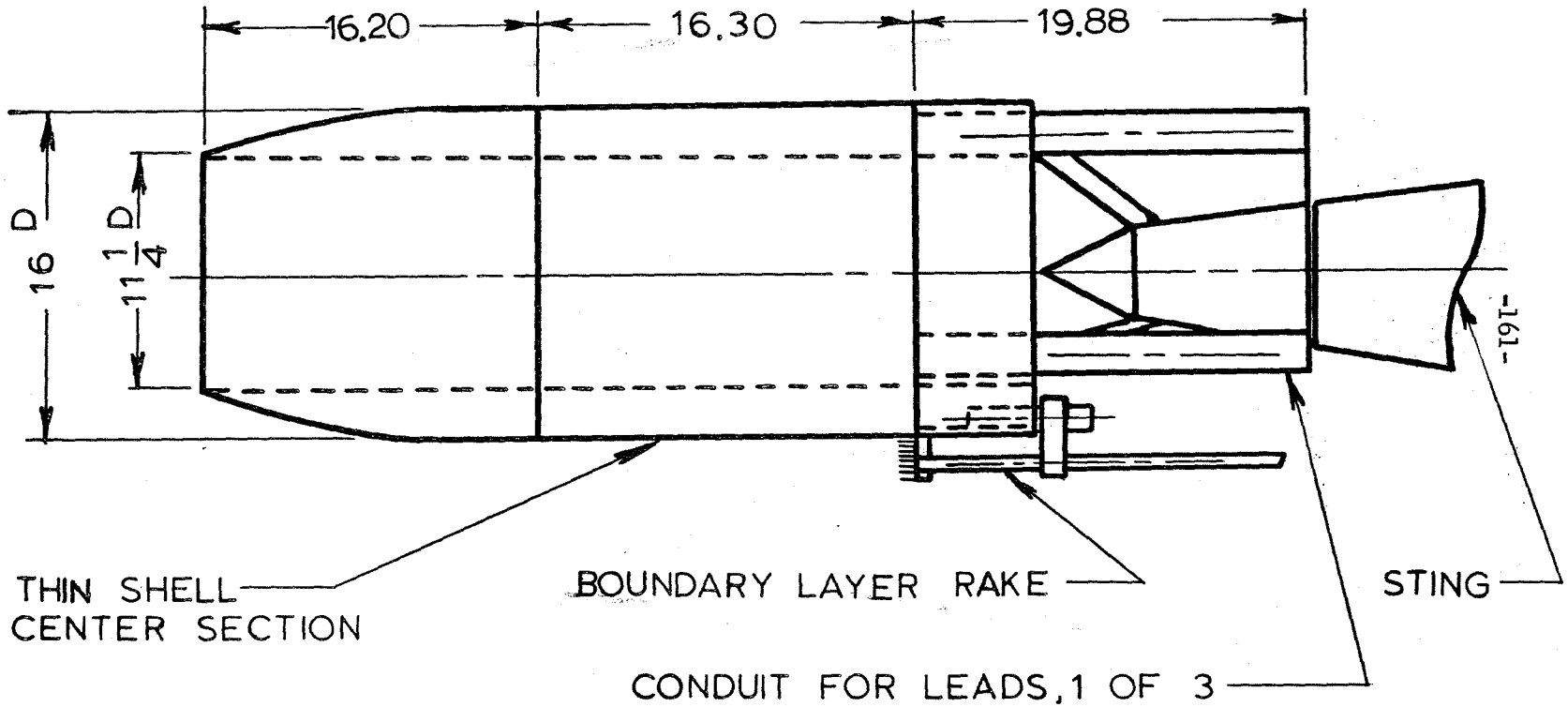

FIG. 3 CYLINDRICAL FLUTTER MODEL

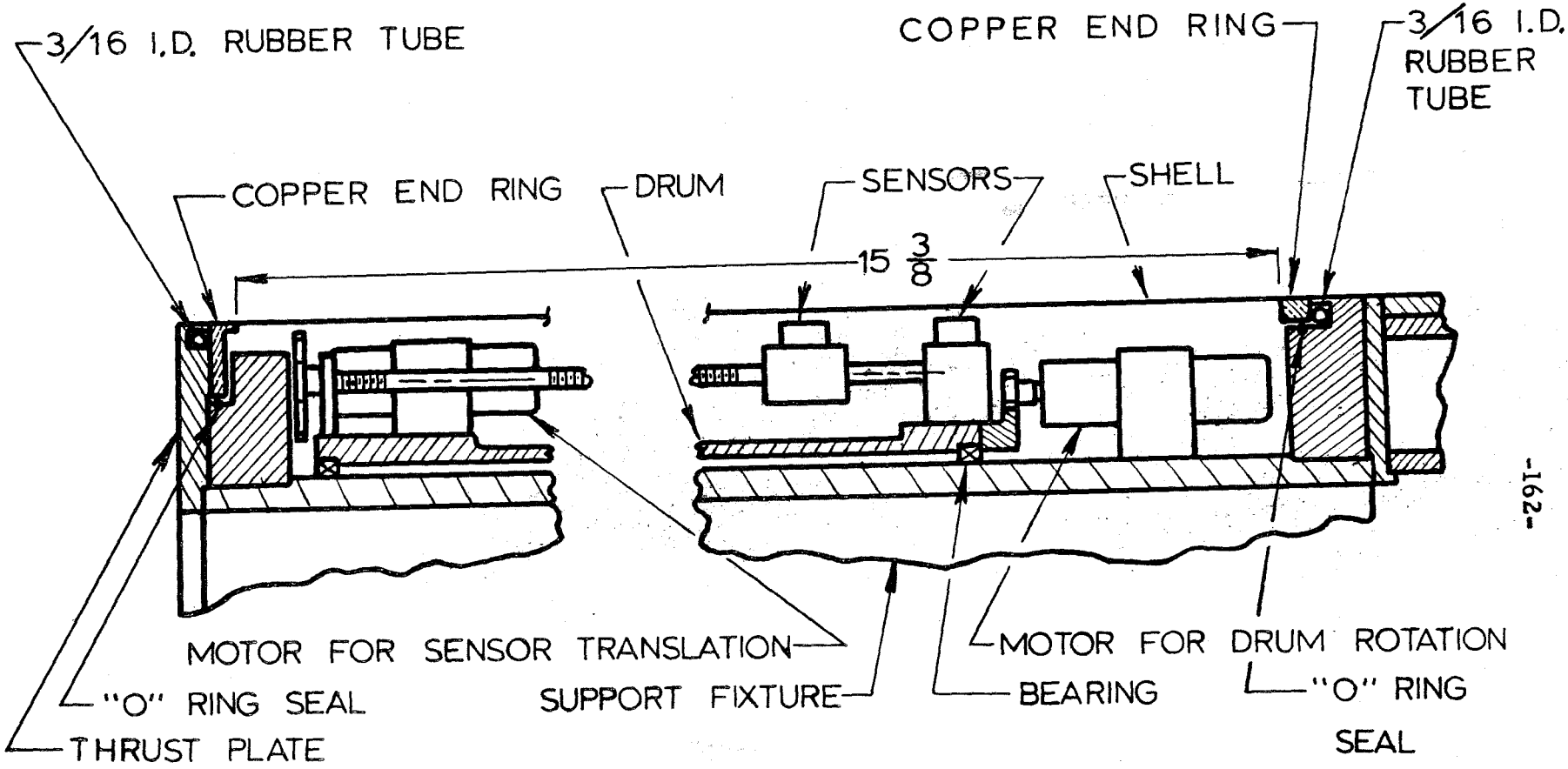

FIG. 4 INSTRUMENTATION AND SHELL MOUNTING DETAILS

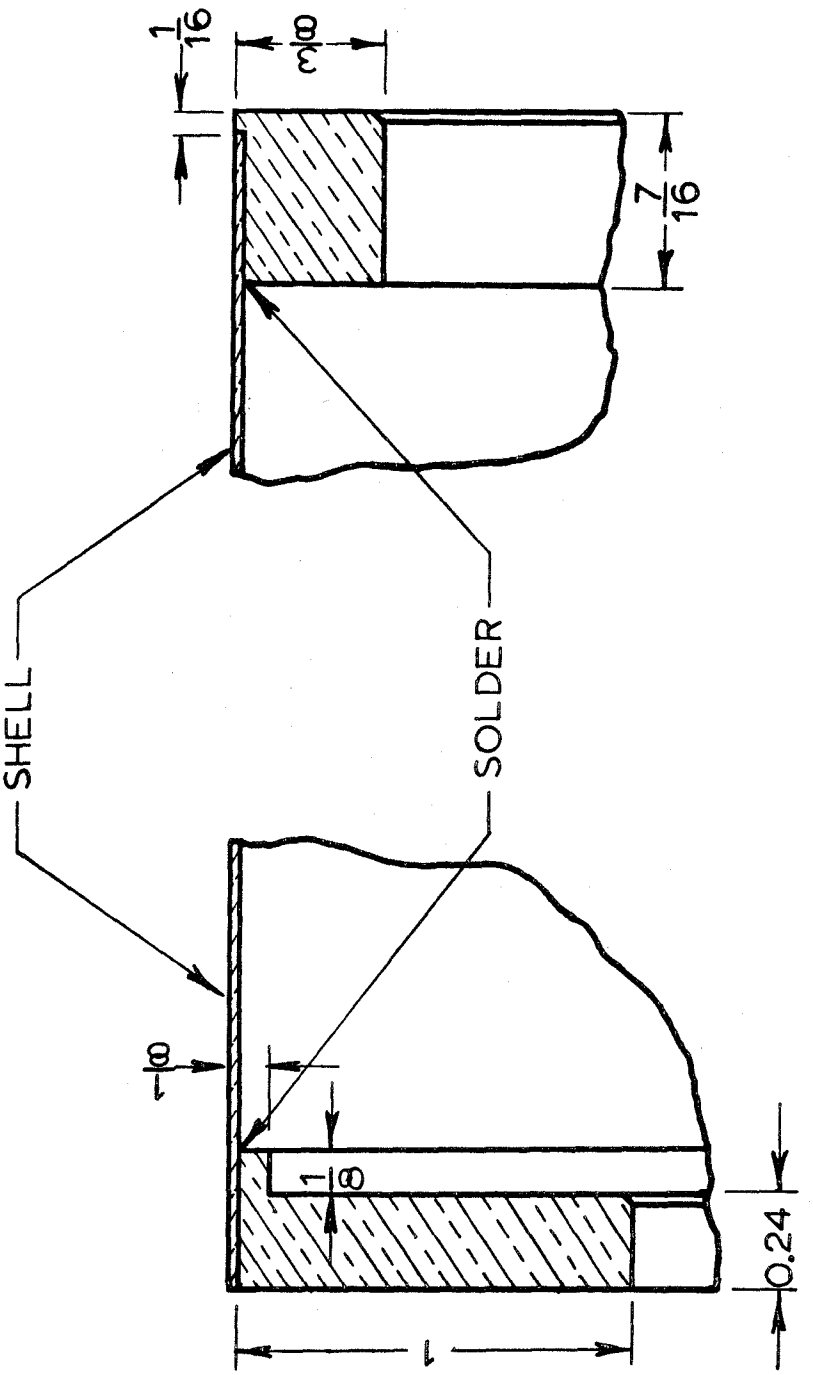

FIG. 5 END RING DETAILS

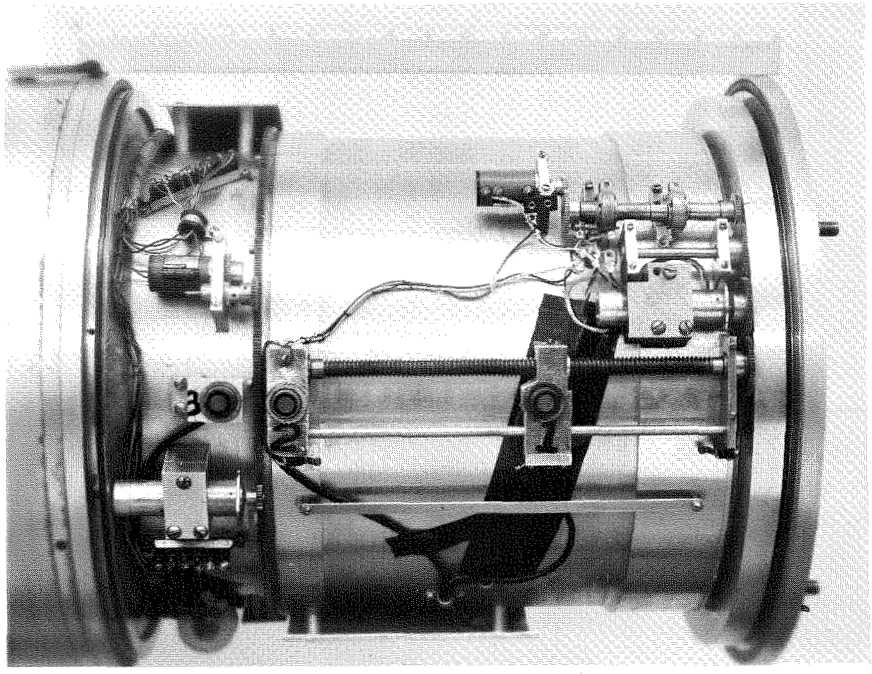

Figure 6: View of Model Instrumentation

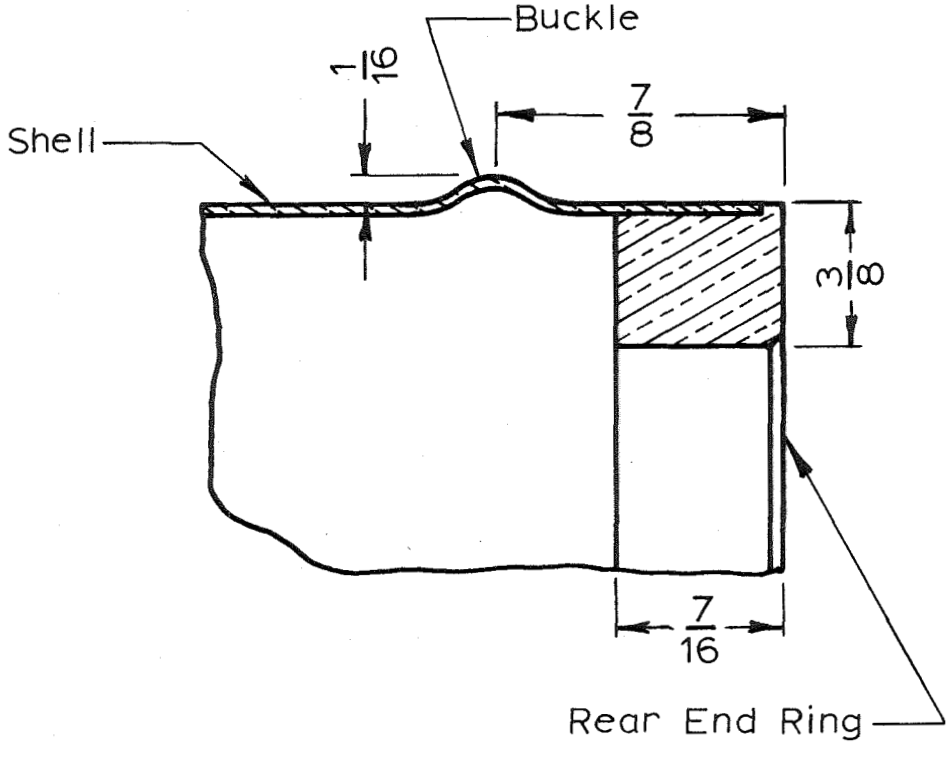

FIG. 7 CROSS SECTION OF BELLOWS BUCKLE (h=0.0039")

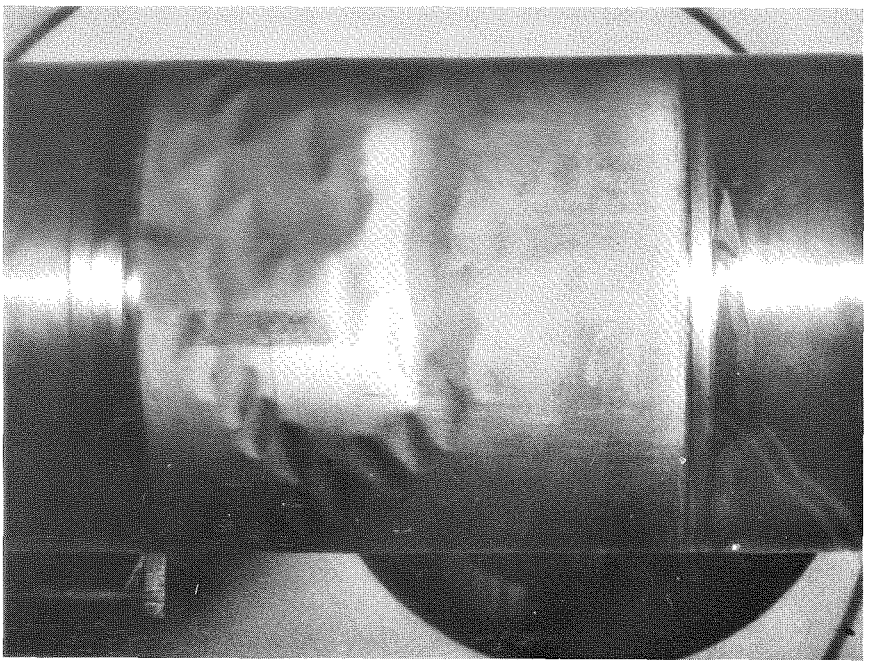

Figure 8: Right Hand Side of Buckled Shell; Run No. 34

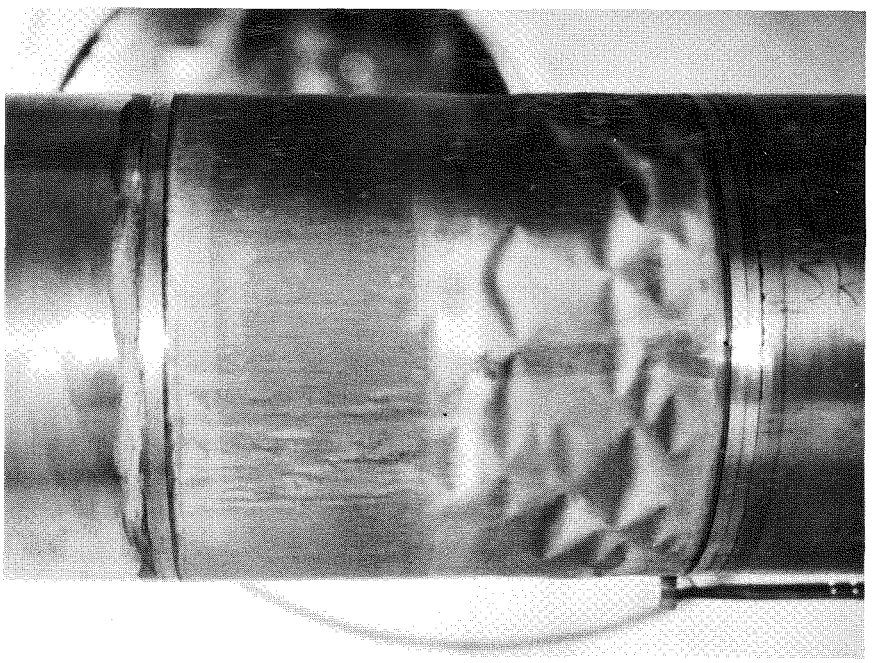

Figure 9: Left Hand Side of Buckled Shell; Run No. 34

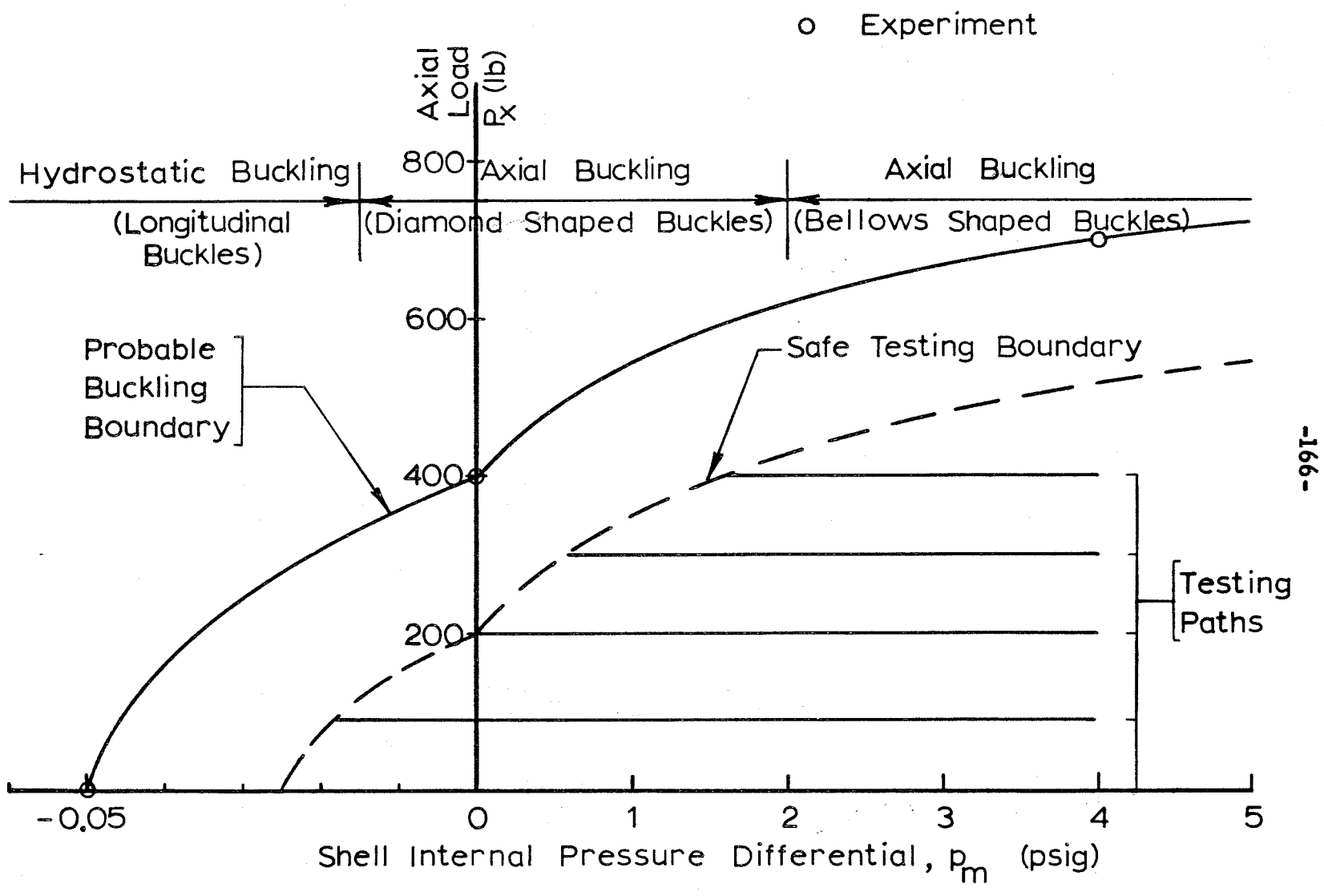

FIG. 10 EXPECTED BUCKLING CHARACTERISTICS OF THIN SHELLS(h=0.0040")

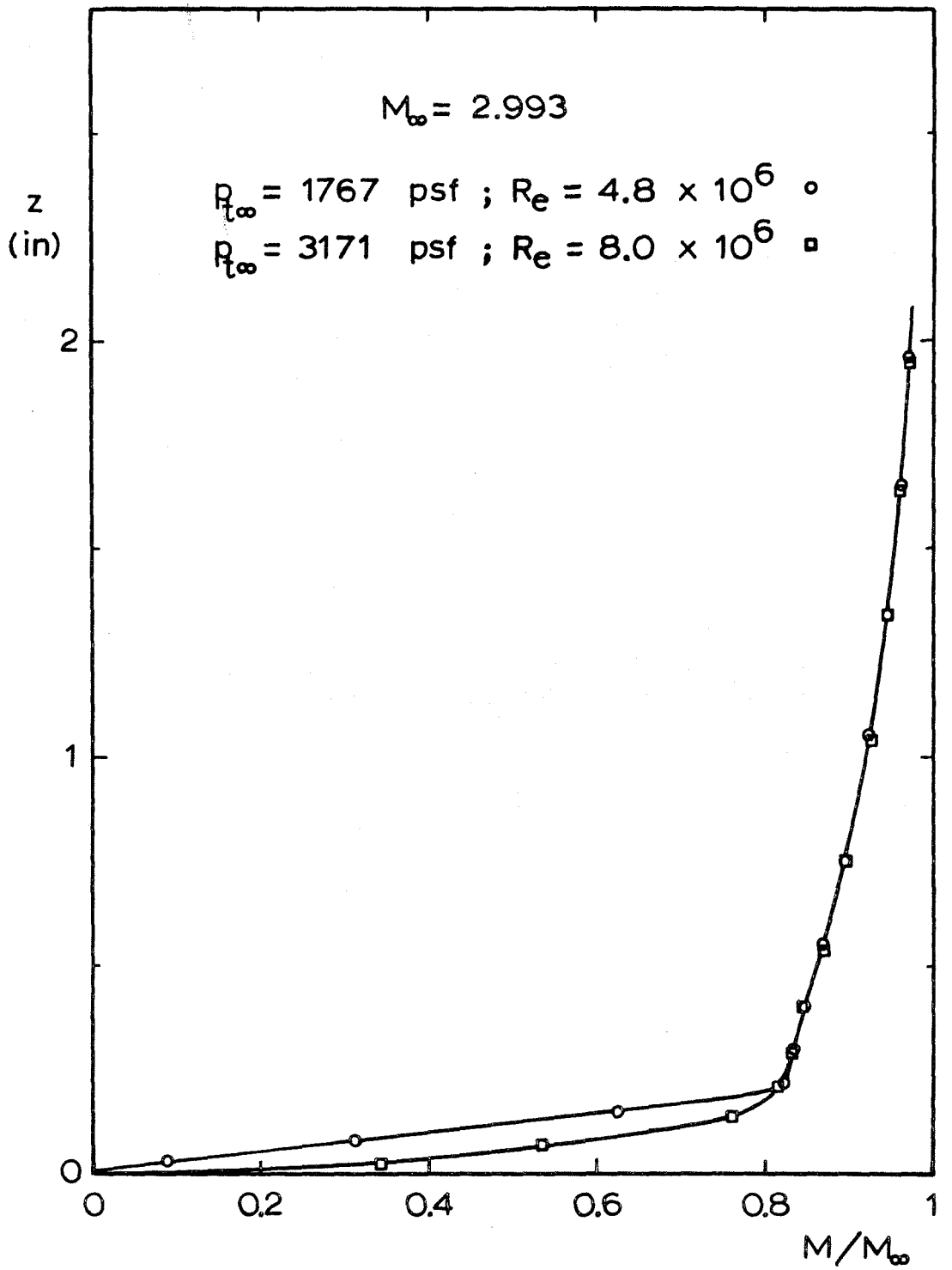

FIG. 11 BOUNDARY LAYER PROFILES

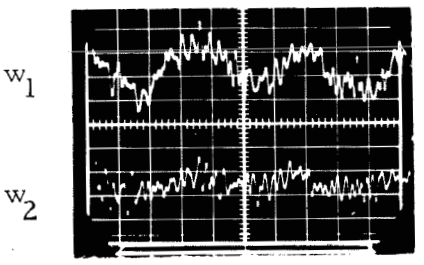

(a)

Corr. No. 299

5 msec/div.

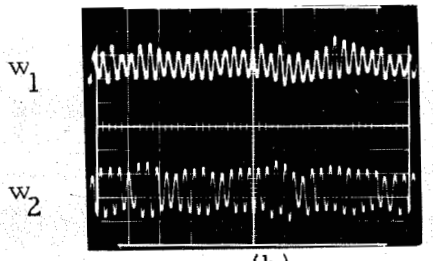

(b)

Corr. No. 113

5 msec/div.

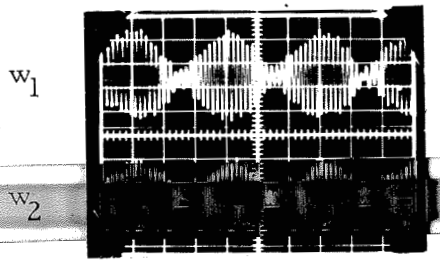

(c)

Corr. No. 209

10 msec/div.

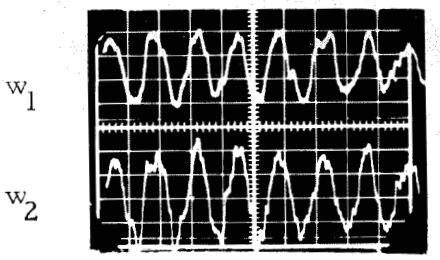

(d)

Corr. No. 310

10 msec/div.

Figure 12: Sample Time Traces of Shell Motion

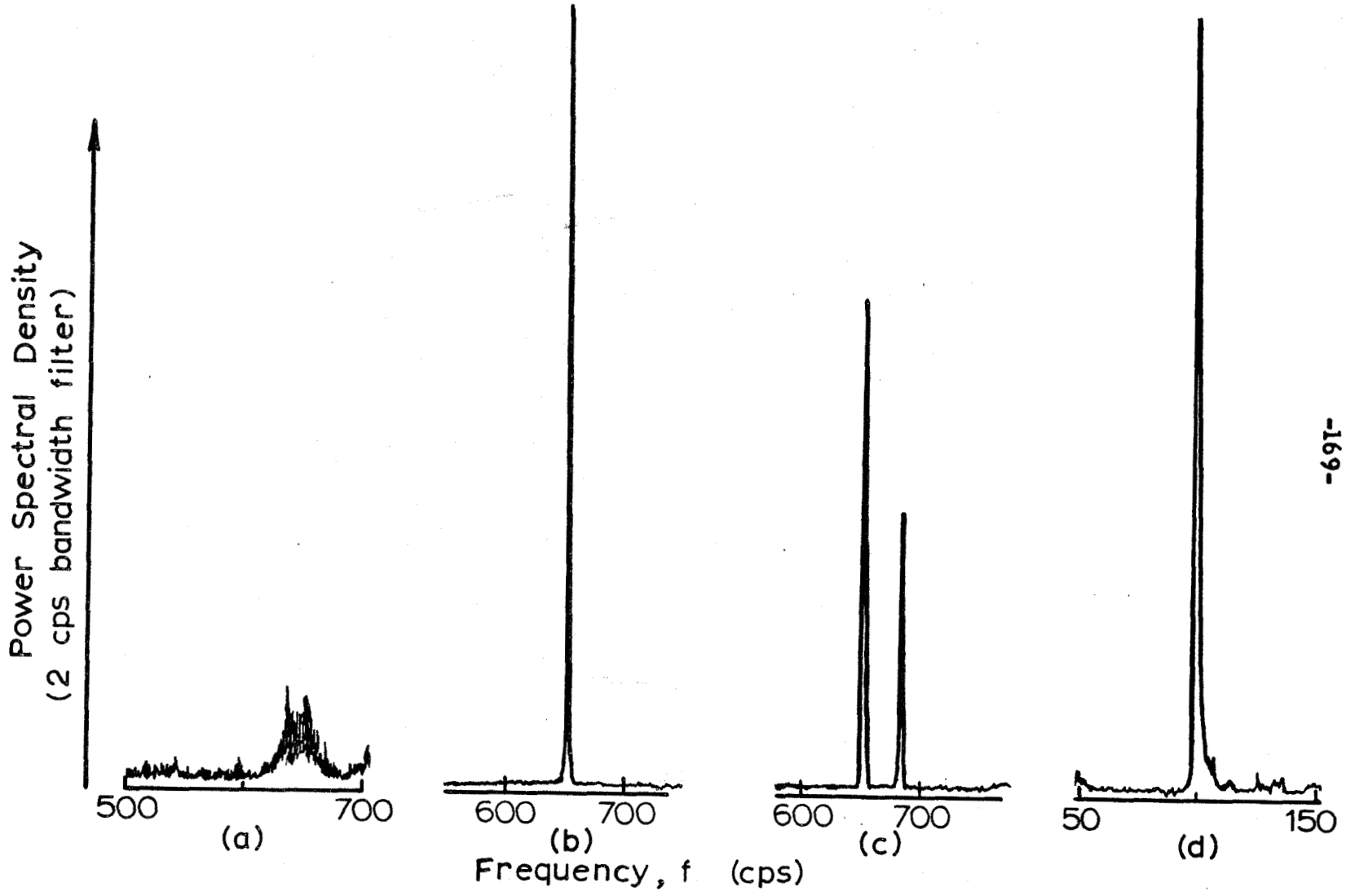

FIG. 13 POWER SPECTRA OF SIGNALS SHOWN IN FIG. 12

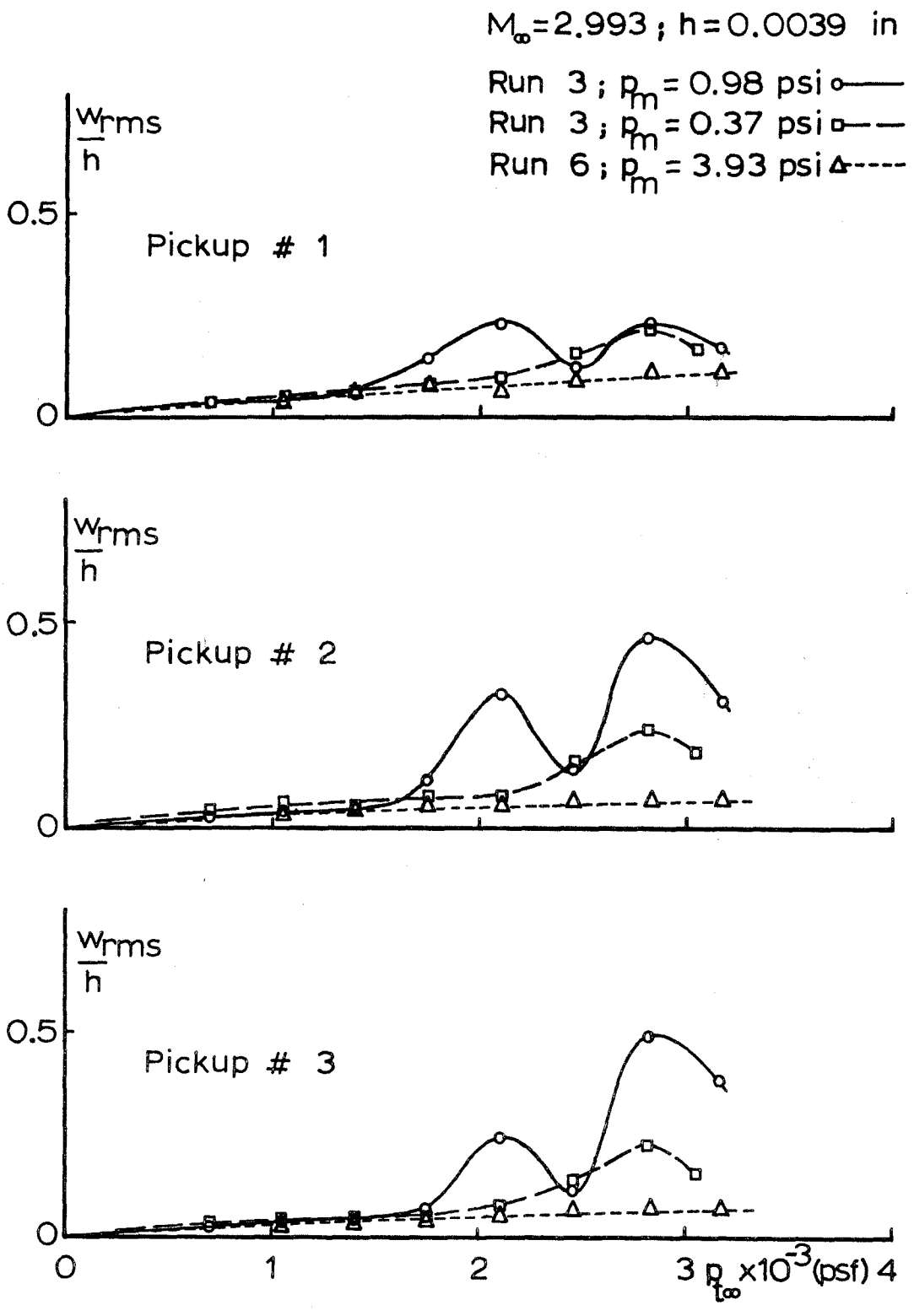

FIG. 14 FLUTTER AMPLITUDE VS. TOTAL PRESSURE

$R_x = 0$; Corr. #'s 157 - 179
$M_\infty = 2.993$; h = 0.0039 in

$p_{t\infty}$ = 2111 psf
$p_{t\infty}$ = 2466 psf
$p_{t\infty}$ = 2818 psf

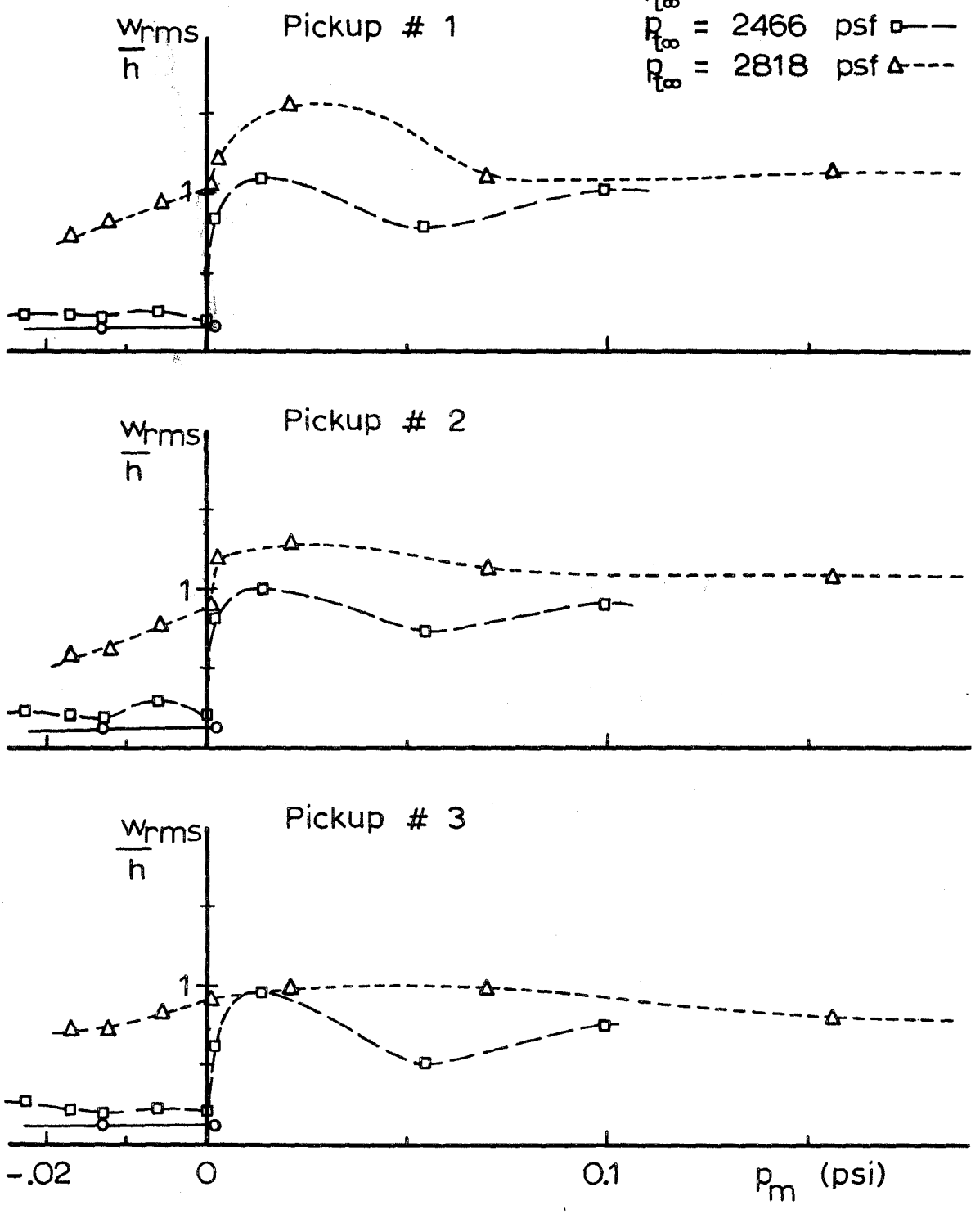

FIG. 15 FLUTTER AMPLITUDE VS. INTERNAL PRESSURE FOR BUCKLED (BELLOWS MODE) SHELL

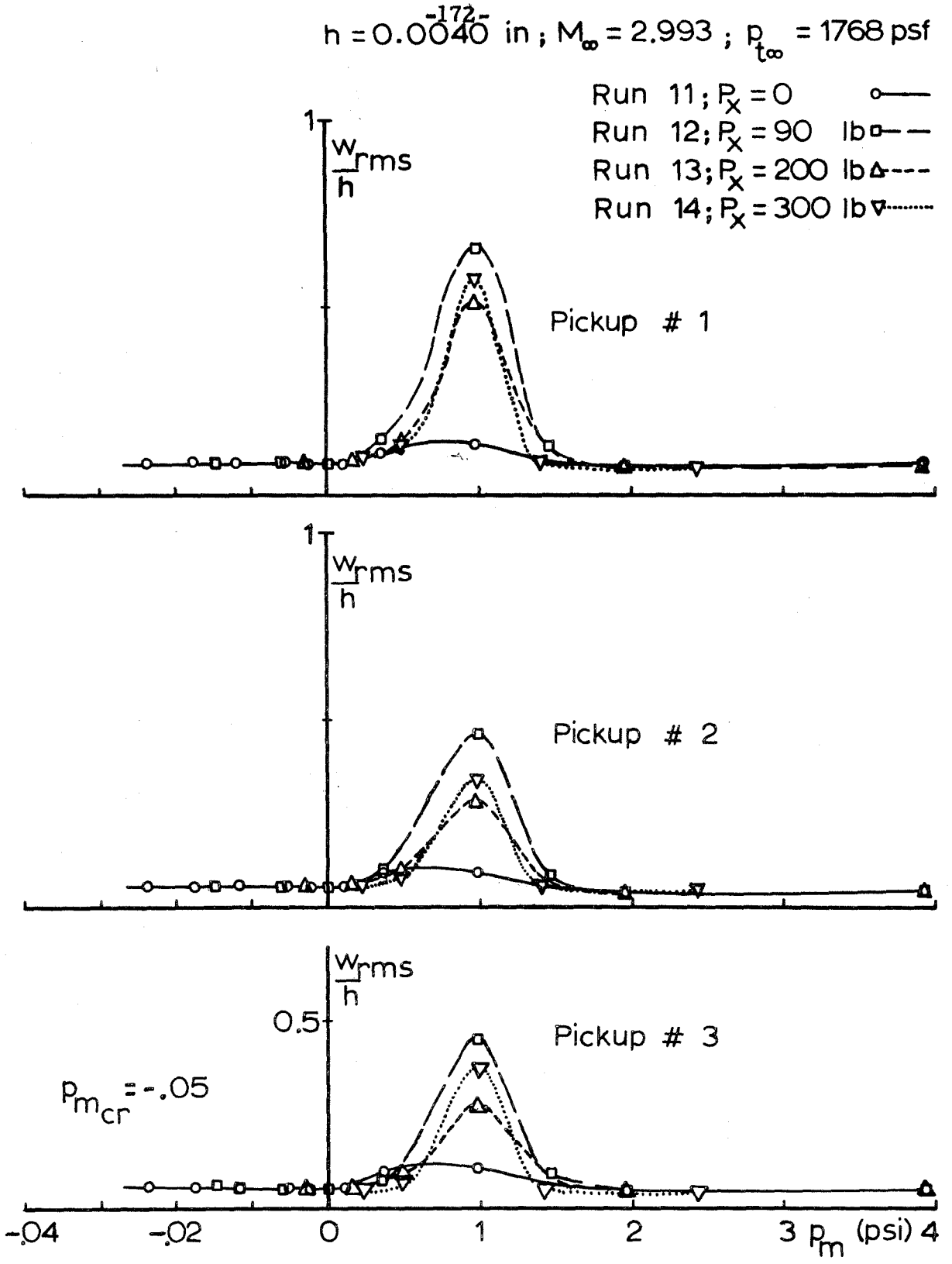

FIG. 16 FLUTTER AMPLITUDE VS. INTERNAL PRESSURE WITH VARIOUS AXIAL LOADS; CORR. #'s 187 TO 217

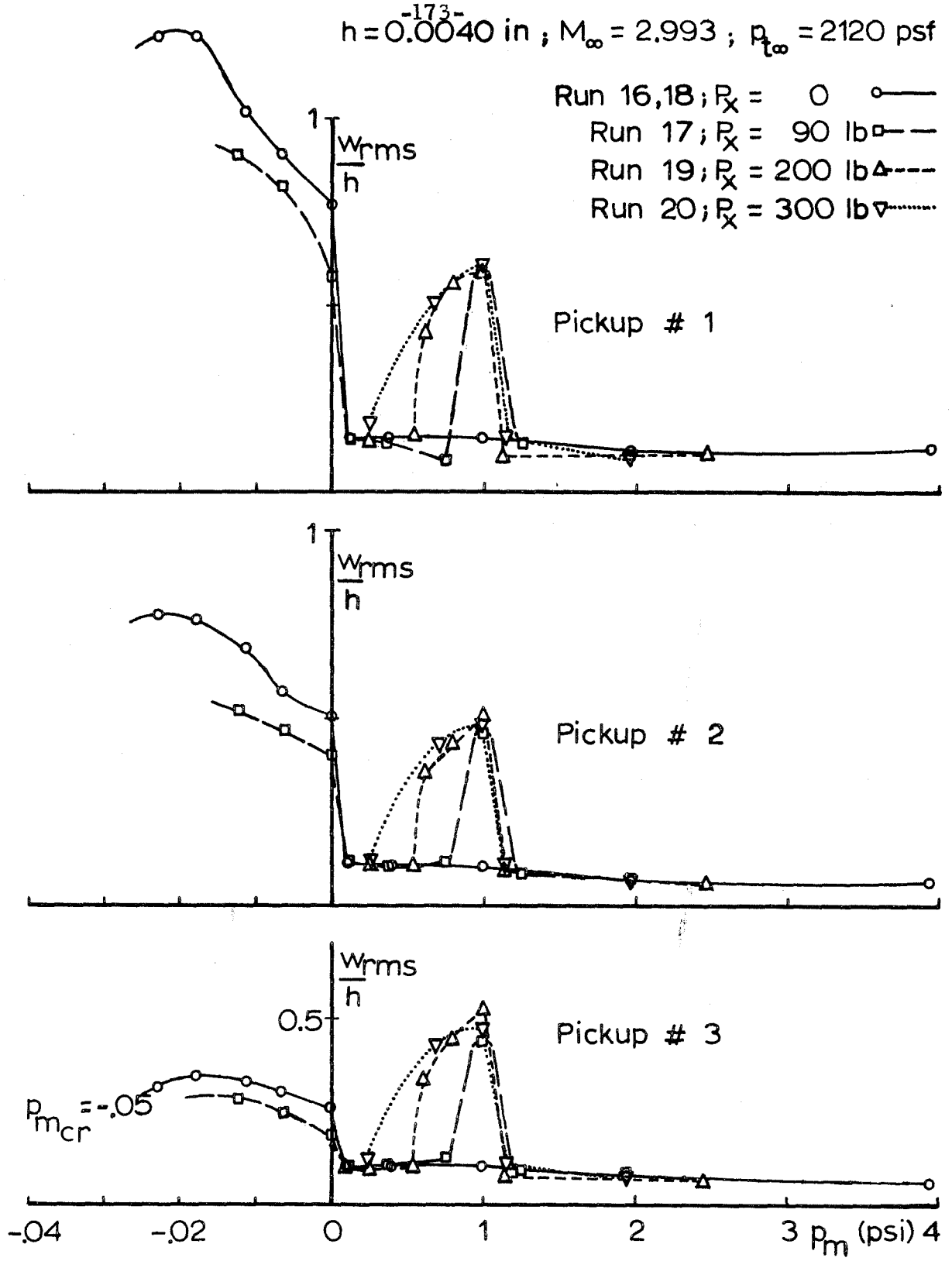

FIG. 17 FLUTTER AMPLITUDE VS. INTERNAL PRESSURE WITH VARIOUS AXIAL LOADS; CORR. #'s 228 TO 260

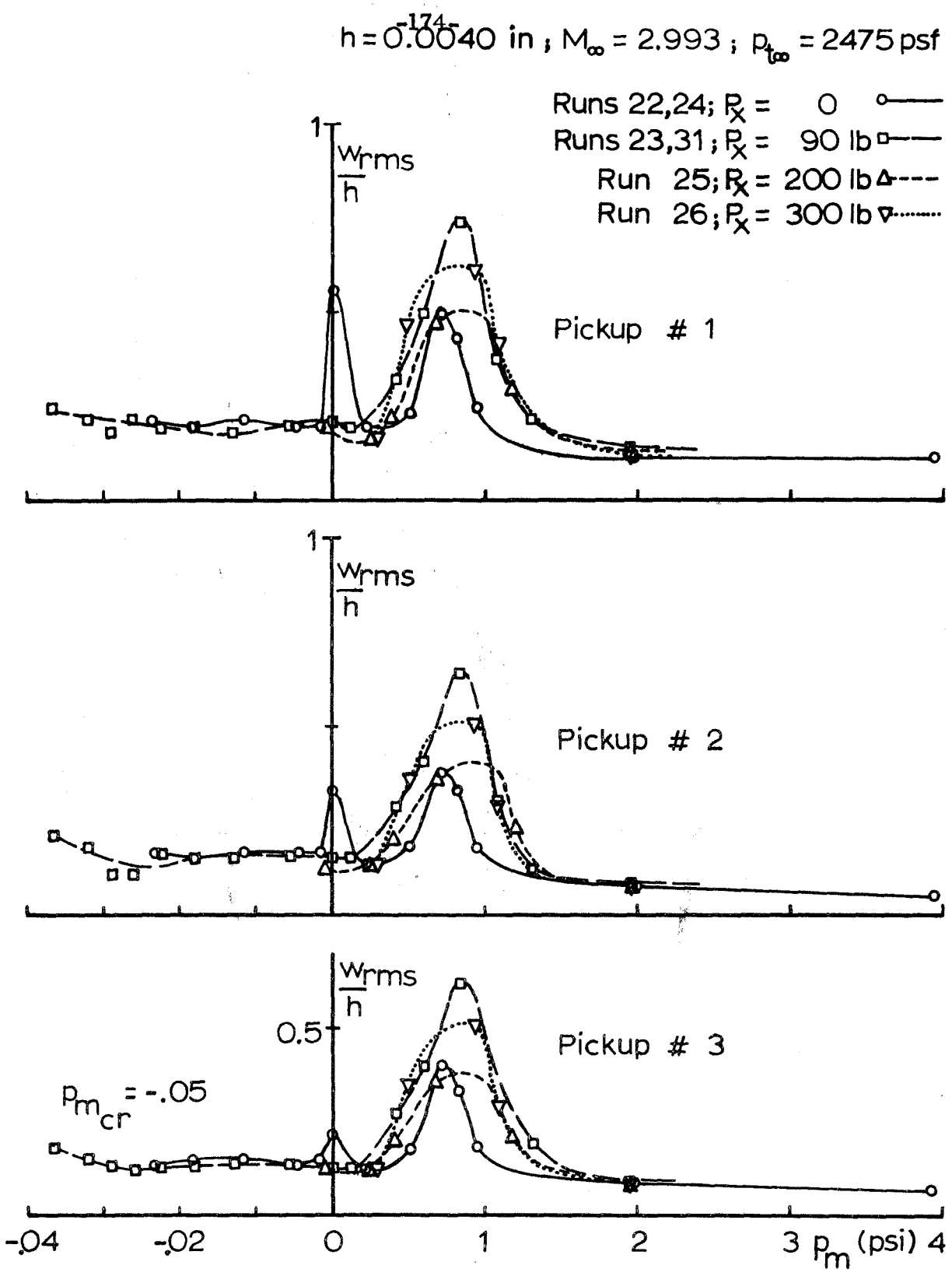

FIG. 18 FLUTTER AMPLITUDE VS. INTERNAL PRESSURE WITH VARIOUS AXIAL LOADS; CORR. #'s 263-296 & 326-332

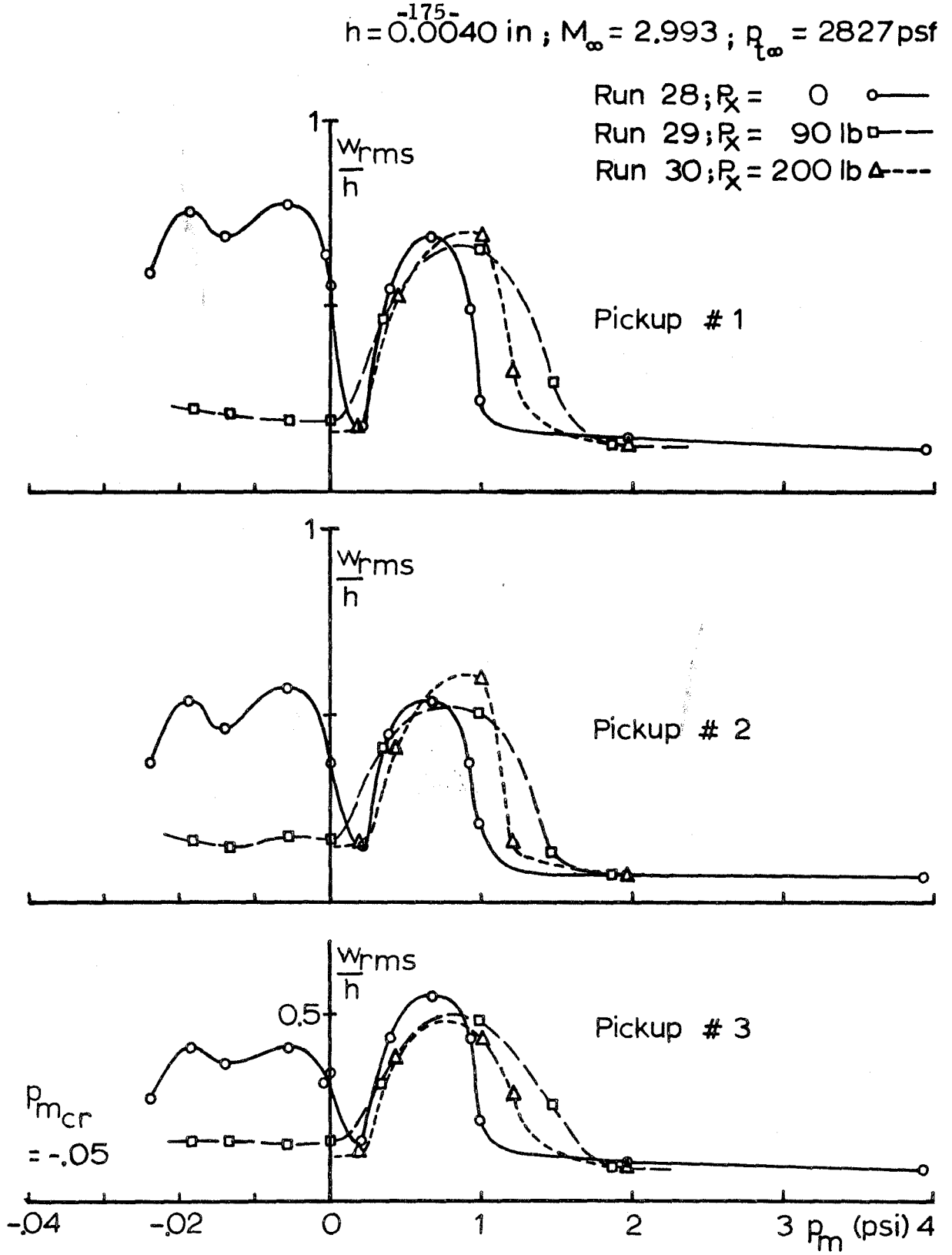

FIG. 19 FLUTTER AMPLITUDE VS. INTERNAL PRESSURE WITH VARIOUS AXIAL LOADS; CORR. #'s 299 TO 325

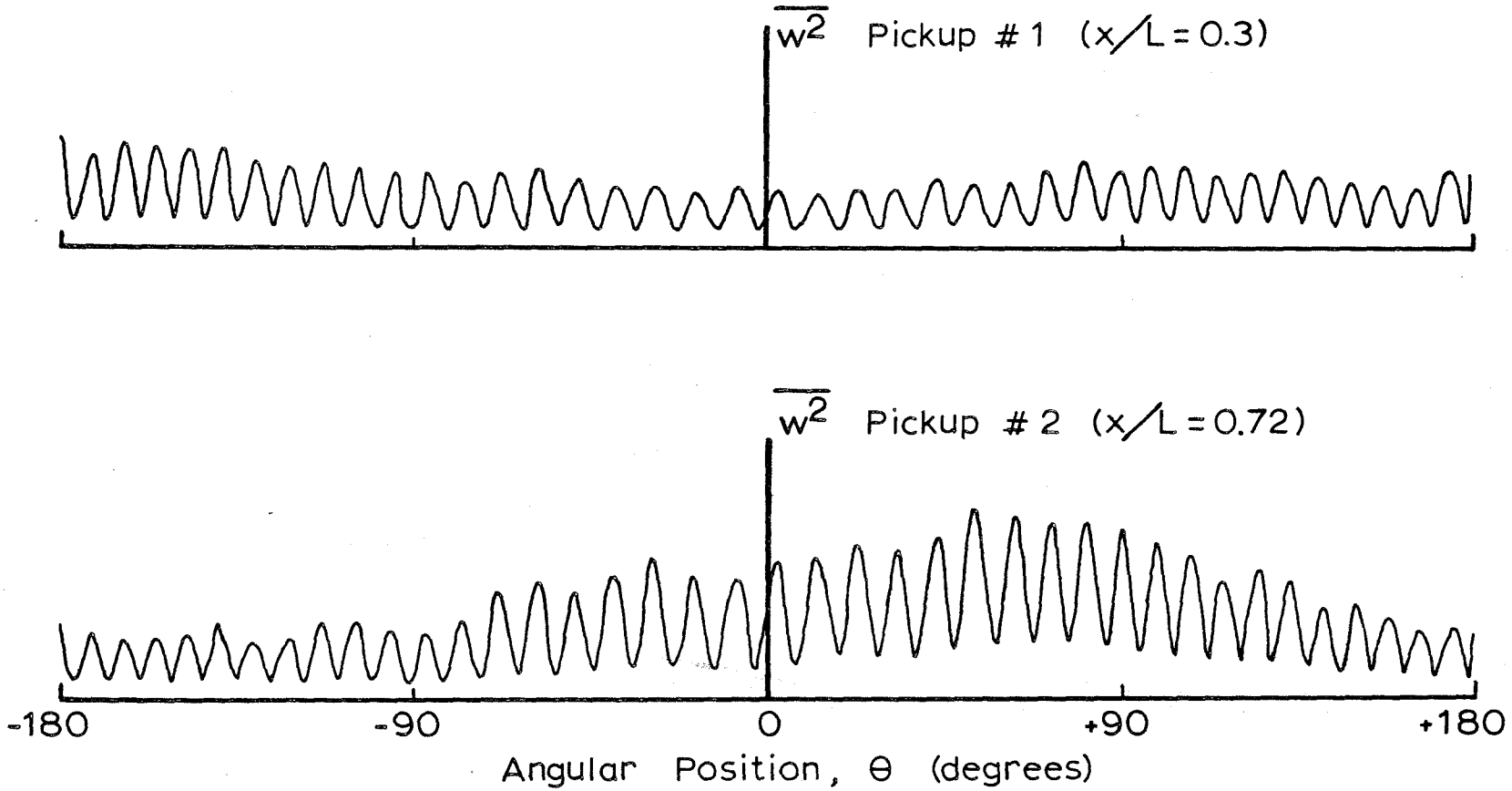

FIG. 20 CIRCUMFERENTIAL TRAVERSE; CORR. # 112

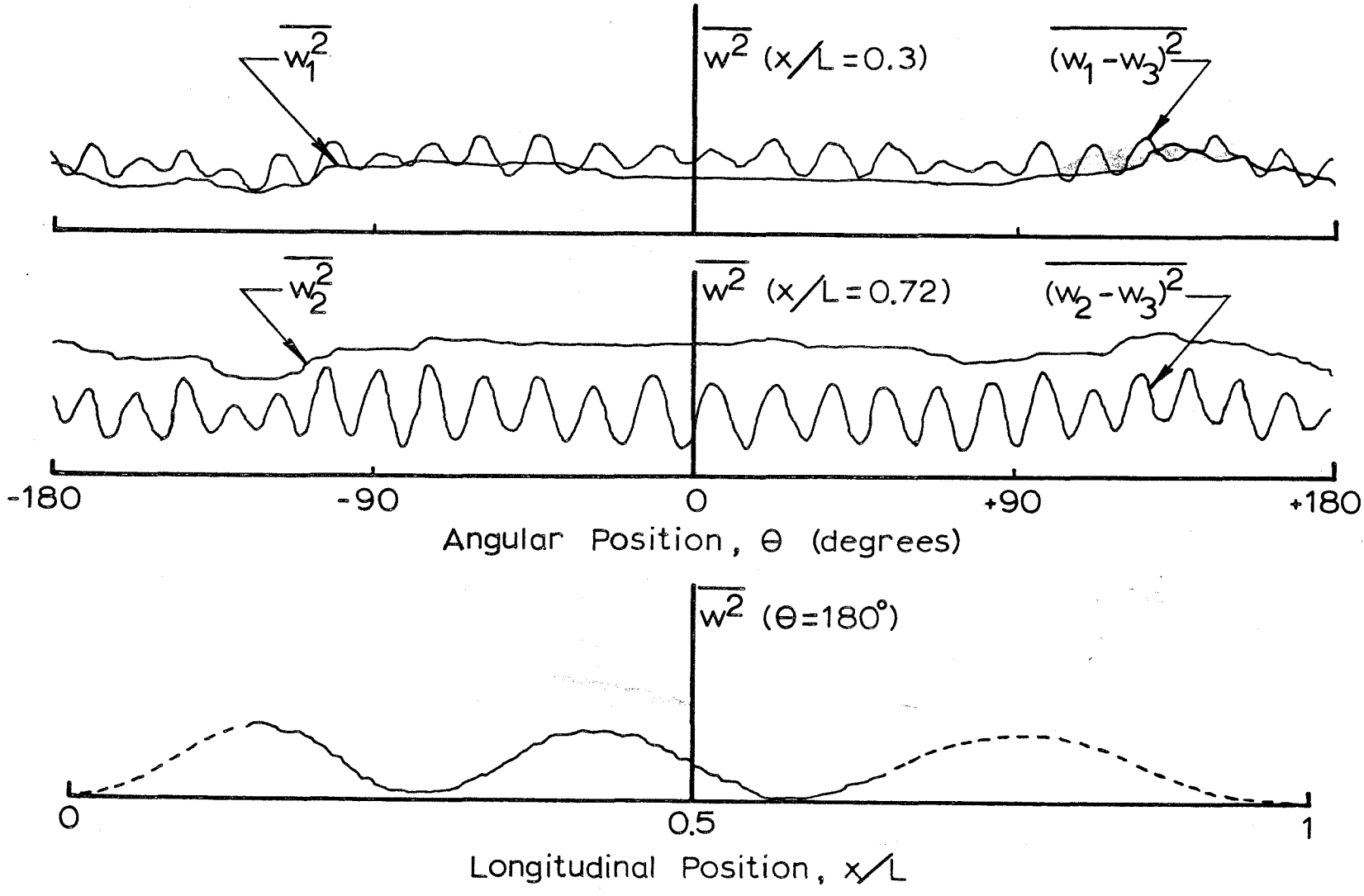

FIG. 21 LONGITUDINAL AND CIRCUMFERENTIAL TRAVERSES; CORR. # 126

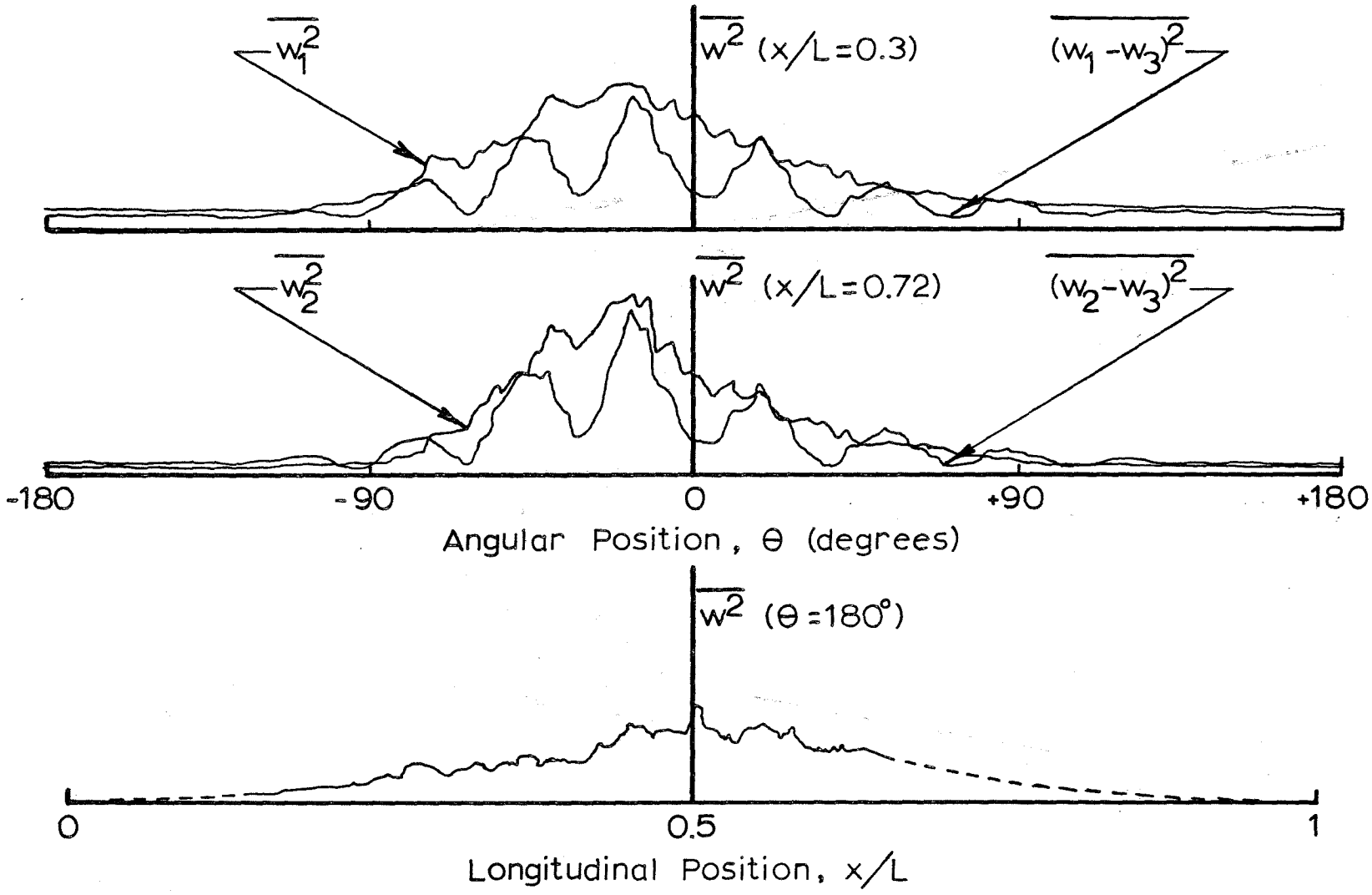

FIG. 22 LONGITUDINAL AND CIRCUMFERENTIAL TRAVERSES; CORR. # 162

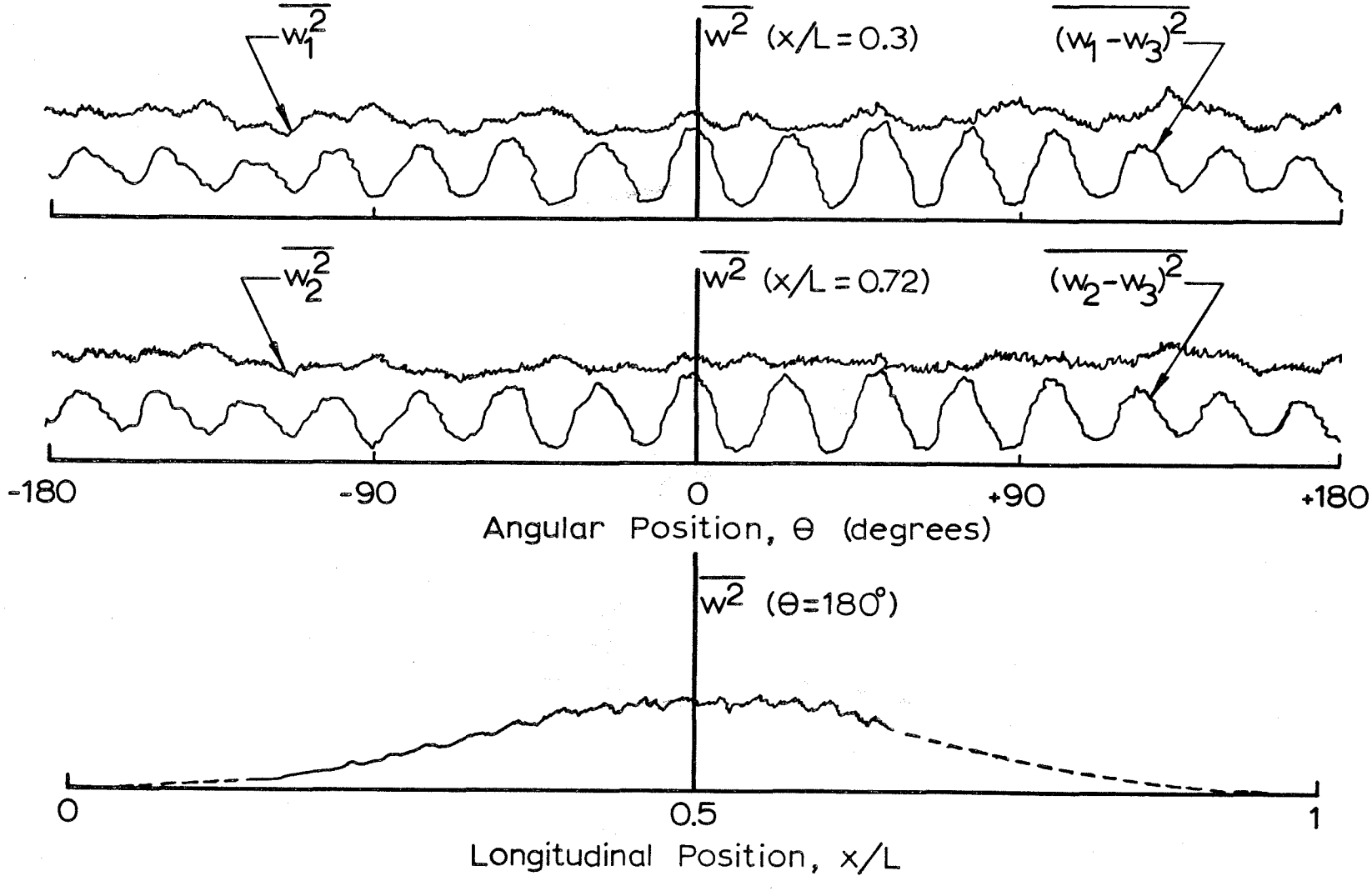

FIG. 23 LONGITUDINAL AND CIRCUMFERENTIAL TRAVERSES; CORR. # 174

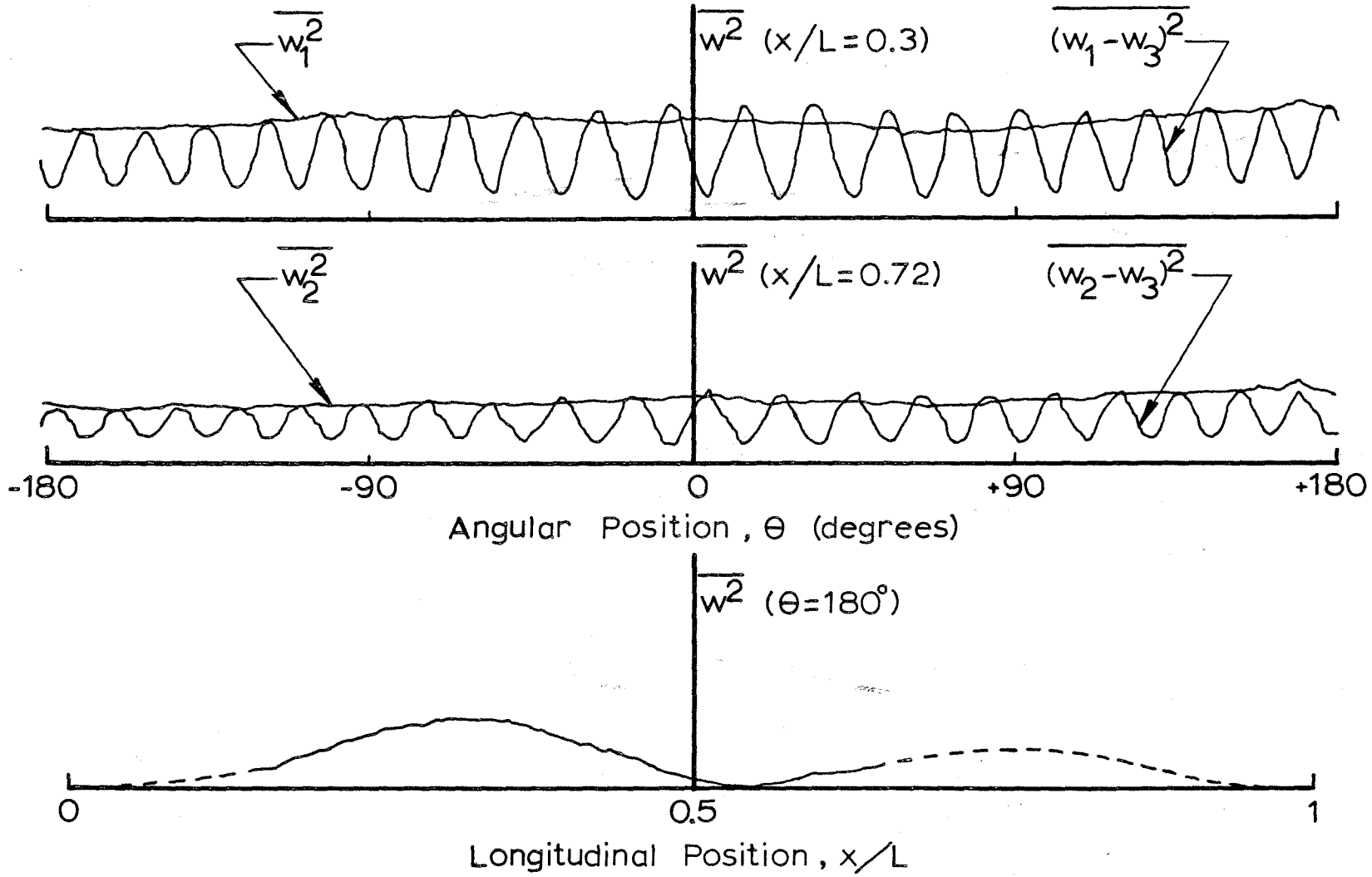

FIG. 24 LONGITUDINAL AND CIRCUMFERENTIAL TRAVERSES; CORR. #203

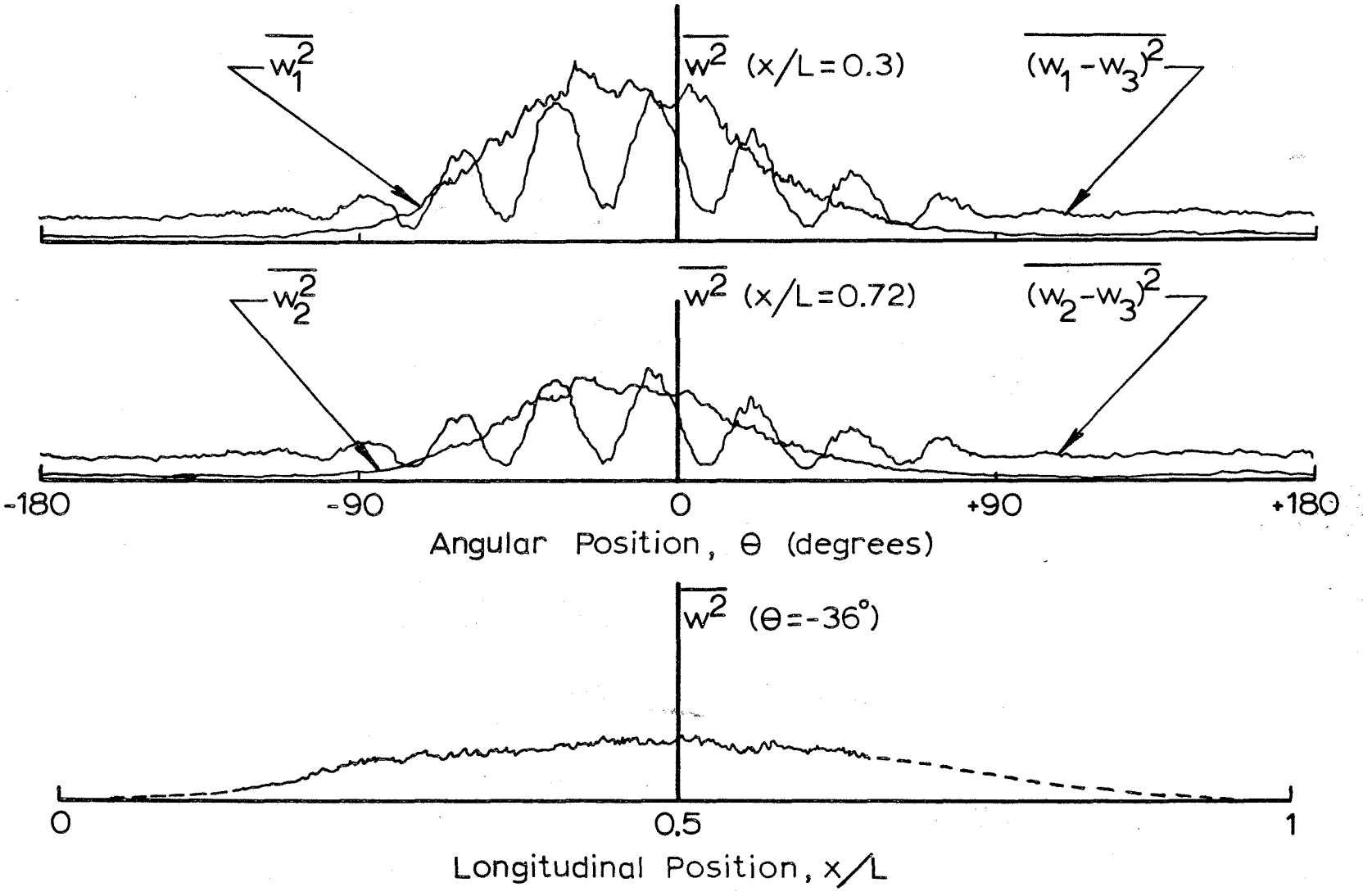

FIG. 25 LONGITUDINAL AND CIRCUMFERENTIAL TRAVERSES; CORR. #310

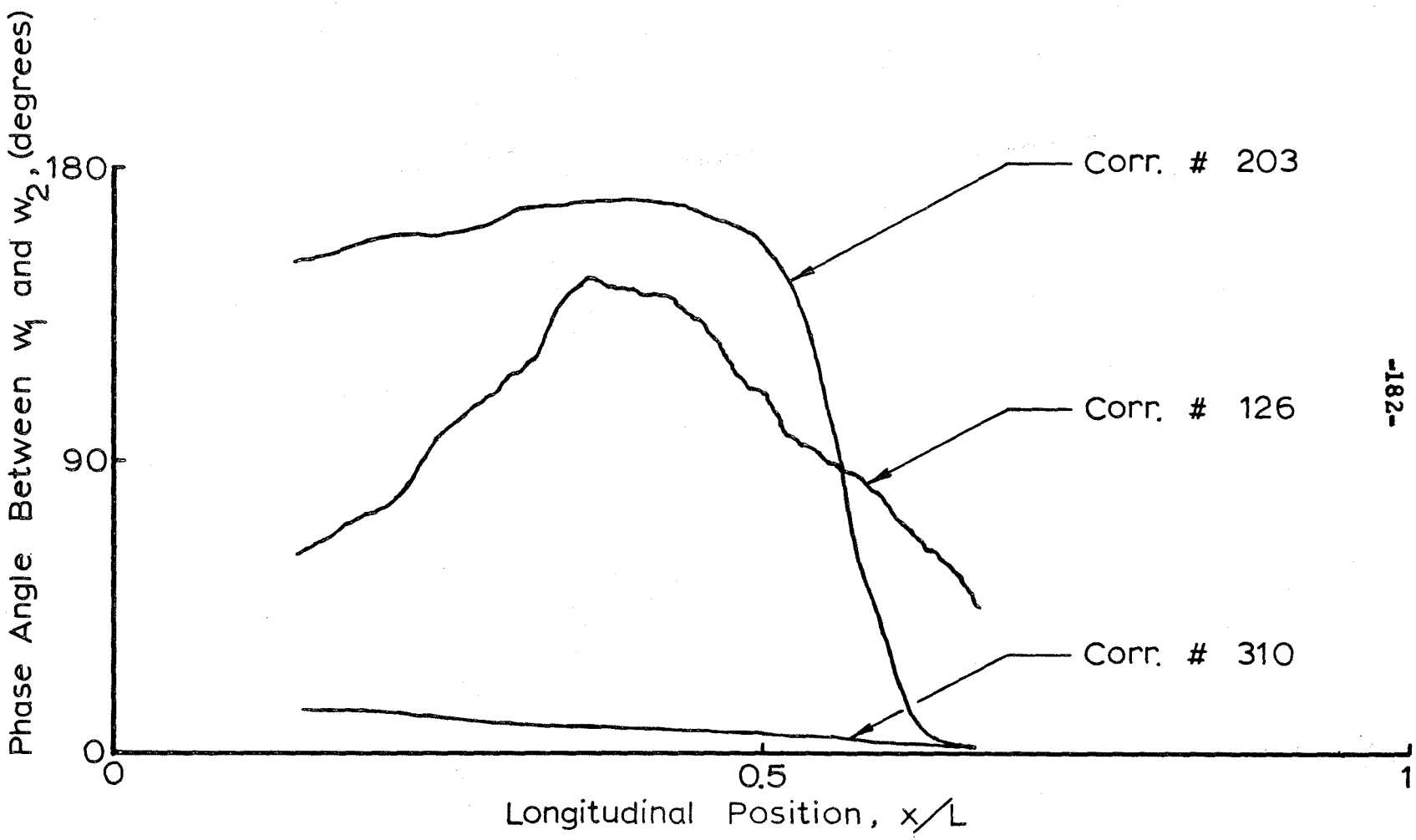

FIG. 26 LONGITUDINAL VARIATION OF PHASE ANGLE OF SHELL MOTION

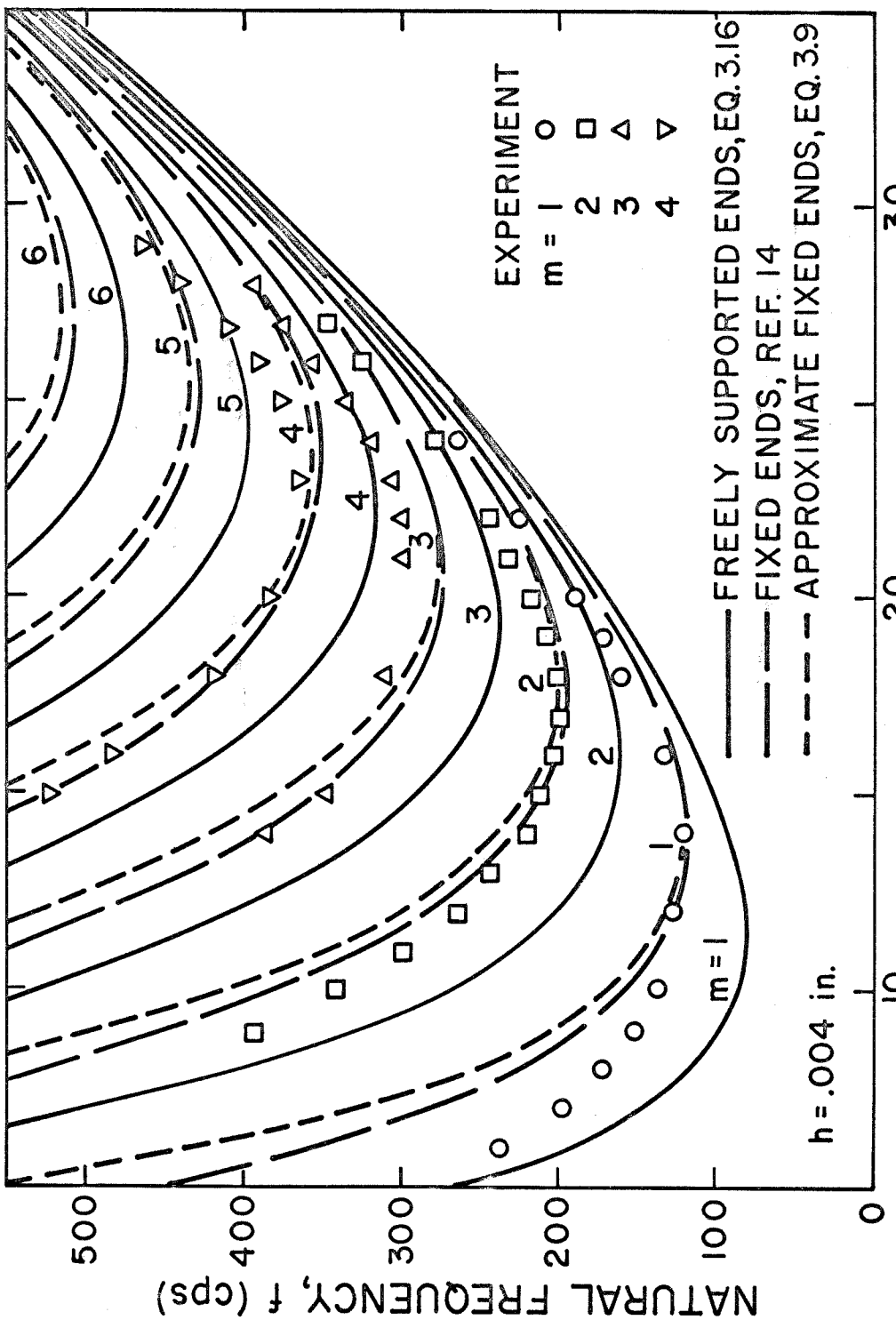

FIG.27 NATURAL FREQUENCIES OF UNSTRESSED CYLINDRICAL SHELL

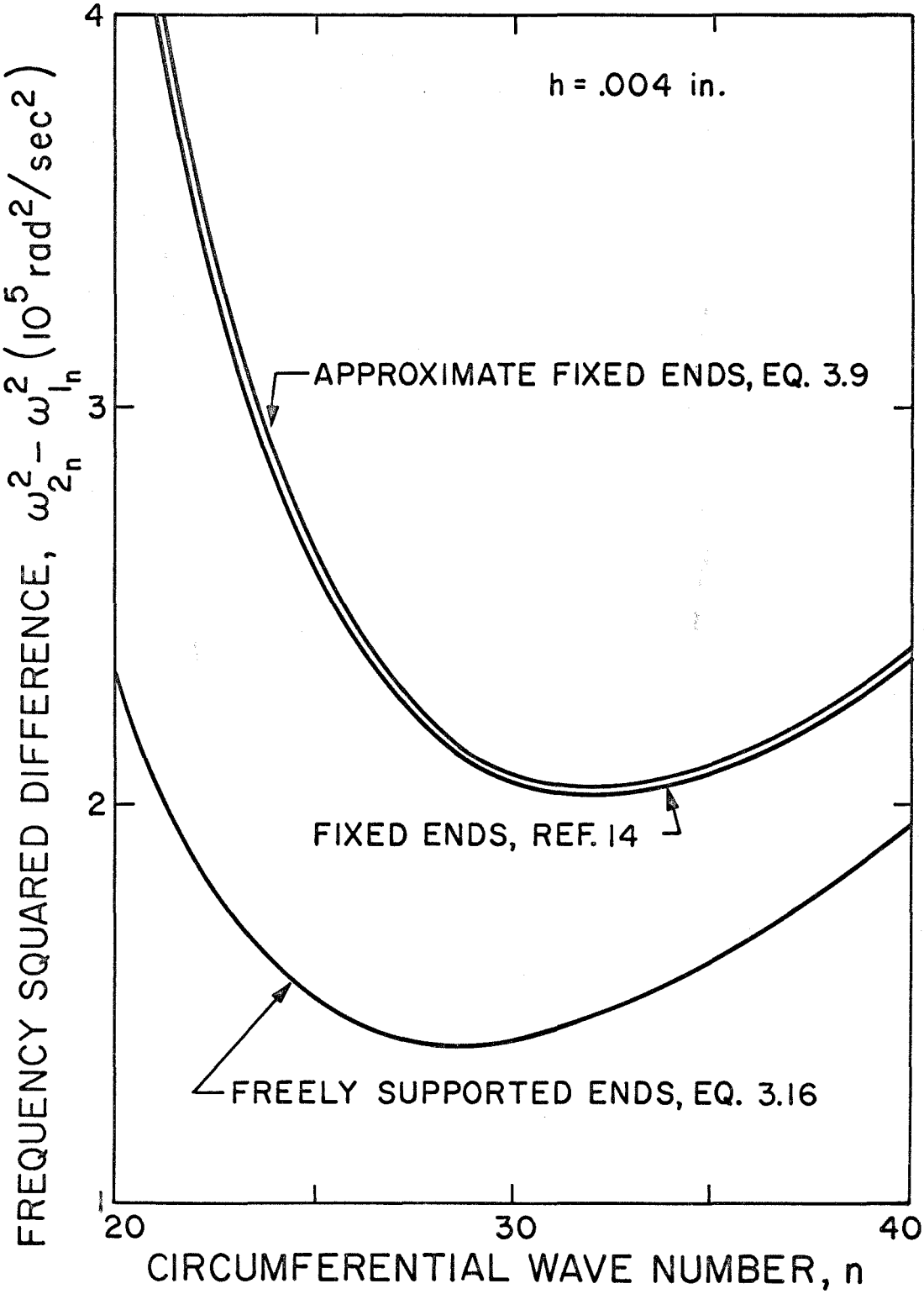

FIG.28 FREQUENCY SQUARED DIFFERENCES FOR UNSTRESSED CYLINDRICAL SHELL

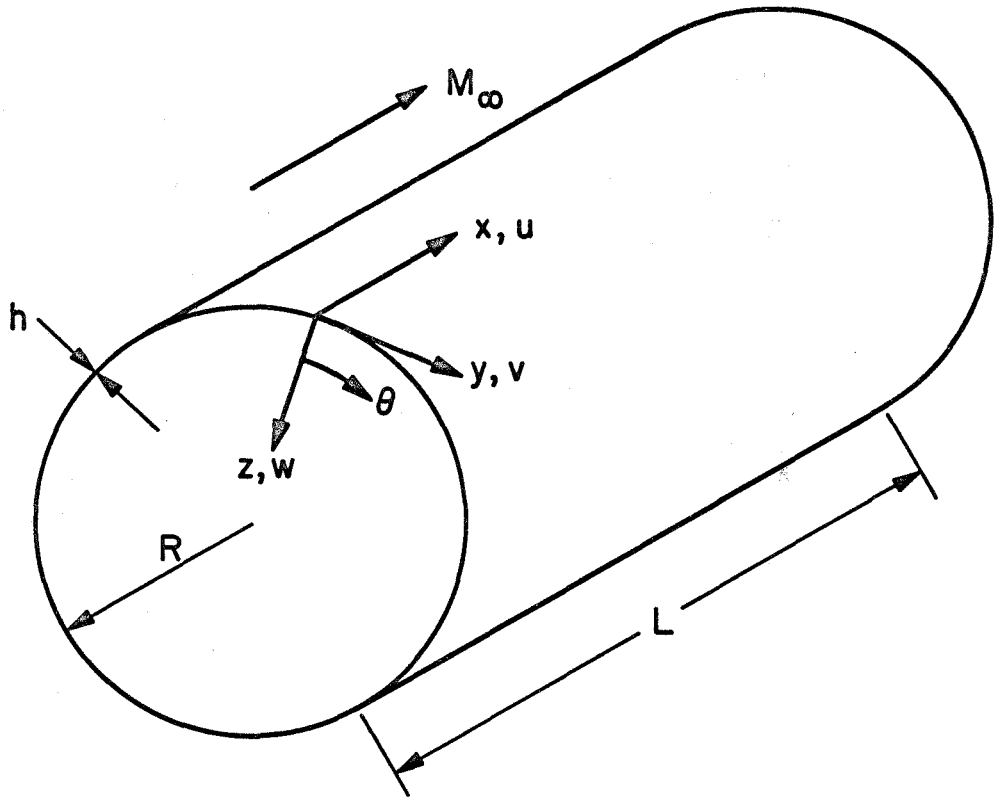

FIG.29 SHELL GEOMETRY AND COORDINATE SYSTEM

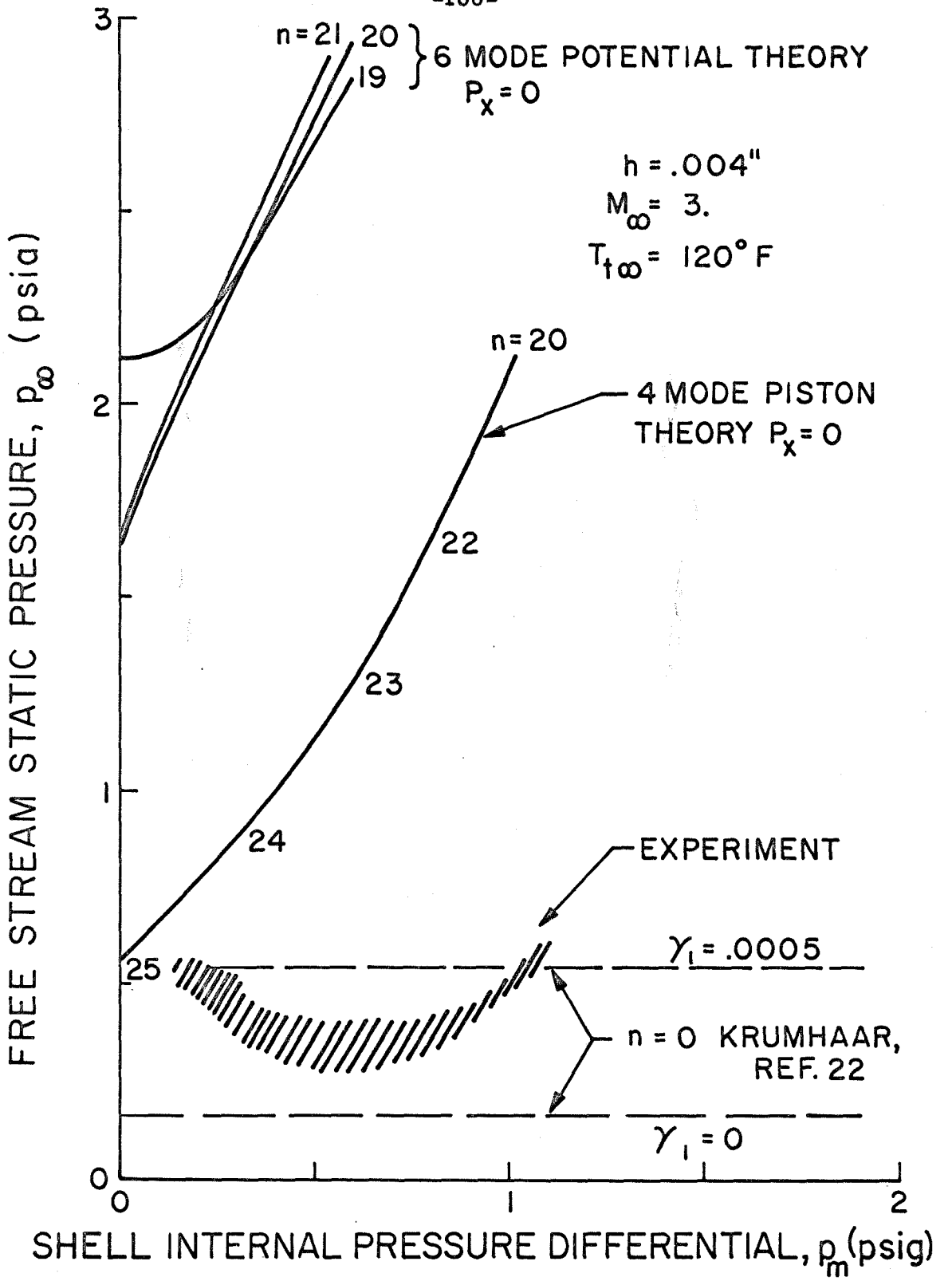

FIG.30 CYLINDRICAL SHELL FLUTTER BOUNDARIES

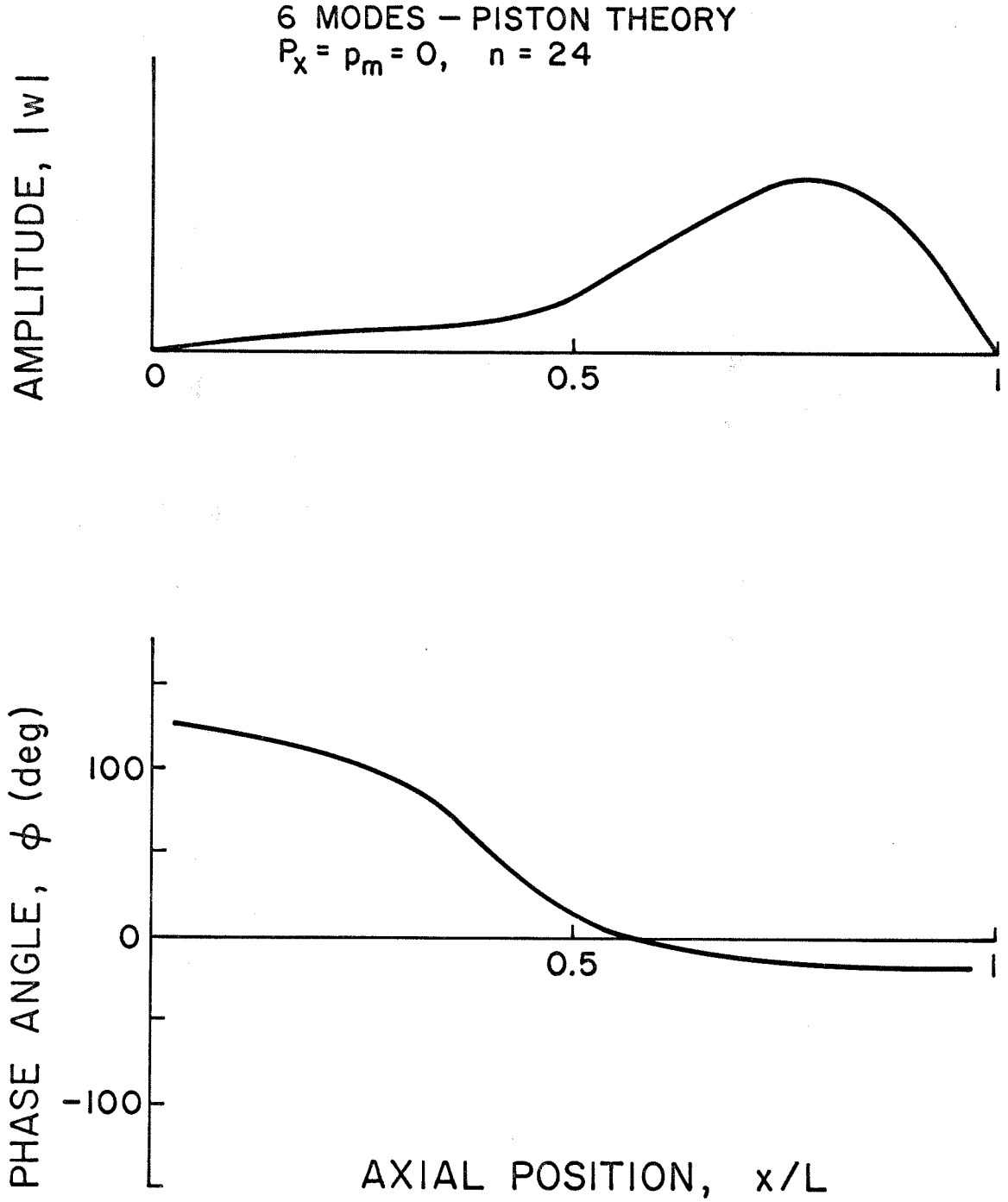

FIG. 31 AXIAL VARIATION OF FLUTTER MODE

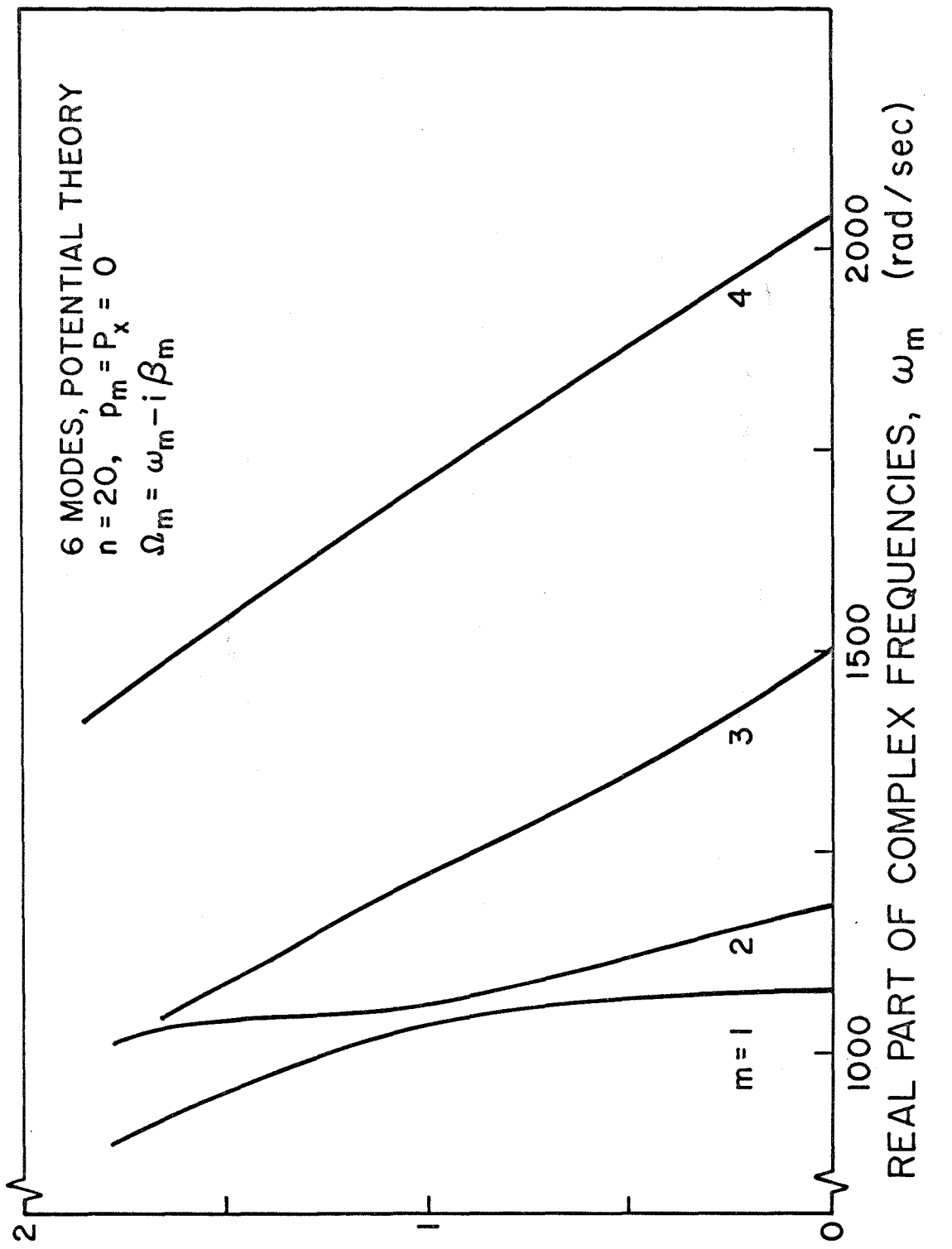

FIG.32 LOCUS OF FREQUENCY ROOTS AS p_∞ INCREASES

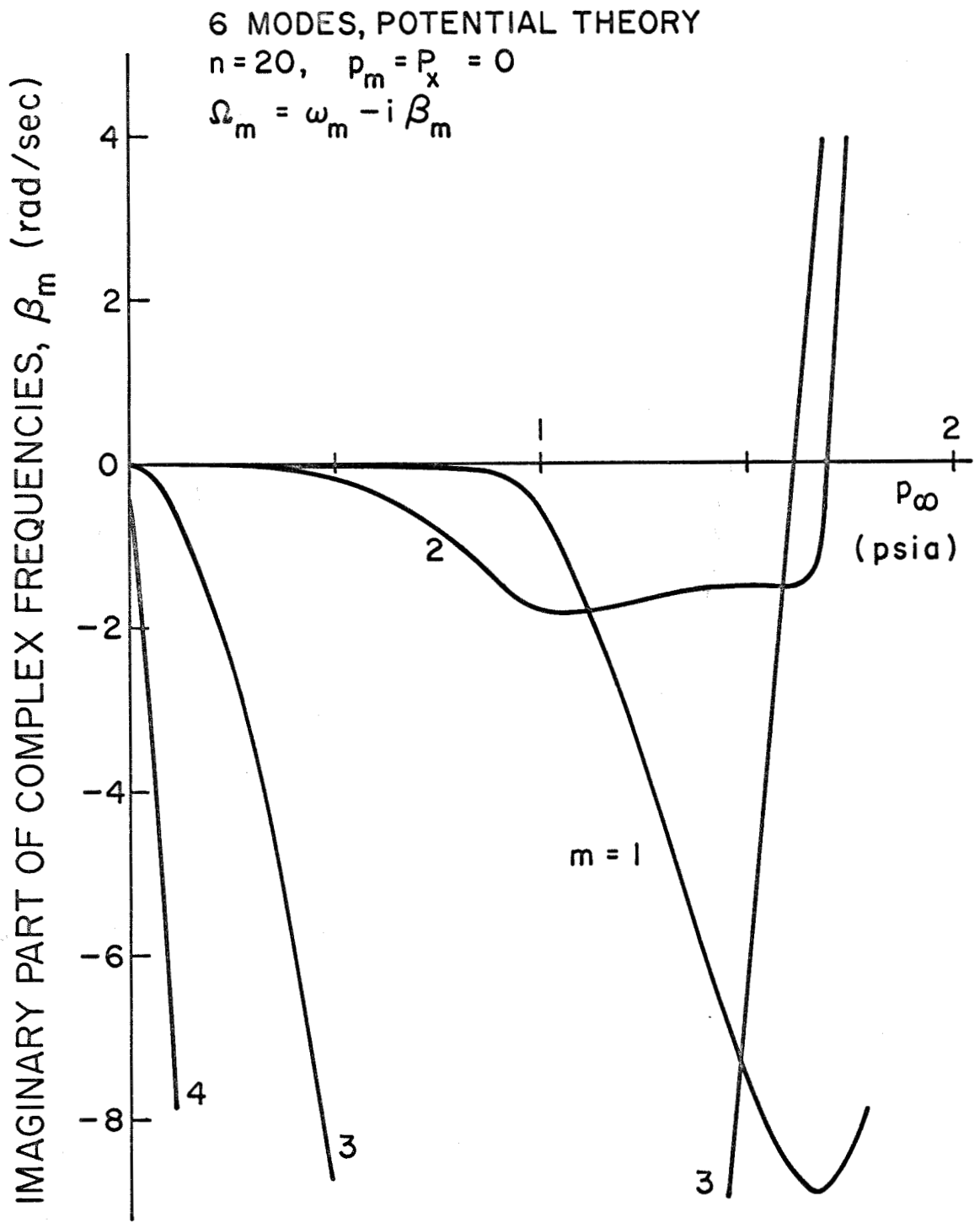

FIG.33 LOCUS OF FREQUENCY ROOTS AS p_∞ INCREASES

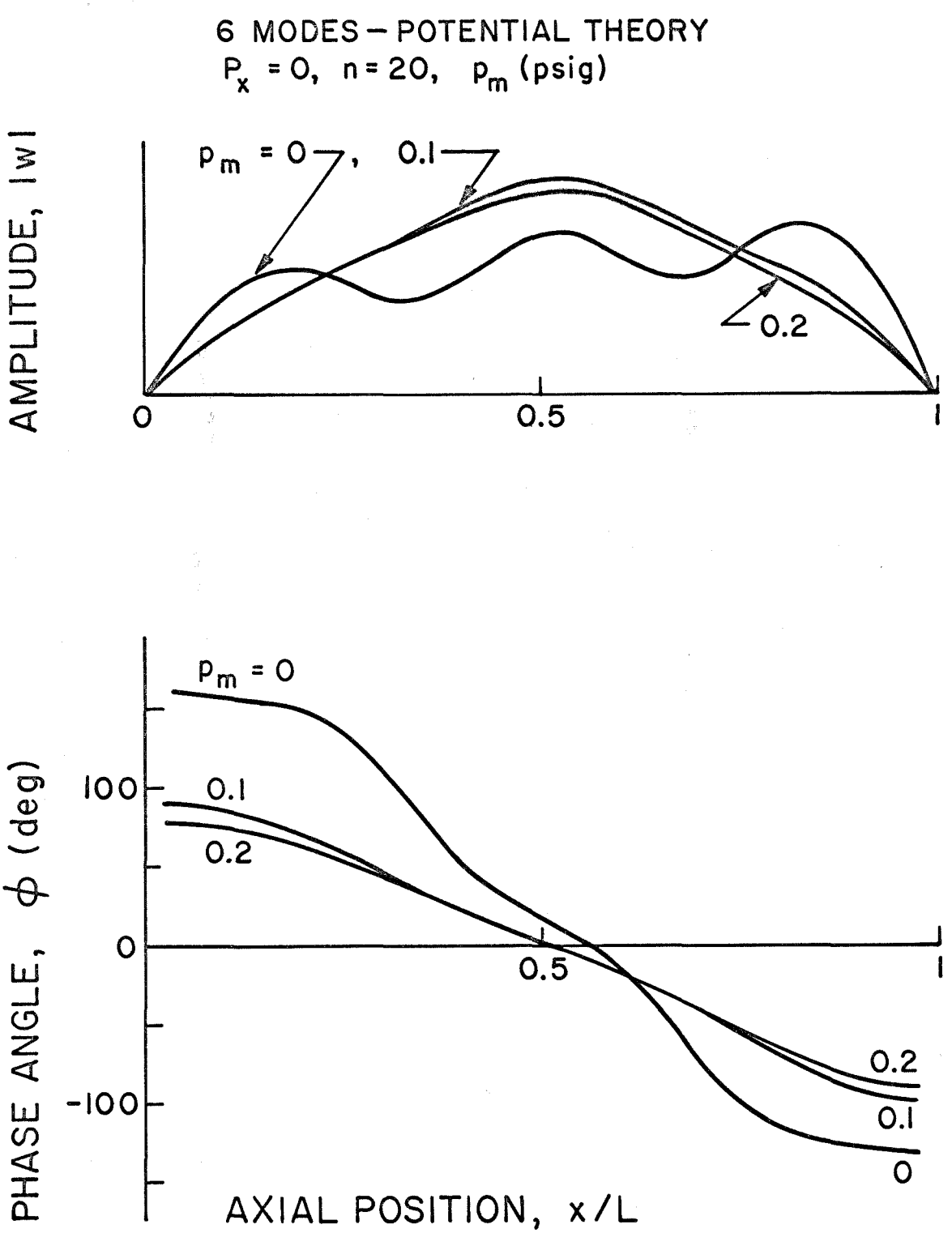

FIG.34 AXIAL VARIATION OF FLUTTER MODE

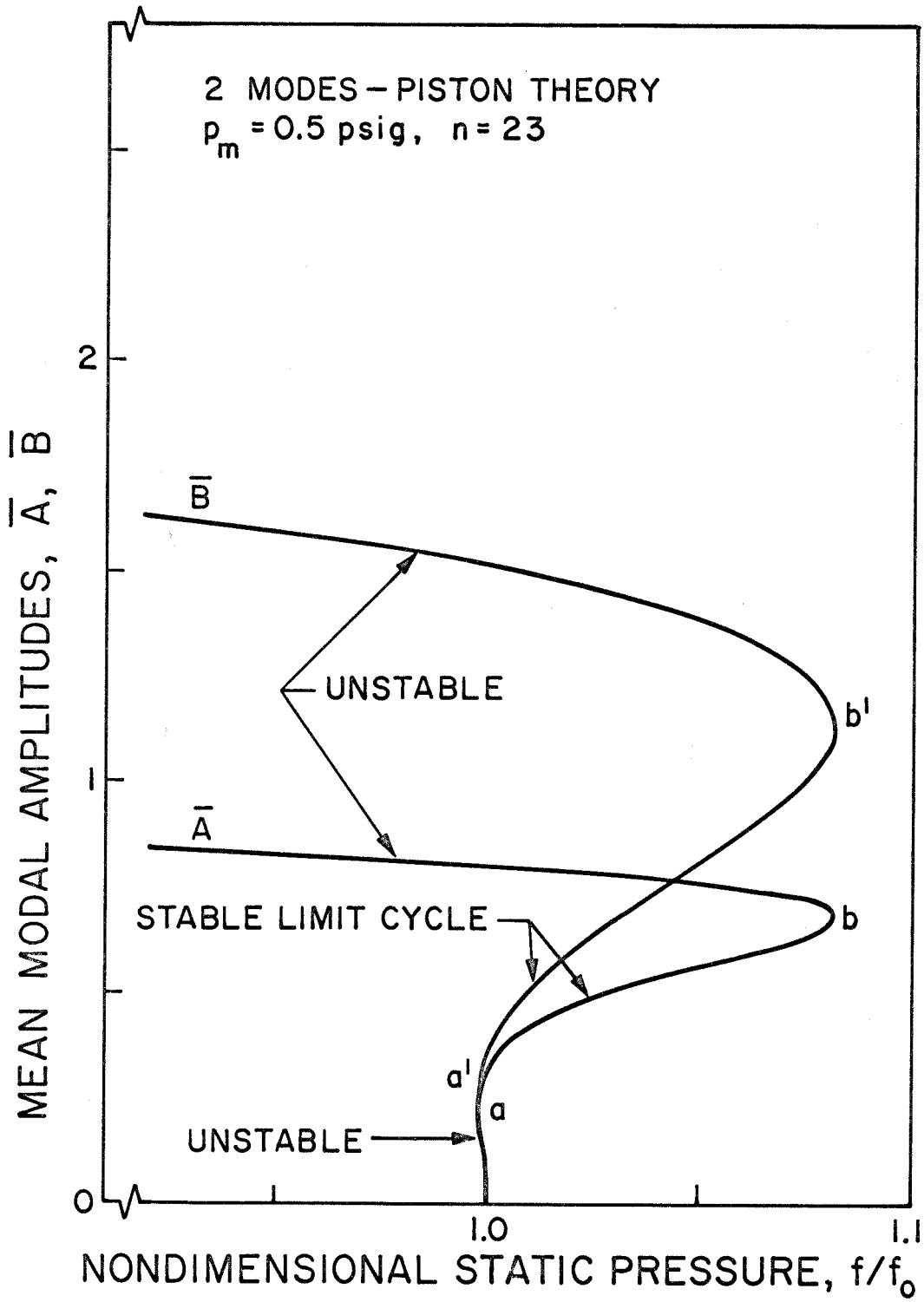

FIG.35 LIMIT CYCLE AMPLITUDES

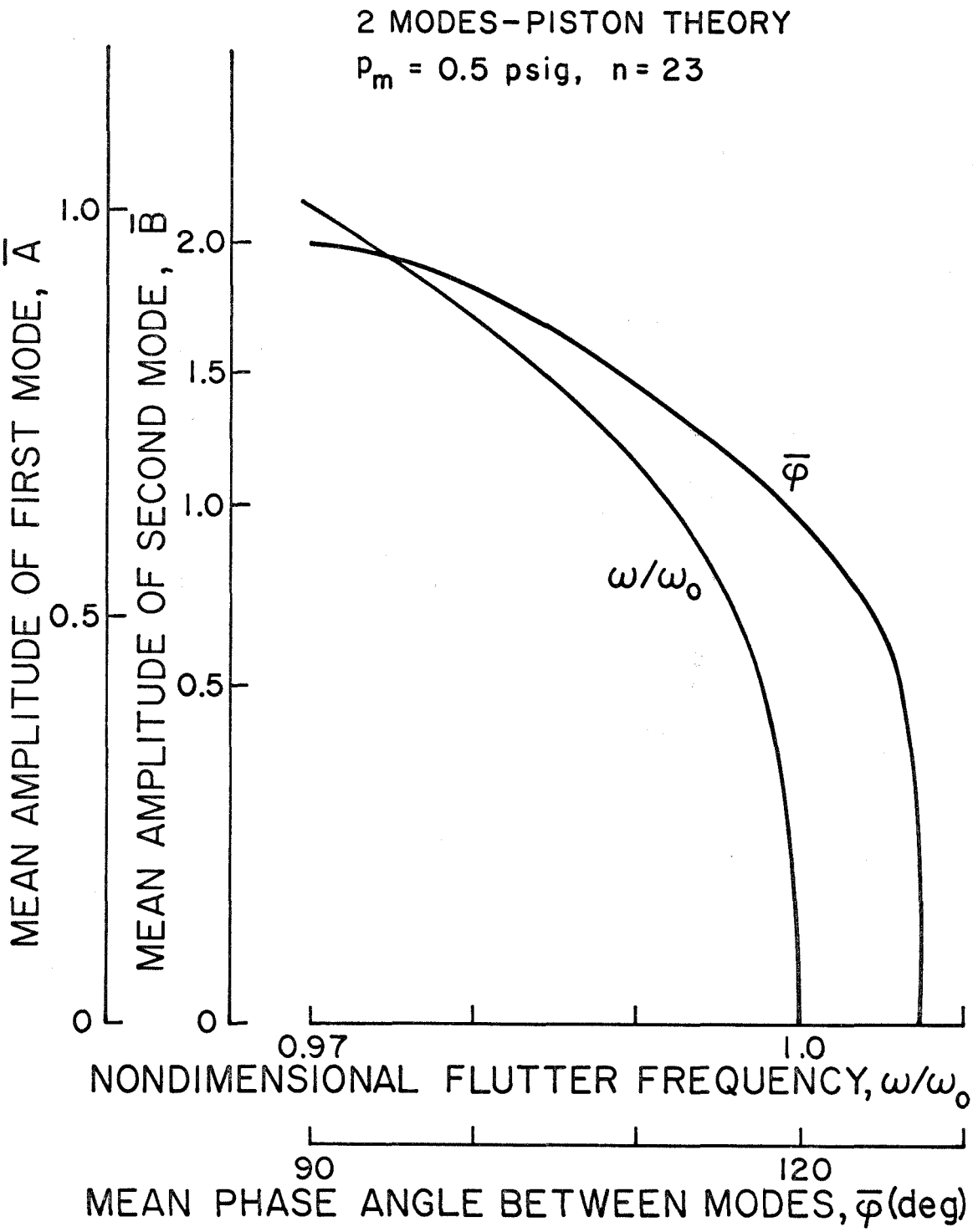

FIG.36 FLUTTER FREQUENCY AND PHASE ANGLE DEPENDENCE ON AMPLITUDE

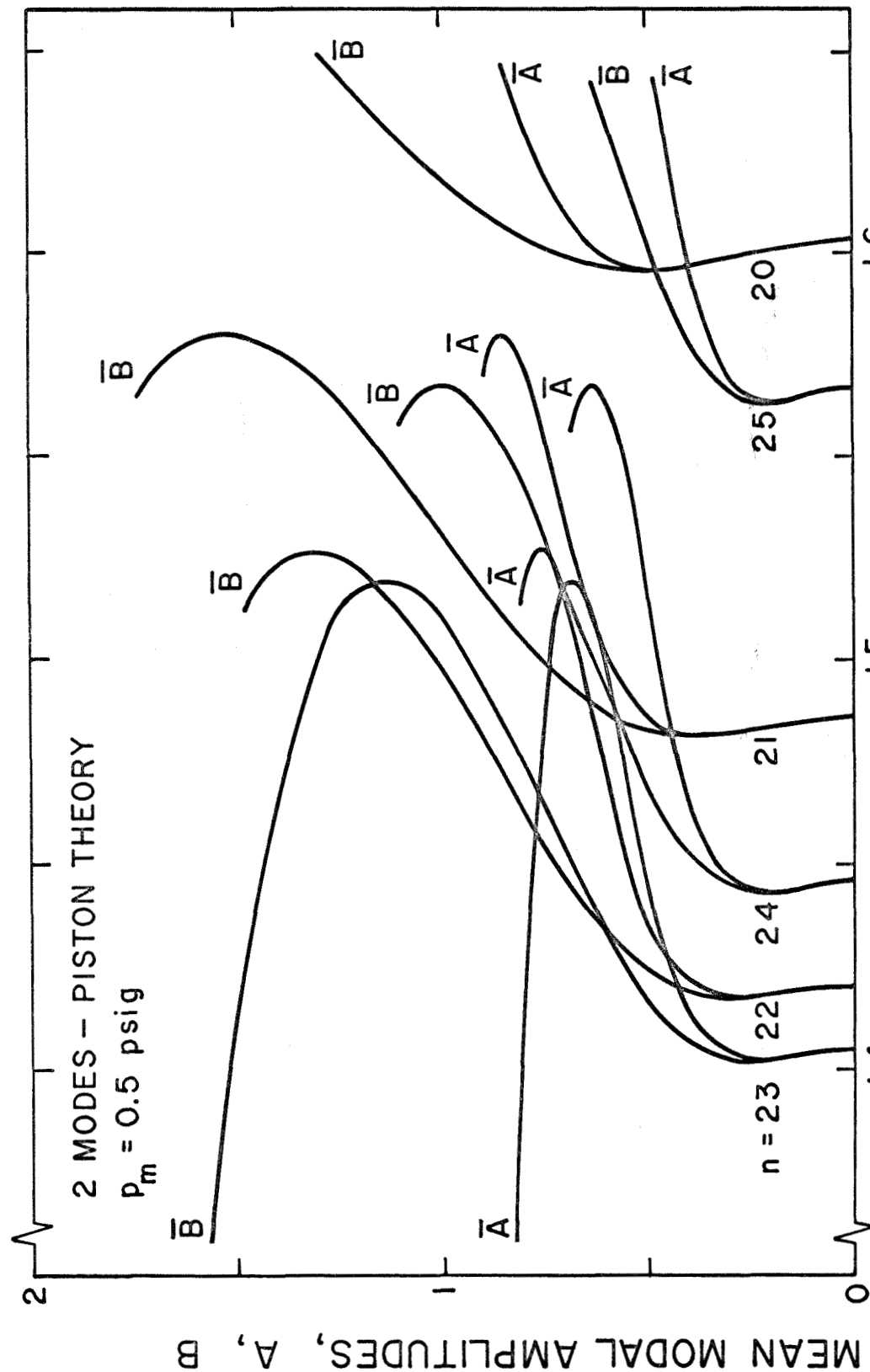

FIG. 37 LIMIT CYCLE AMPLITUDES FOR INCREASING STATIC PRESSURE

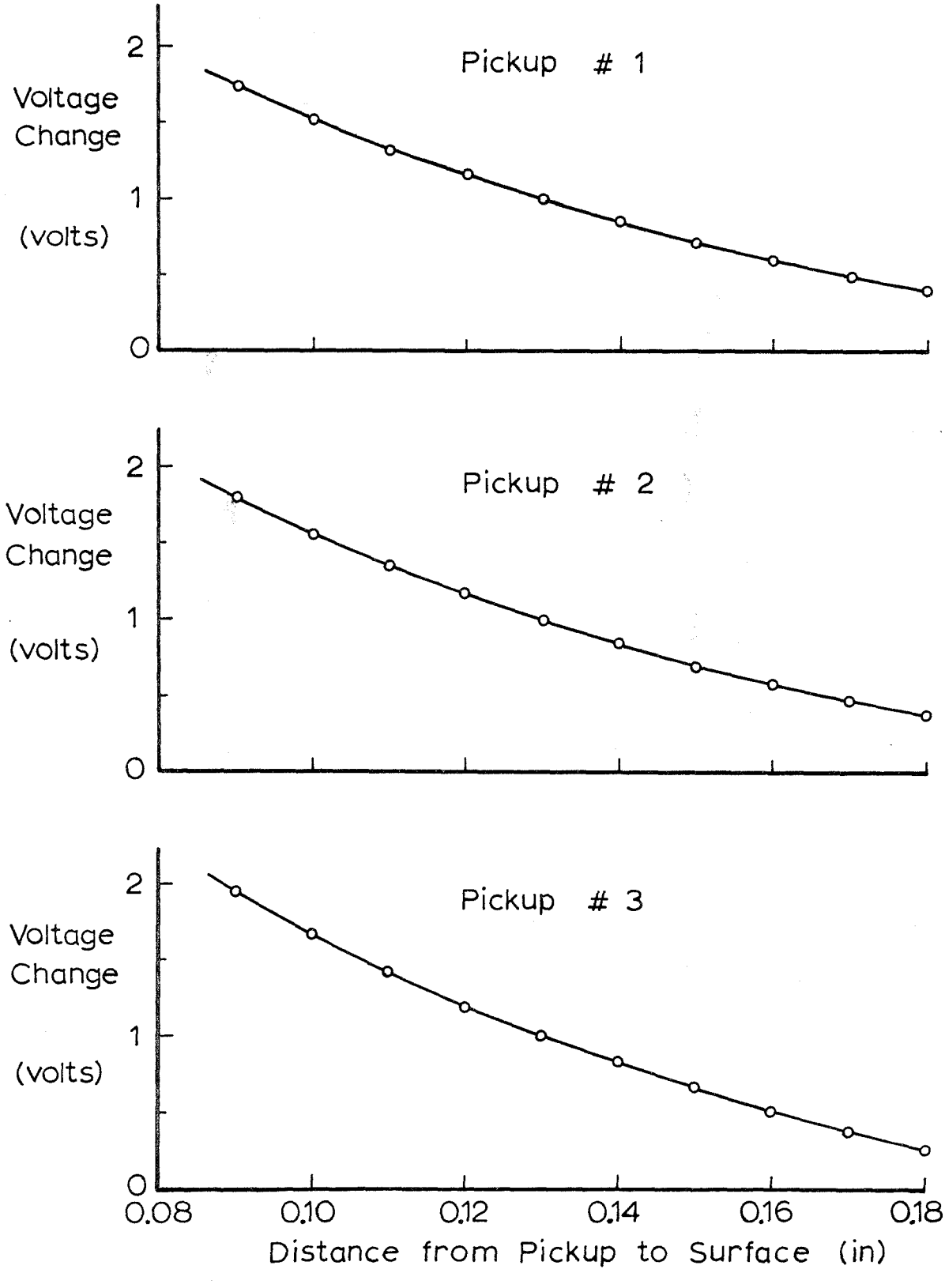

FIG. A.1 PICKUP CALIBRATION CURVES

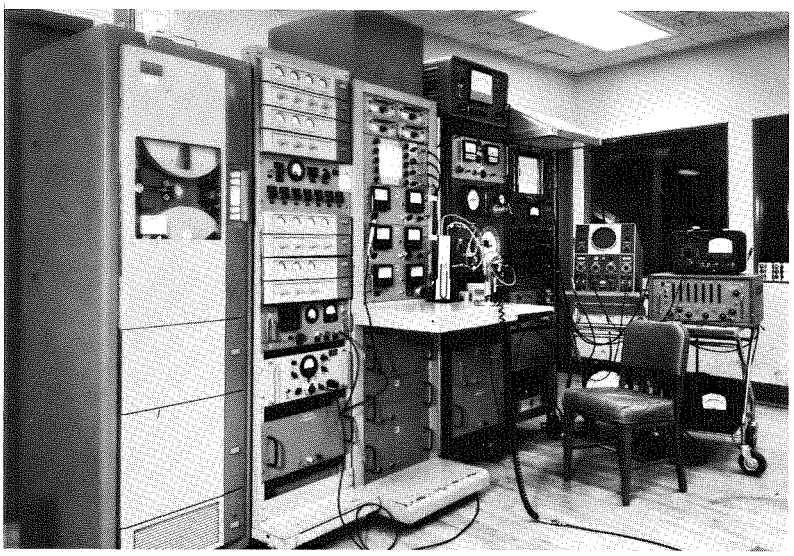

Figure A. 2: Instrument Arrangement in Tunnel Control Room

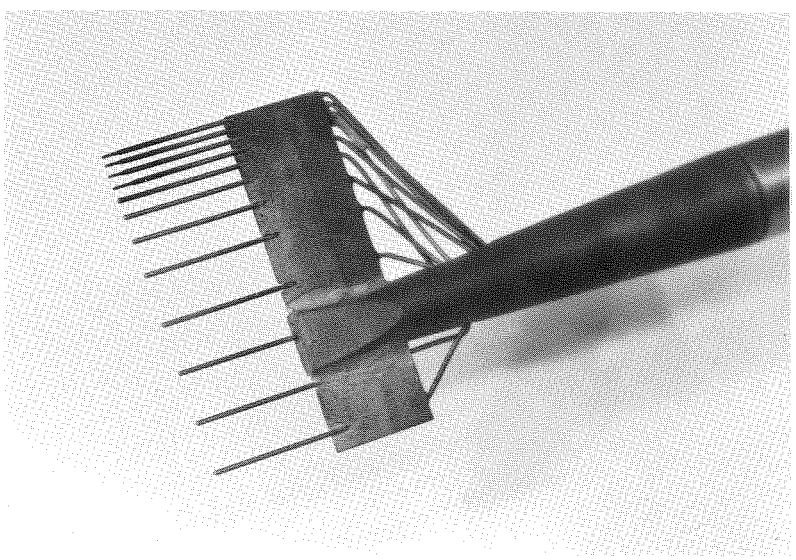

Figure A. 3: Close-up View of Boundary Layer Rake

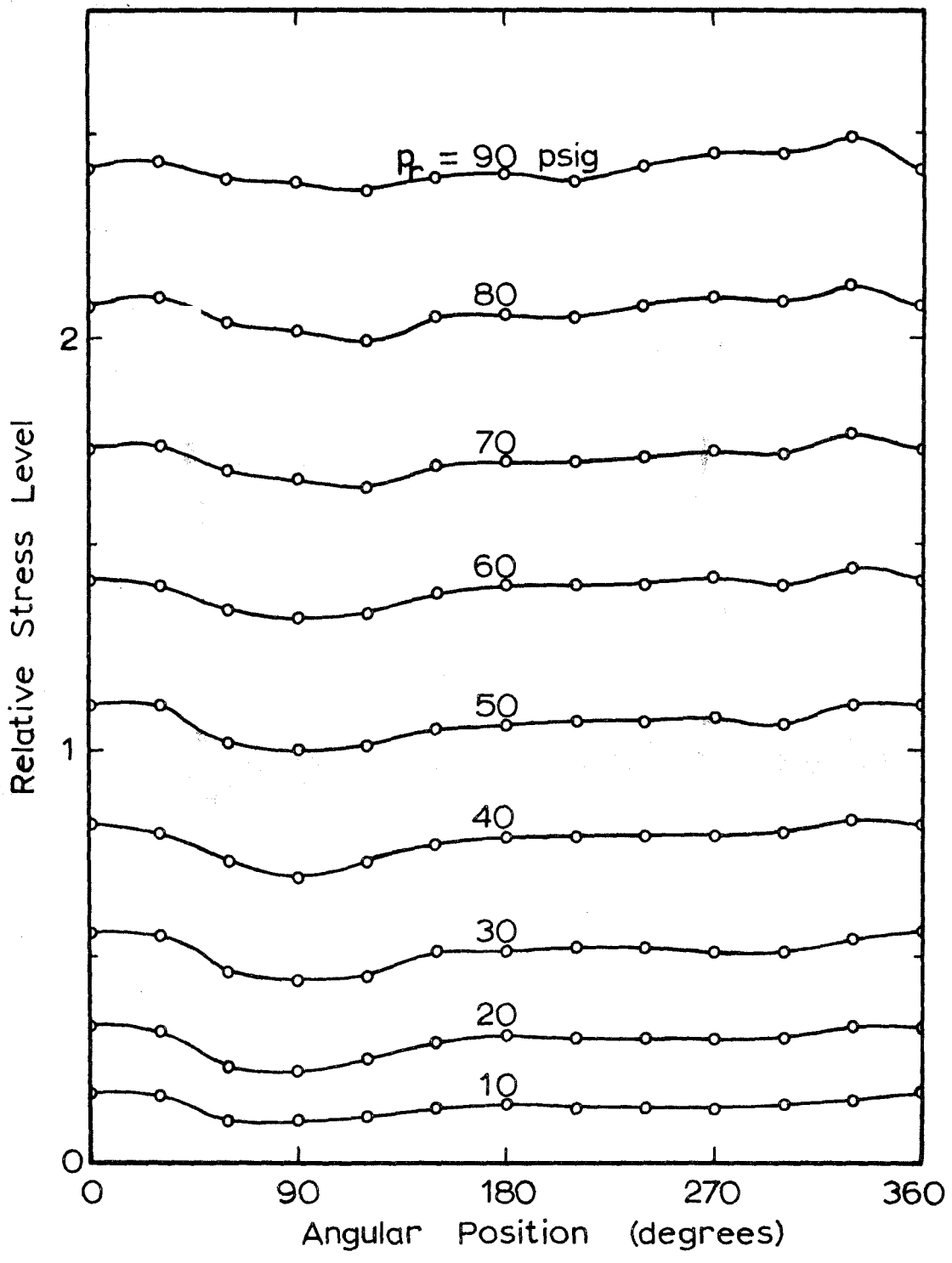

FIG. A.4 AXIAL STRESS DISTRIBUTION IN INSTRUMENTED SHELL

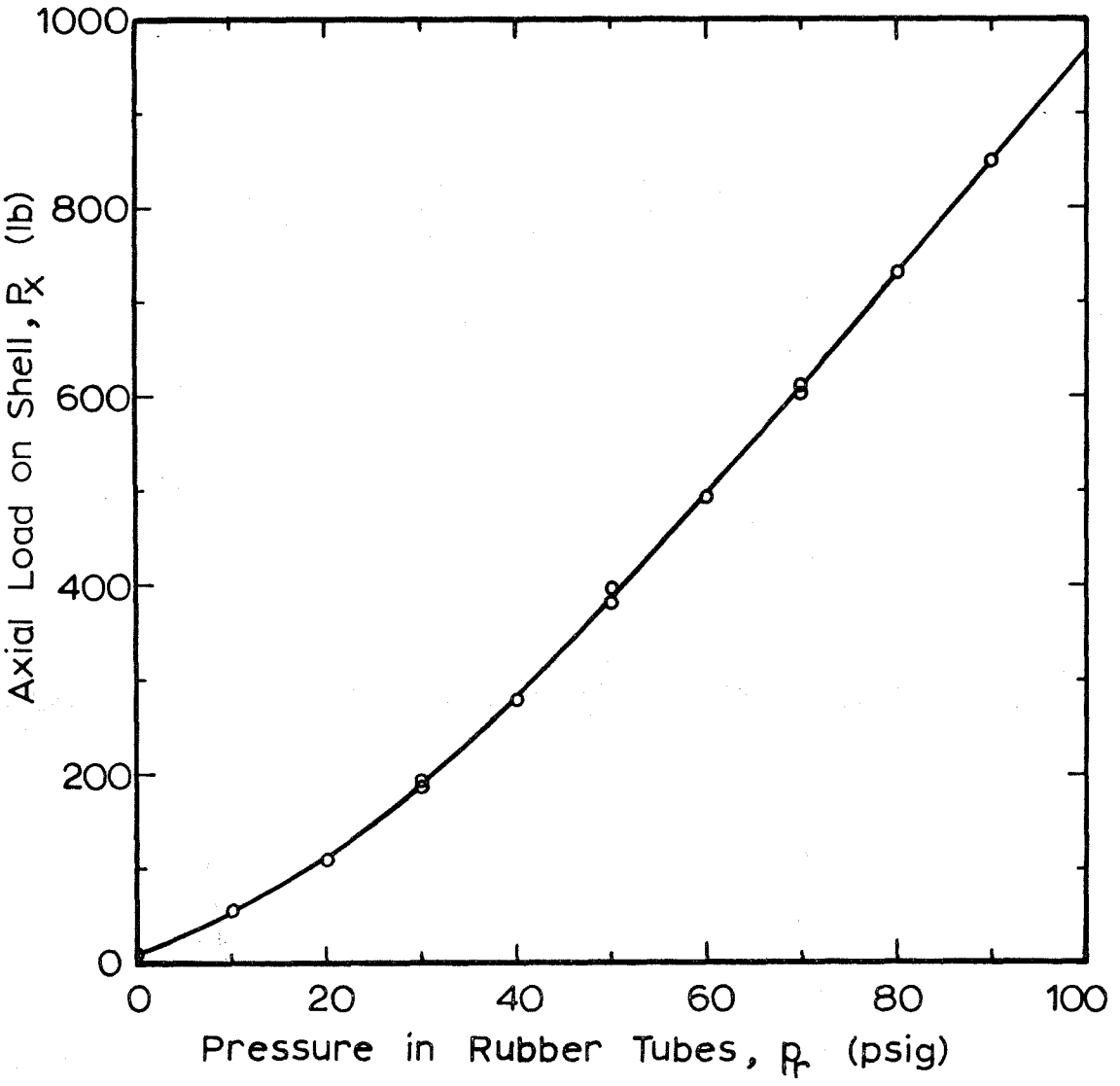

FIG. A.5 CALIBRATION OF AXIAL LOADING MECHANISM

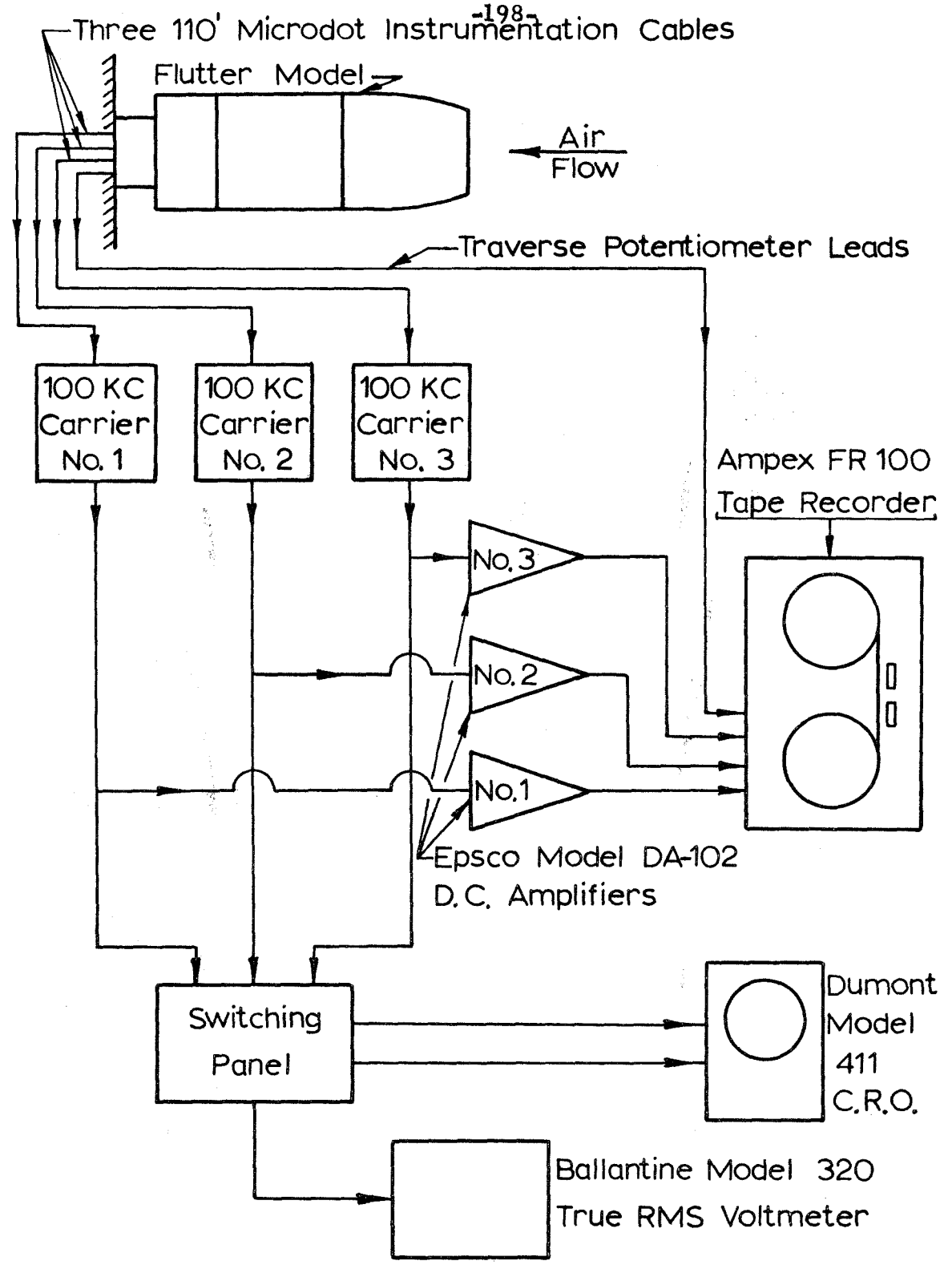

FIG. B.1 SCHEME OF DATA RECORDING CIRCUITRY

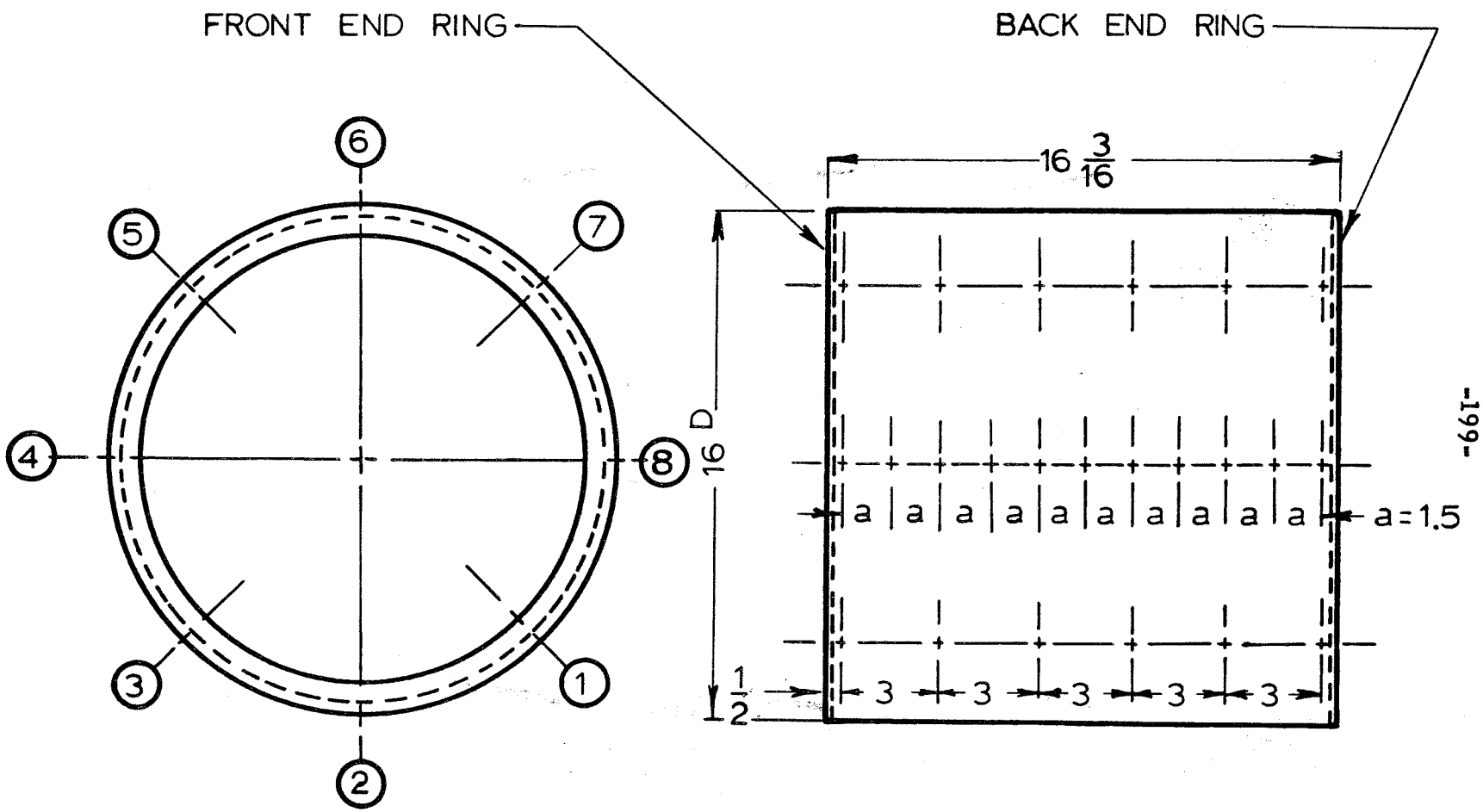

FIG. E.1 SCHEMATIC LAYOUT OF STATIC PRESSURE PORTS

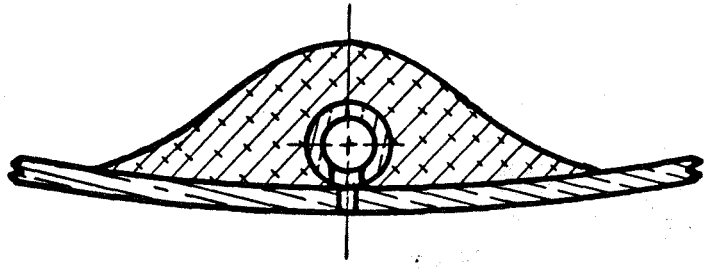

SECTION A-A

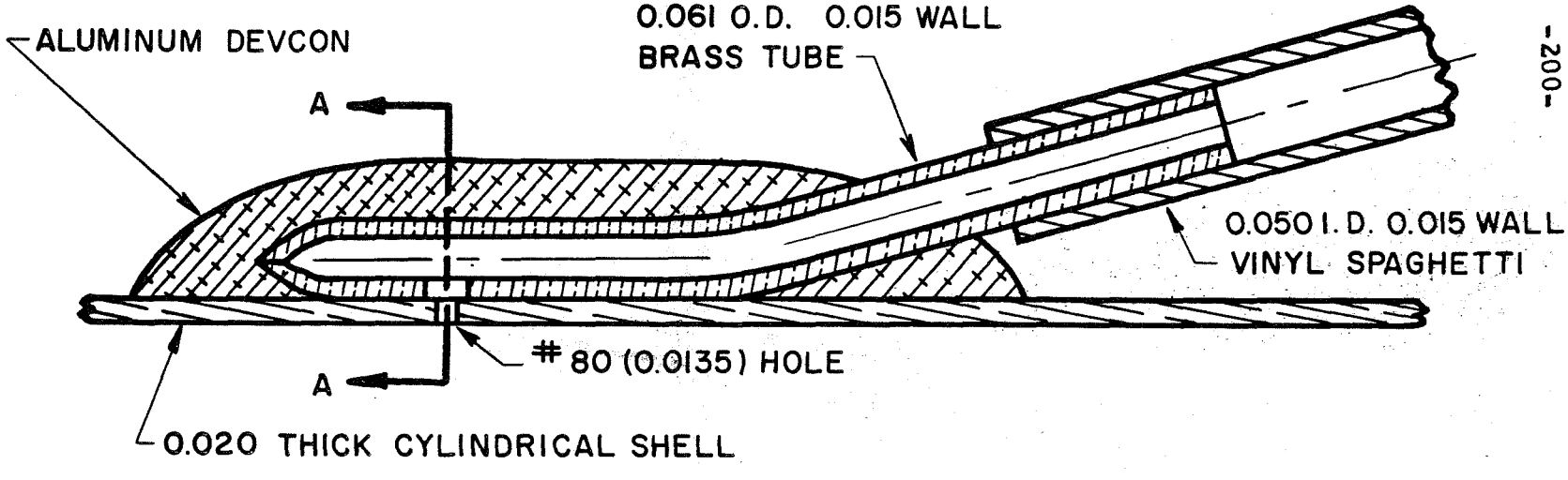

FIG. E.2 DETAILS OF A STATIC PRESSURE PORT

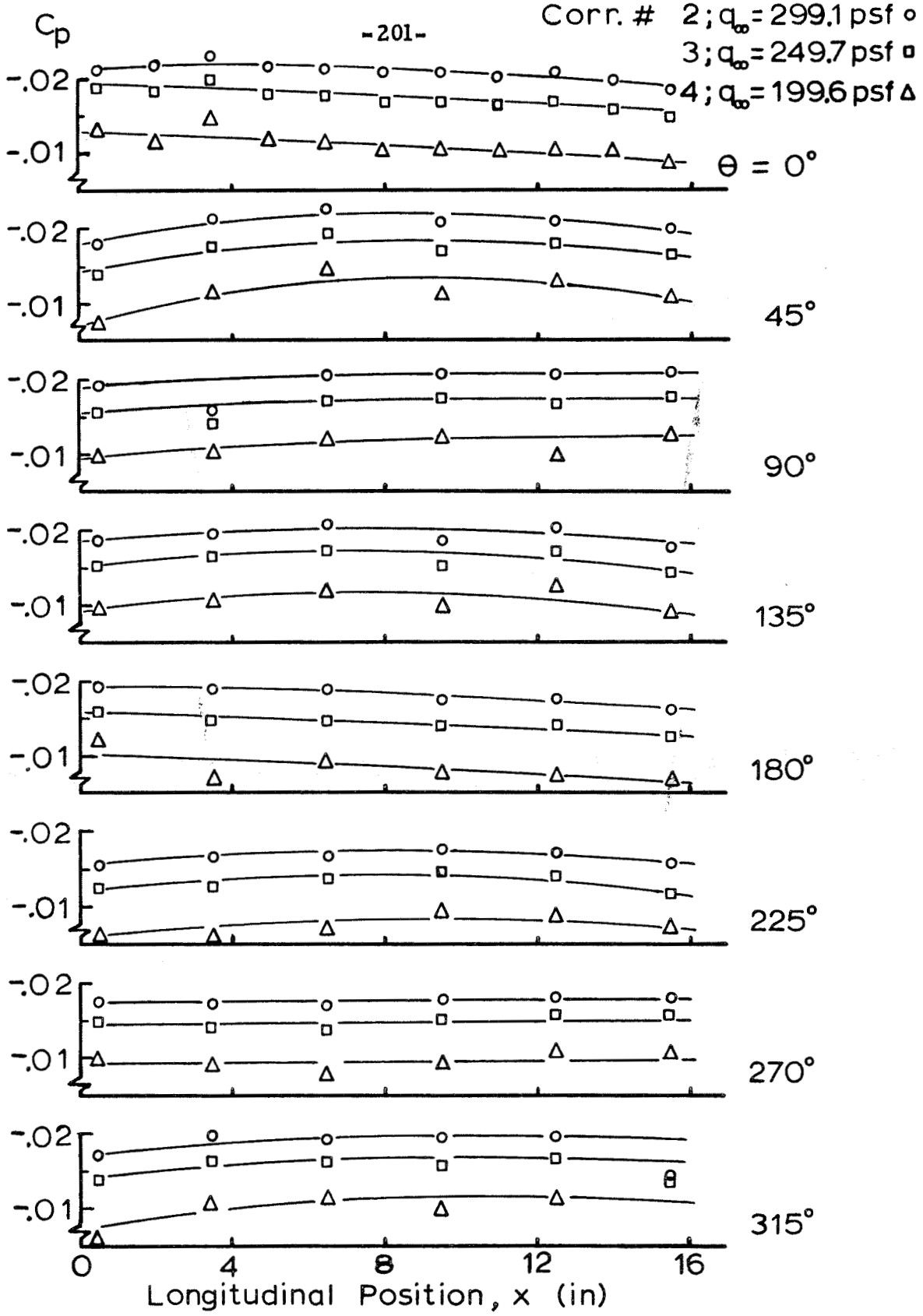

FIG. E.3 STATIC PRESSURE DISTRIBUTION, M_∞ = 3.400

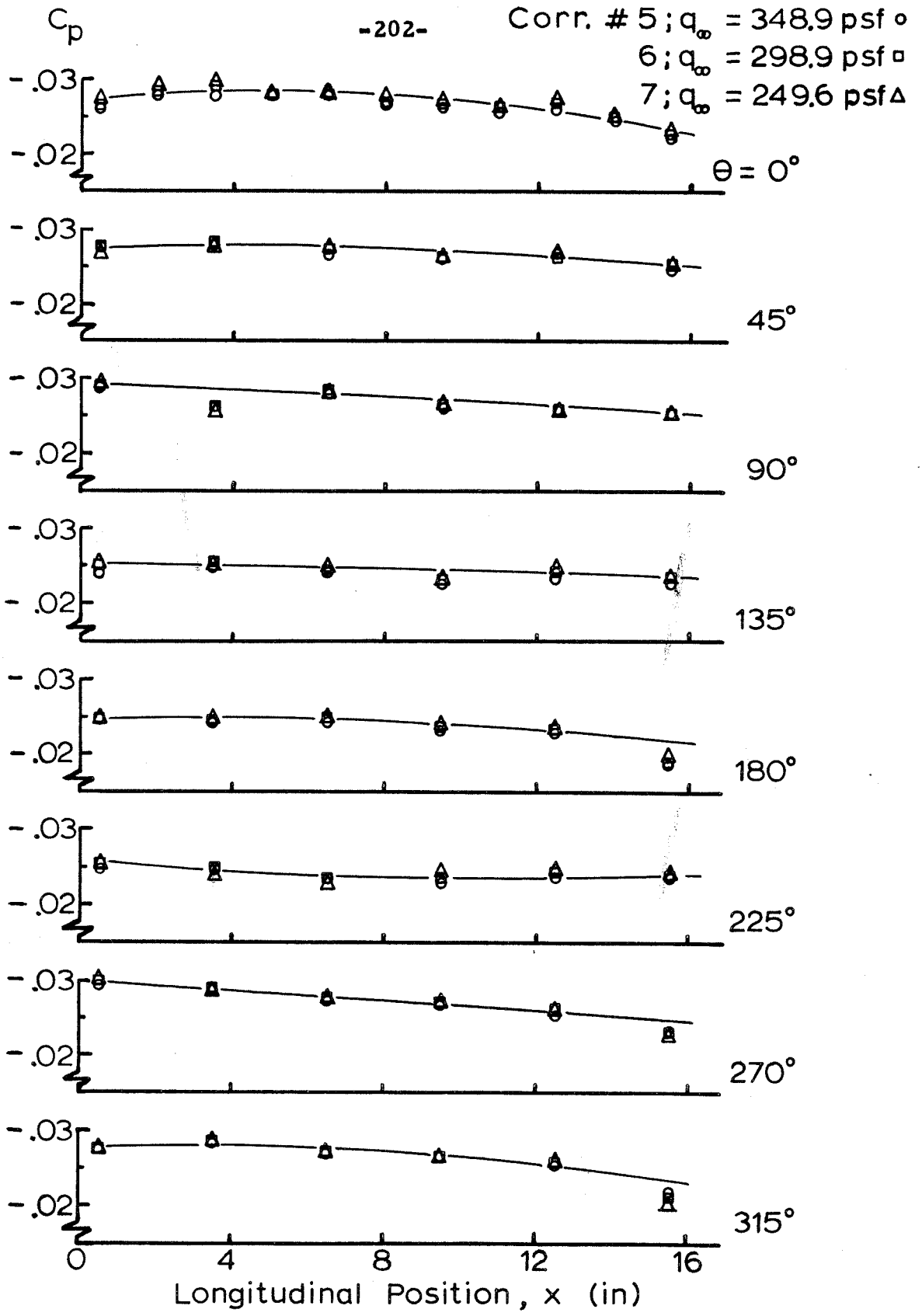

FIG. E.4 STATIC PRESSURE DISTRIBUTION, M_∞ = 3.003

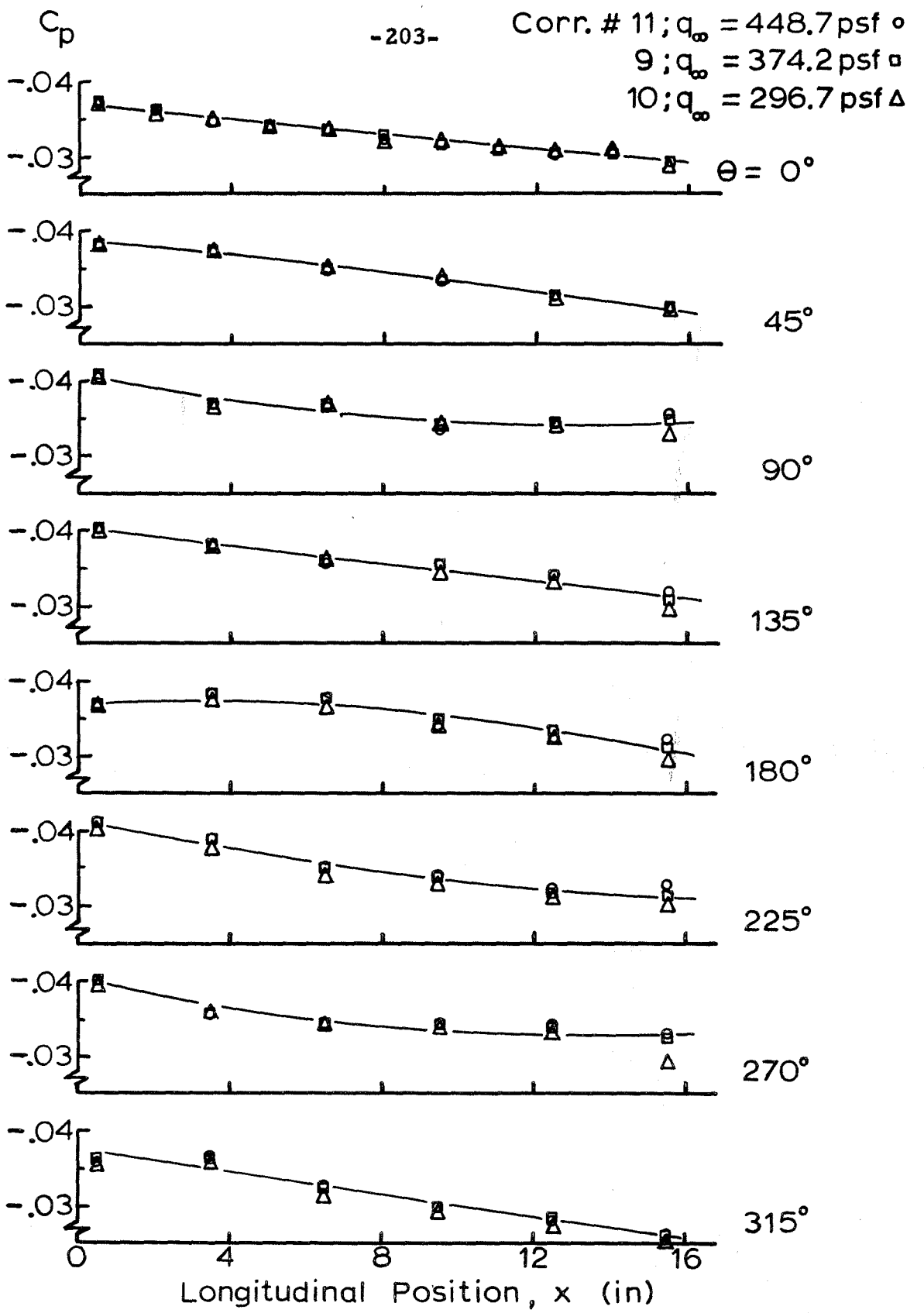

FIG. E.5 STATIC PRESSURE DISTRIBUTION, $M_\infty = 2.605$

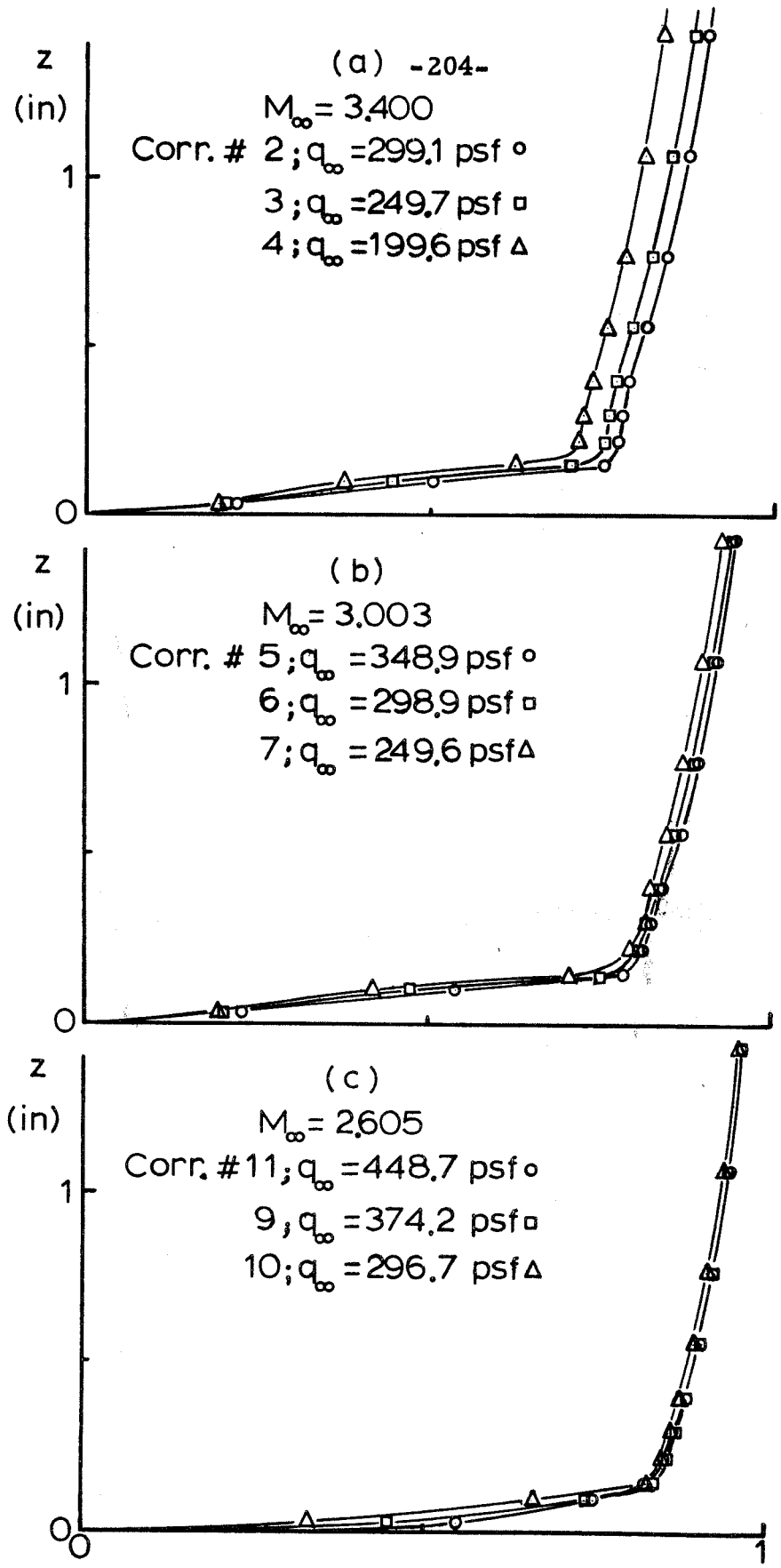

FIG. E.6 BOUNDARY LAYER PROFILES

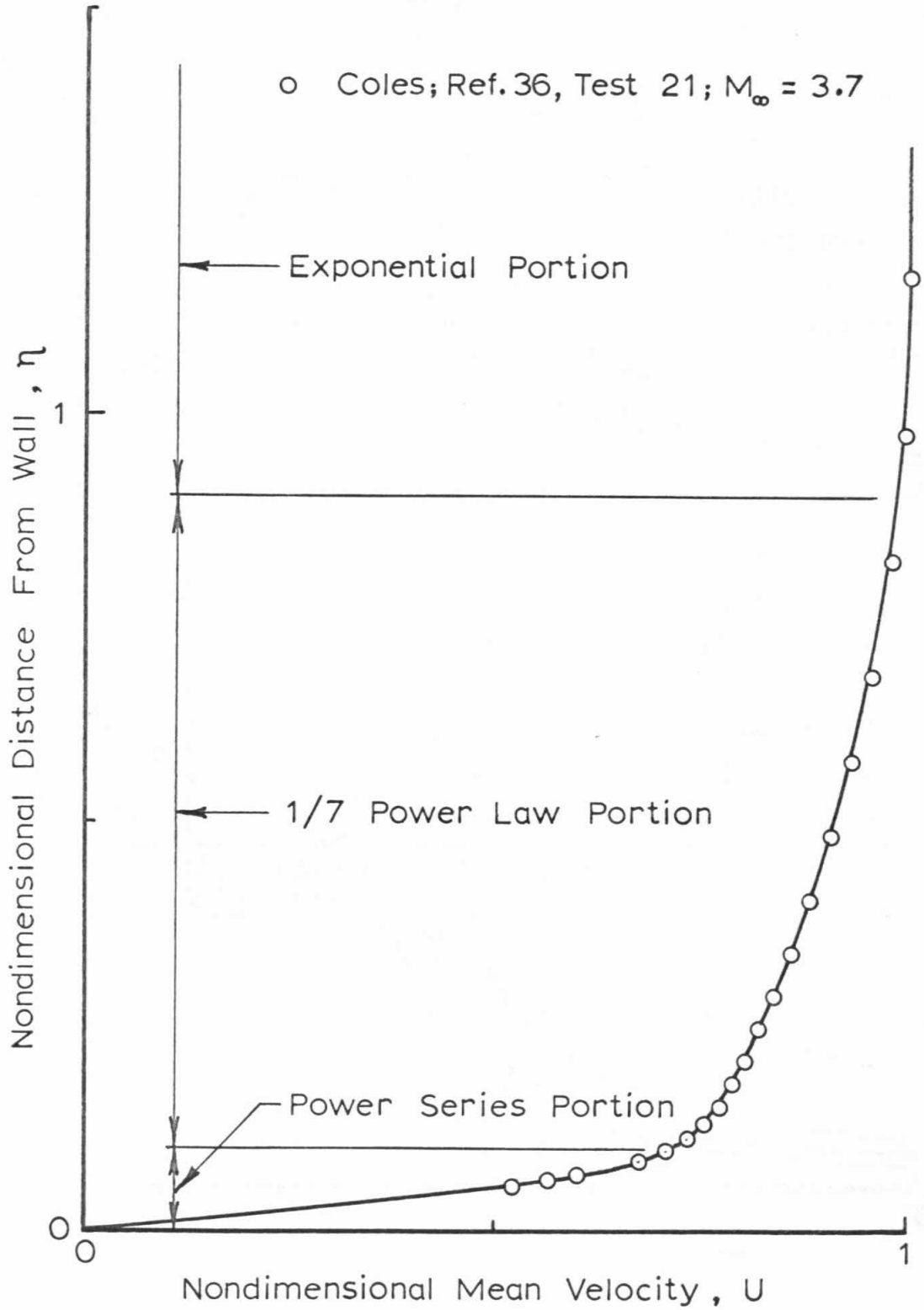

FIG. G.1 MEAN VELOCITY PROFILE

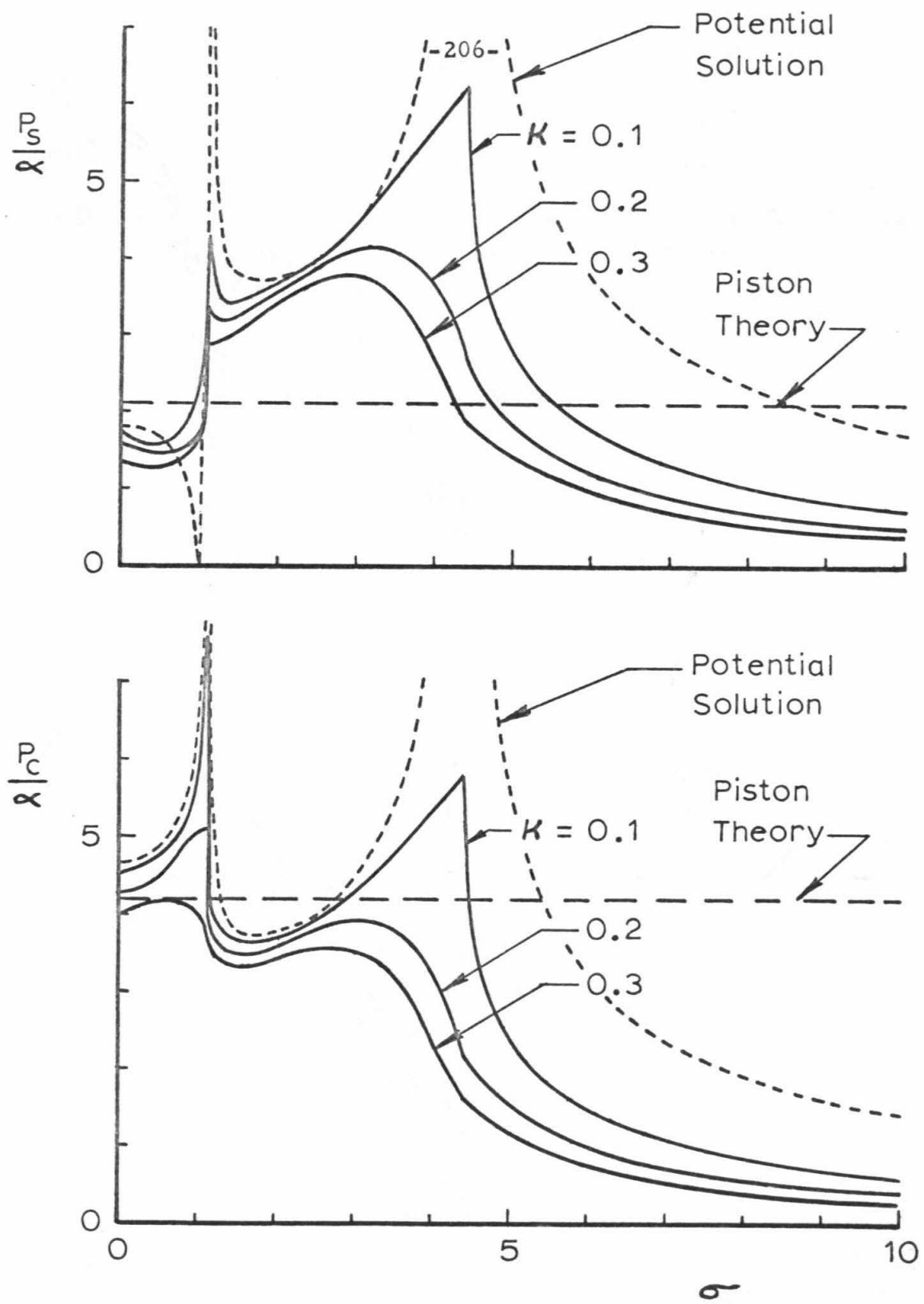

FIG. G.2 WALL PRESSURE AMPLITUDES ($M_\infty = 3.0$, $k = 0.5$)

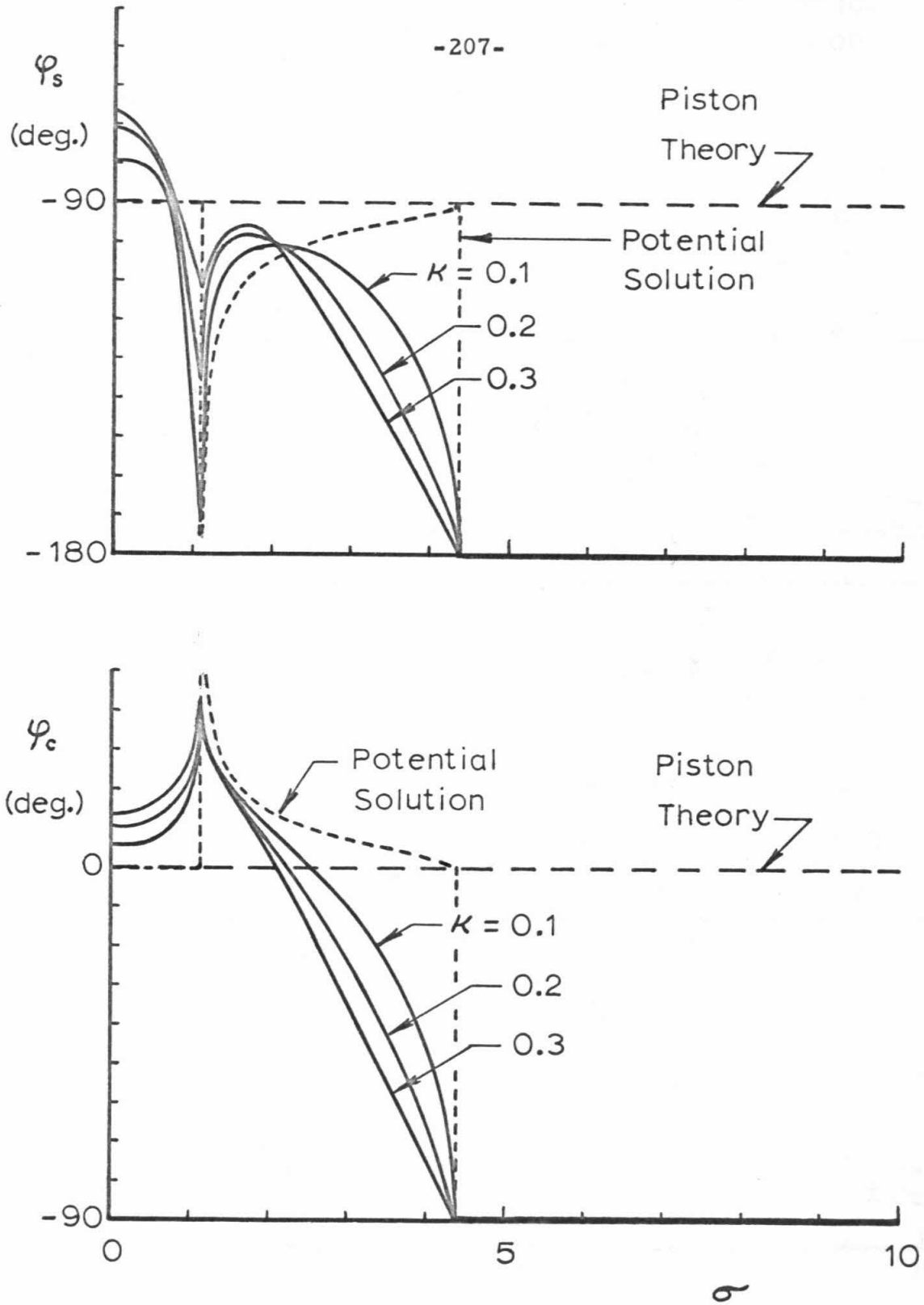

FIG. G.3 WALL PRESSURE PHASE ANGLES ($M_\infty = 3.0, k = 0.5$)

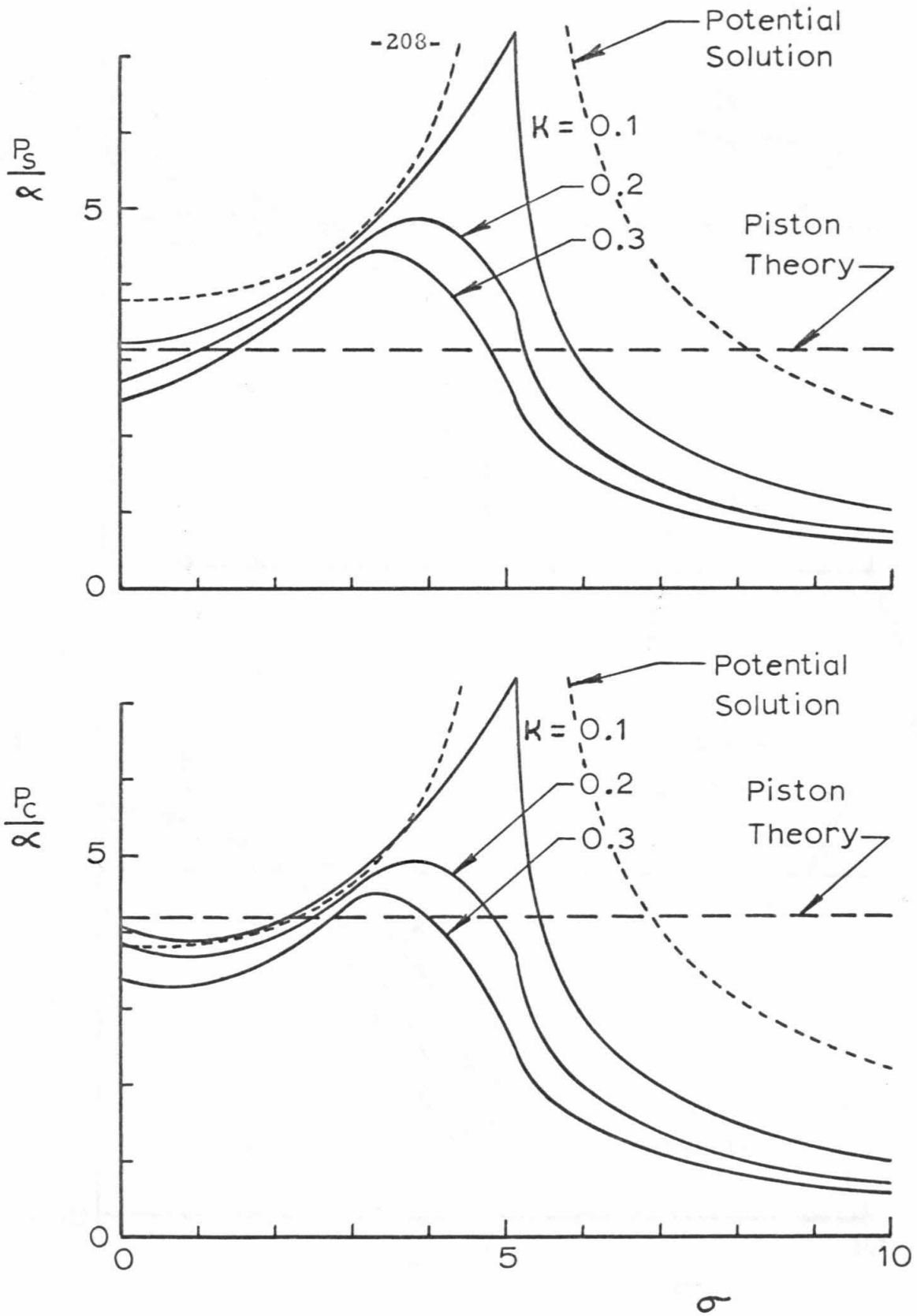

FIG. G.4 WALL PRESSURE AMPLITUDES ($M_\infty = 3.0, k = 0.75$)

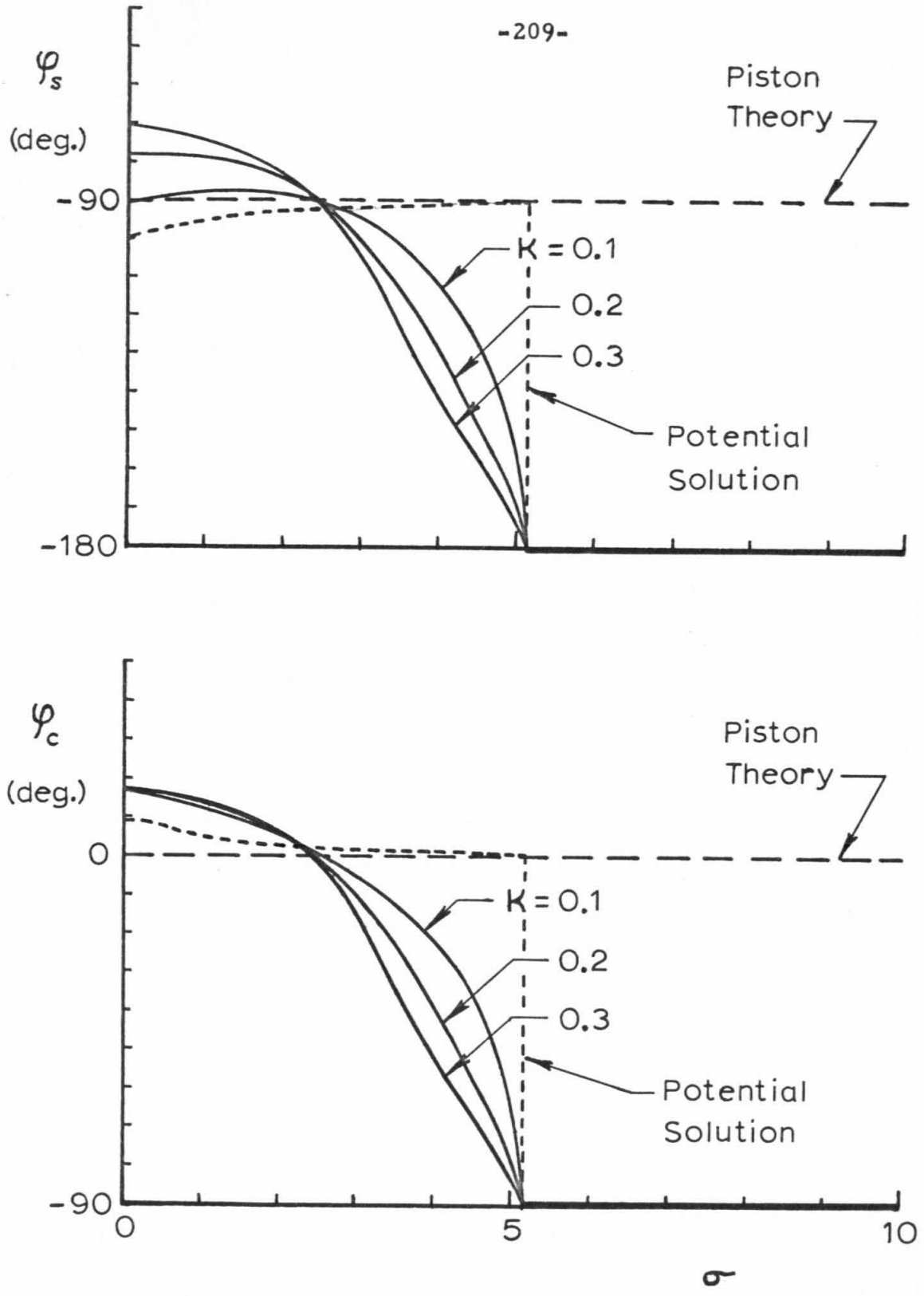

FIG. G.5 WALL PRESSURE PHASE ANGLES ($M_\infty = 3.0, k = 0.75$)